Advanced Coastal Mapping along the South Shore of NS to support Hydrodynamic Modelling: Final Report

Prepared by

Dr. Tim Webster & AGRG Team
Applied Geomatics Research Group
NSCC, Middleton
Tel. 902 825 5475

email: tim.webster@nscc.ca

Submitted to

CAPP
OERA
ECRC-SIMEC

August 31, 2018

OERA Offshore Energy Research Association

AGRG Applied Geomatics Research Group

nscc Applied Research

CAPP CANADIAN ASSOCIATION OF PETROLEUM PRODUCERS

bp

How to cite this work and report:

Webster, T. 2018. “Advanced Coastal Mapping along the South Shore of NS to support Hydrodynamic Modelling: Final Report” Technical report, Applied Geomatics Research Group, NSCC Middleton, NS.

Executive Summary

Mapping along the coastal zone is very challenging as there are many technologies that are well suited for the land or deep water, but not the shallow coastal zone. Knowledge of the nearshore currents and materials both submerged and exposed along the shoreline are critical to contaminant spill preparedness and are typically not mapped at a sufficient level of detail to facilitate an effective and efficient response if such a spill were to occur. This project utilized a topo-bathymetric lidar sensor to provide a seamless high-resolution elevation model across the coastal zone with simultaneous aerial photography of a large tidal inlet near Lockport in southwest Nova Scotia. These data were the basis for the development of a hydrodynamic model to calculate the tidal currents and interactions of the ecologically sensitive tidal inlet and the open ocean. Drifter buoys were deployed at different locations near the tidal inlet equipped with GPS to track their trajectories and interaction with the tidal inlet. Two Acoustic Doppler Current Profiles (ADCP) were deployed in shallow and deep water for one month to record water levels and current speeds to compare to the hydrodynamic model. Particles representing spill contaminants were released at different locations seaward of the inlet and tracked to determine their fate. These simulations were conducted under normal tidal conditions and under conditions of variable winds based on previous offshore environmental impact assessments. The lidar and orthophotography were used to construct cover maps of both the shoreline substrate and the benthic environment. This project has demonstrated the rich information base that can be derived from a single topo-bathymetric lidar flight by providing both detailed nearshore elevation and information on the aquatic vegetation, as well the terrestrial vegetation although that was not the focus of this study. Our results indicate that contaminants do not enter the inlet unless they are released very close to the mouth of the inlet despite the large currents observed in the inlet channel. We interpret this behavior to be a result of a large shoal that is located seaward of the mouth of the inlet that locally affects current velocities and appears to impede movement of material into the inlet. It is our recommendation that this approach be applied to other tidal inlets and potentially sensitive shorelines to support the Ocean Protection Plan so that we are knowledgeable about our coast and water movement in the event of a contaminant spill or other environmental threats.

Acknowledgements

We would like to thank the Offshore Energy Research Association of Nova Scotia (OERA), the Canadian Petroleum producers (CAPP) for providing funding and ECRC for providing in-kind support for this project.

Table of Contents

Table of Figures

List of Tables

1 Introduction

1.1 Project Background

Lockeport, NS, like many communities situated along the Atlantic shore, may be vulnerable to contamination in the event of an offshore oil spill. This is due to the highly dynamic and biologically rich tidal inlets, which pose a challenge for responders, compared to accessible linear sections of the coast. Additionally, variable currents, changing water levels, shoals, and exposed seaside conditions together make effective response difficult. Protecting tidal inlets is important, as the associated sheltered back bays often feature highly productive salt marsh and tidal-flat environments that are very sensitive to oil spills. Information related to tidal inlet morphology is limited or out-of-date, and no information regarding water current speeds and bathymetry is available to aid response organizations in planning to respond to a spill. This lack of information also presents risks to the health and safety of first responders with respect to secure access and safe navigation in light of shifting channels and shoals, unpredictable currents, etc.

In order to generate detailed maps of the shallow nearshore zone where the use of traditional bathymetric methods is limited, Nova Scotia Community College (NSCC)'s Applied Geomatics Research Group (AGRG) conducted a survey of Lockeport in August 2017 using an innovative airborne lidar system to collect surface and shallow submarine topographic data. This project was funded by the Canadian Association of Petroleum Producers (CAPP) with contributions from Shell Canada and BP with matching funding from the Offshore Energy Research Association (OERA) with in-kind support from Eastern Canada Response Corporation (ECRC), a marine oil spill response organization. The study was Year 2 of a two-year study. The purpose of this project was to investigate how high-resolution imagery, topo-bathymetric lidar, and hydrodynamic modelling can be used to improve planning for and response to contaminants in the near coastal environment. In Year 1, a similar study was conducted at Cow Bay, NS.

Ground truth surveying was conducted, which involved the deployment of two Acoustic Doppler Current Profilers (ADCP) in Lockeport for one month. AGRG researchers worked with ECRC staff to deploy and retrieve the ADCPs. One was deployed in shallow water, where wave and current data were collected, the second was deployed in deeper water and collected current data. Water clarity samples, seabed cover photos, and GPS seabed measurements were collected. Additional in-situ sampling involved using a RiverRay ADCP to measure the flow in and out of the Matthews Lake tidal inlet. Boat based sampling included a Biosonics echo-sounder survey to map submerged aquatic vegetation (SAV). A variety of experiments were conducted after the aerial surveys using drifter buoys to observe the flow in and out of the Matthews Lake tidal inlet.

This document is the final report to update OERA, CAPP and ECRC on the progress and initial results generated by this second phase of the project.

1.2 Study Area

The study area of Lockeport was selected for the second phase of this project for two main reasons: 1) it is a typical bay with a tidal inlet that connects the ocean to a sensitive salt marsh, and 2) its location on the south shore where oil and gas exploration is occurring offshore (Figure 1.1).

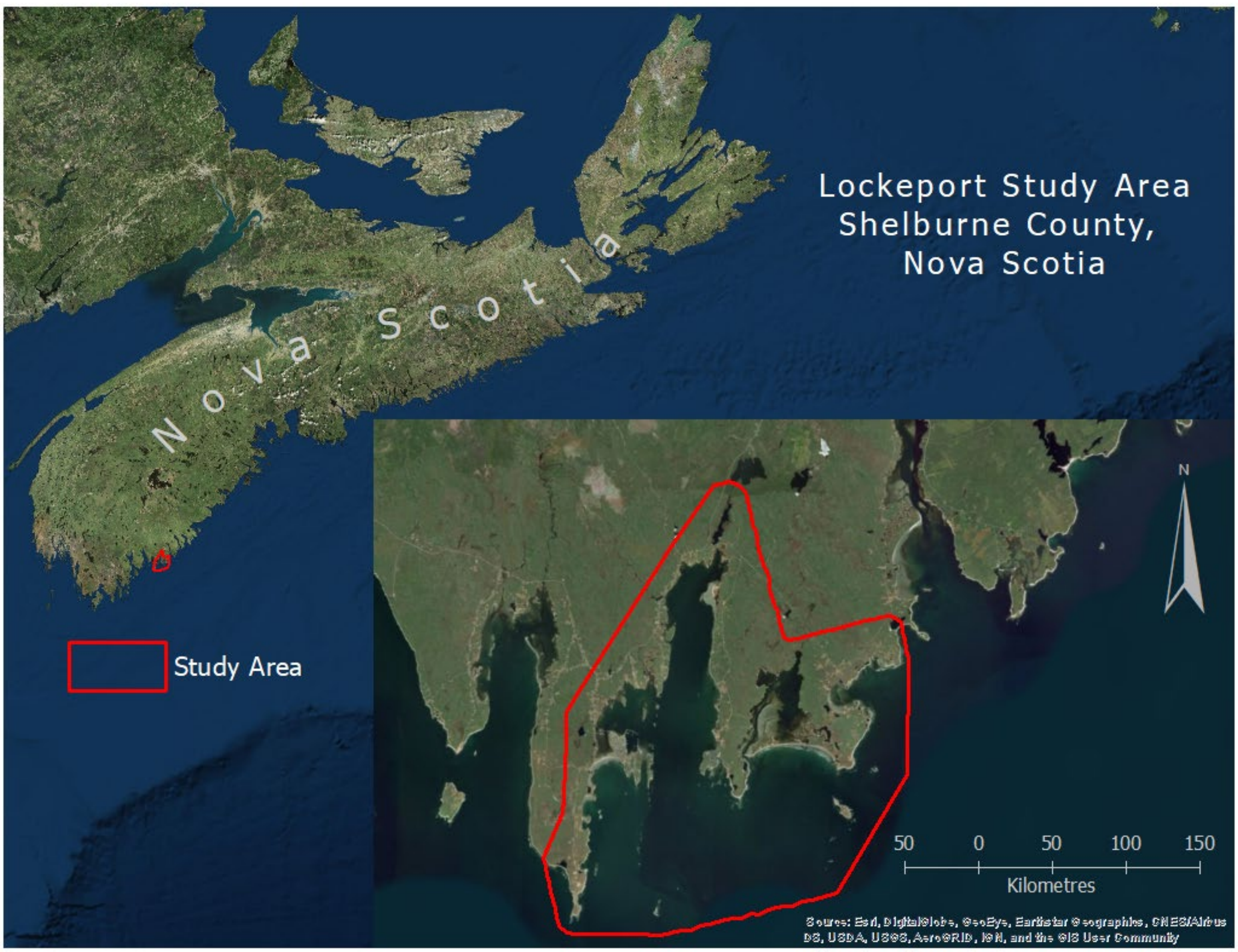

Figure 1.1: The topographic-bathymetric lidar study area near Lockeport, NS. (Imagery source: ESRI DigitalGlobe World Imagery)

2 Methods

2.1 Sensor Specifications

The lidar sensor used in this study is a Chiroptera II integrated topographic-bathymetric lidar sensor equipped with a 60-megapixel multispectral camera. The system incorporates a 1064 nm near-infrared laser for ground returns and sea surface and a green 515 nm laser for bathymetric returns (Figure 2.1, Figure 2.2d). The lasers scan in an elliptical pattern, which enables coverage from many different angles on vertical faces, causes less shadow effects in the data, and is less sensitive to wave interaction. The bathymetric laser is limited by depth and clarity, and has a depth penetration rating of roughly 1.5 x the Secchi depth (a measure of turbidity or water clarity using a black and white disk). The Leica RCD30 60 megapixel camera (Figure 2.2d) collects co-aligned RGB+NIR motion compensated photographs which can be mosaicked into a single image in post-processing, or analyzed frame by frame for maximum information extraction.

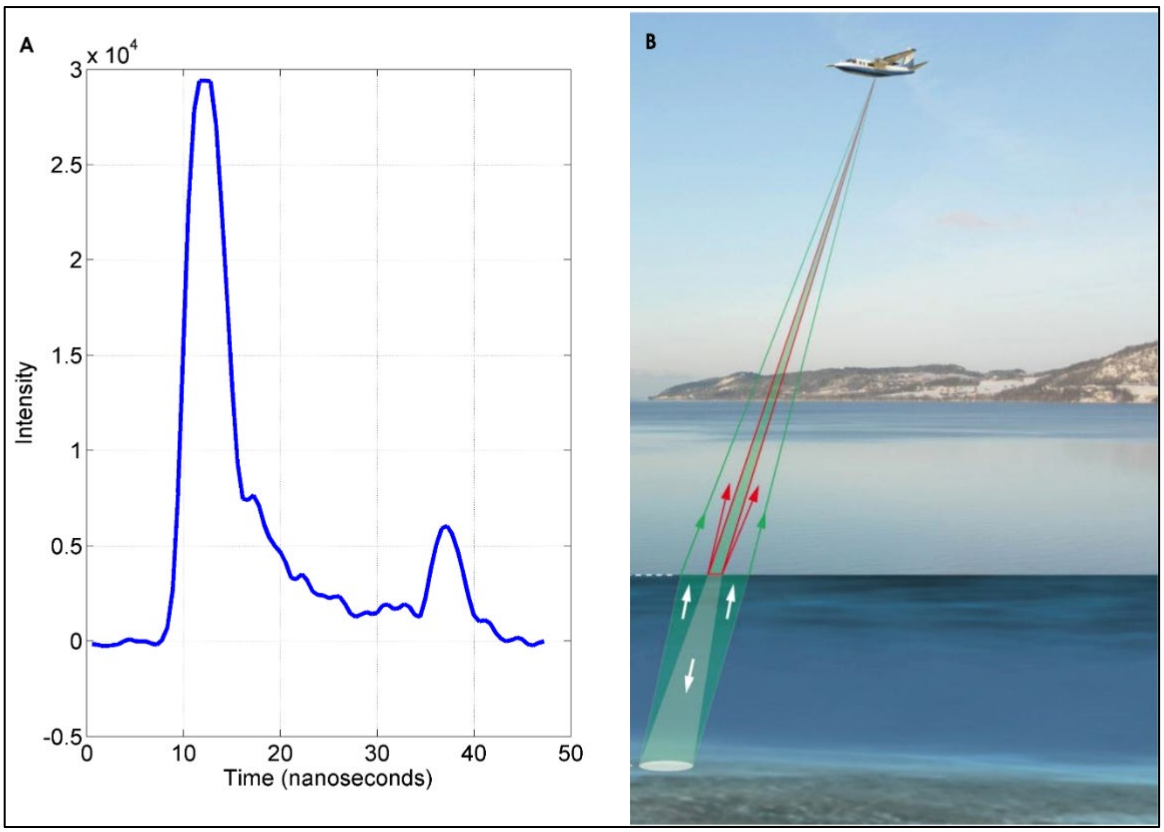

Figure 2.1: (A) Example of the Chiroptera II green laser waveform showing the large return from the sea surface and smaller return from the seabed. (B) Schematic of the Chiroptera II green and NIR lasers interaction with the sea surface and seabed (adapted from Leica Geosystems).

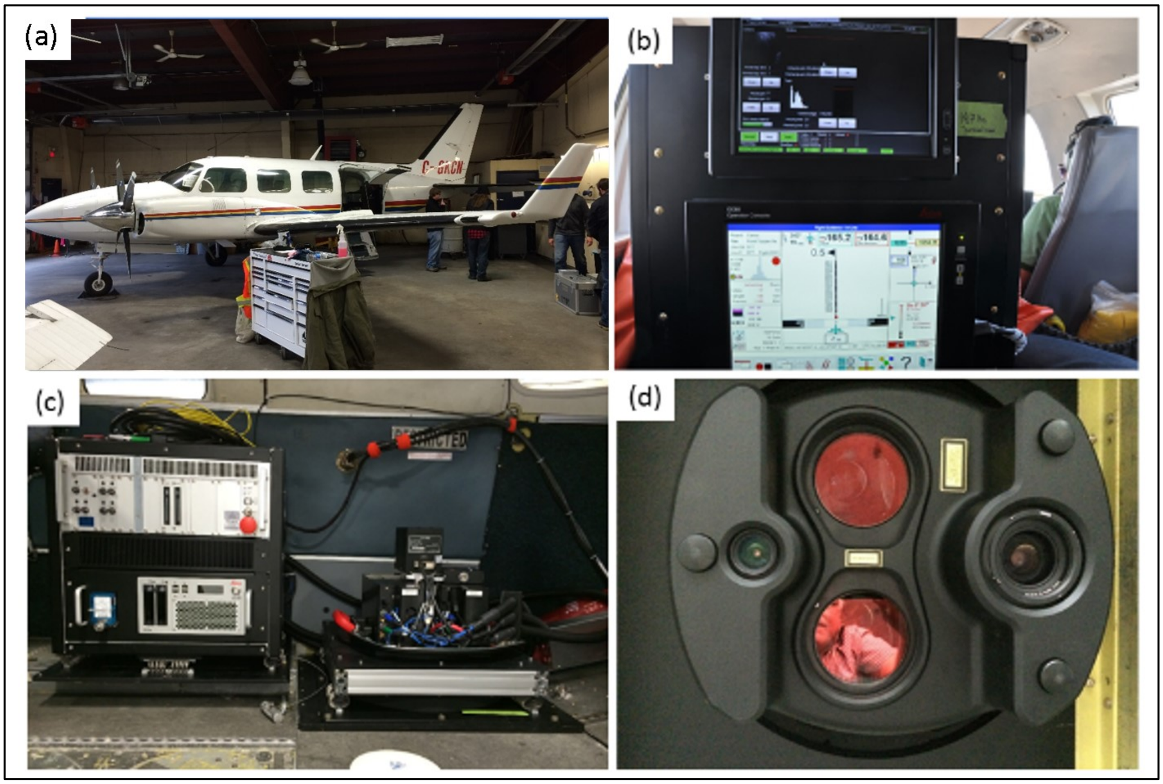

Figure 2.2: (a) Aircraft used for 2017 lidar survey; (b) display seen by lidar operator in-flight; (c) main body of sensor (right) and the data rack (left); (d) large red circles are the lasers; the RCD30 lens (right) and low resolution camera quality control (left).

2.2 Lidar Survey Details

AGRG partnered with Leading Edge Geomatics to assist in the survey operations and arranging the aircraft (AGRG-NSCC does not own an aircraft, only the sensor). The lidar sensor was installed in the twin engine aircraft in Fredericton, NB. Since the study area is significantly large, two lidar surveys were conducted using the Chiroptera II sensor on August 28 and 29 2017. The survey was planned using Mission Pro software and was flown at an altitude of 400 m above ground and took a total of 7 hours to complete. The aircraft required ground-based high precision GPS data to be collected during the lidar survey in order to provide accurate positional data for the aircraft trajectory. The Nova Scotia Active Control Stations (NSACS) cellular network was used to provide geodetic control and a GNSS base station during the survey was used to process the trajectory of the survey aircraft (Figure 2.3). The NSACS network was also used to establish base station coordinates for real-time kinematic collection of ground truth data within the study area.

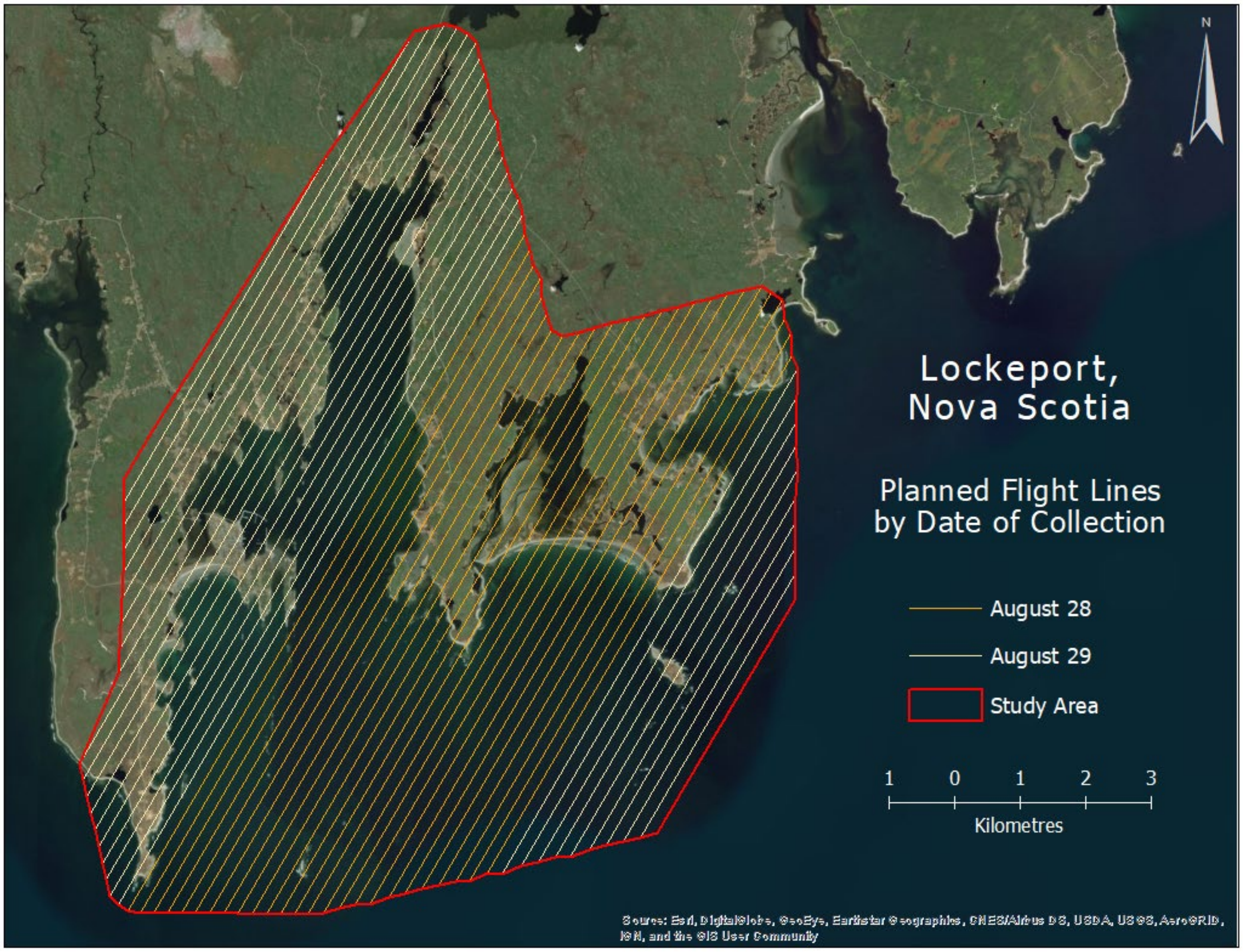

Figure 2.3: Aircraft planned flight lines for the 2017 lidar survey in Lockeport.

2.3 Time of Flight Conditions

Meteorological conditions during and prior to topo-bathy lidar data collection are an important factor in successful data collection. As the lidar sensor is limited by water clarity, windy conditions have the potential to stir up any fine sediment in the water and prevent laser penetration. Rain or fog are not suitable for lidar collection, and the reflection from the water (sun glint) must also be factored in for the collection of aerial photography. Before each lidar survey, we primarily monitored weather forecasts using four web applications: the Environment and Climate Change Canada (ECCC) public weather forecast (http://weather.gc.ca/), ECCC's Marine Forecast (http://weather.gc.ca/marine/index_e.html), SpotWx (www.spotwx.com), which allows the user to enter a precise location and choose from several forecasting models of varying model resolution and forecast length, and lastly, a customized ECCC forecast delivered to AGRG every 8 hours. Each of these tools had strengths and weaknesses and it was through monitoring all four that a successful lidar mission was achieved. For example, the customized ECCC forecast was the only tool that provided an hourly fog prediction. However, the SpotWx graphical interface proved superior for wind monitoring. Only the ECCC public forecast provided Weather Warnings that were broadcast in real-time, such as thunderstorms, and the marine forecast provided the only information for offshore conditions.

Weather observations are presented for the nearest ECCC weather station, Liverpool, ~50 km northeast of the study area (Figure 1.1). After a wind event one week before the lidar survey (Aug. 22- 24, wind SW > 20 km/hr), meteorological conditions did not pose any threat to water clarity (Figure 2.4). Winds were mainly from the NW and remained < 20 km/hr. The first portion of the Lockeport lidar survey occurred on August 28 13:00 – 16:30 UTC (10:00 ADT – 13:30 ADT) on a rising tide (Figure 2.4, Figure 2.5). Wind during the survey blew from the NE at ~10 km/hr. On August 29 the survey took place between 12:30 – 16:00 UTC (9:30 ADT – 13:00 ADT) during a rising tide (Figure 2.4, Figure 2.5). Wind was again from the NE, < 10 km/hr.

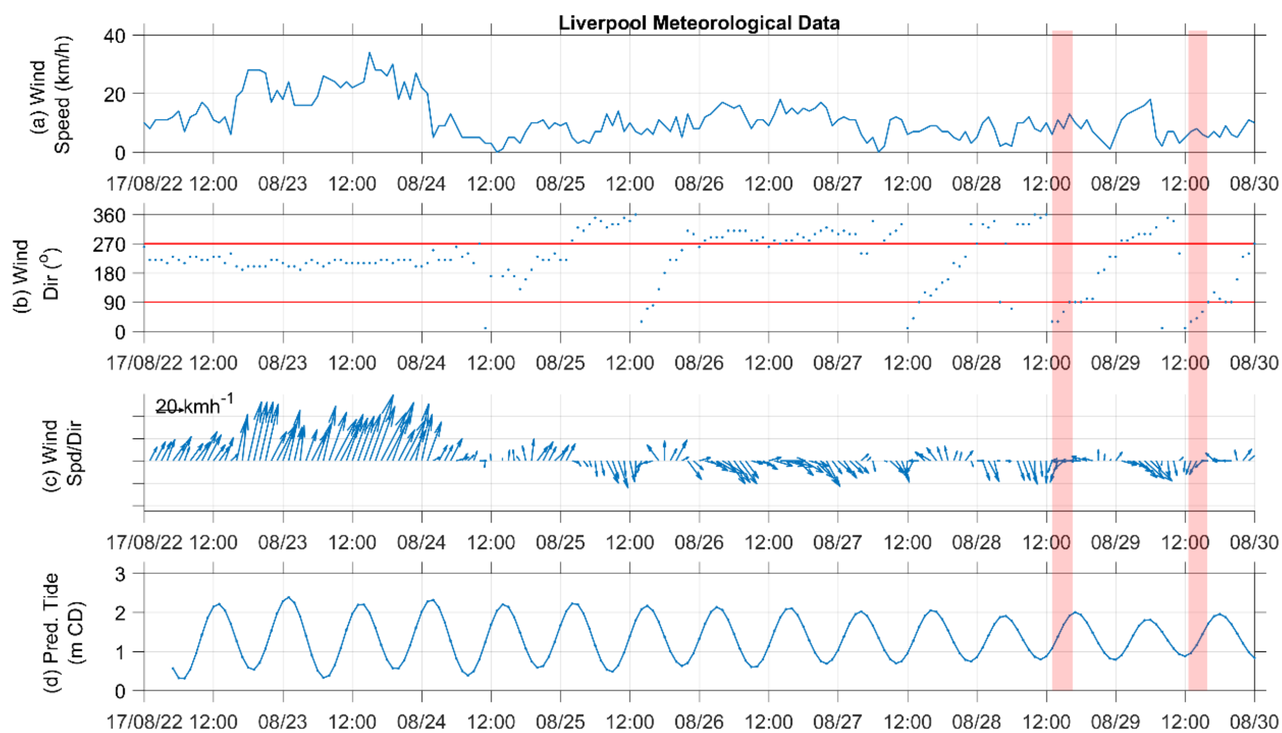

Figure 2.4: Weather preceding and during the Lockeport lidar surveys. Red boxes indicates the lidar survey duration. (a) Wind speed and (b) direction collected at the EC weather station at Liverpool between Aug 22 and Aug 30, 2017 at 1-hr intervals. Panel (c) shows a vector plot of the wind, where the arrows point in the direction the wind is blowing. Panel (d) shows predicted tide.

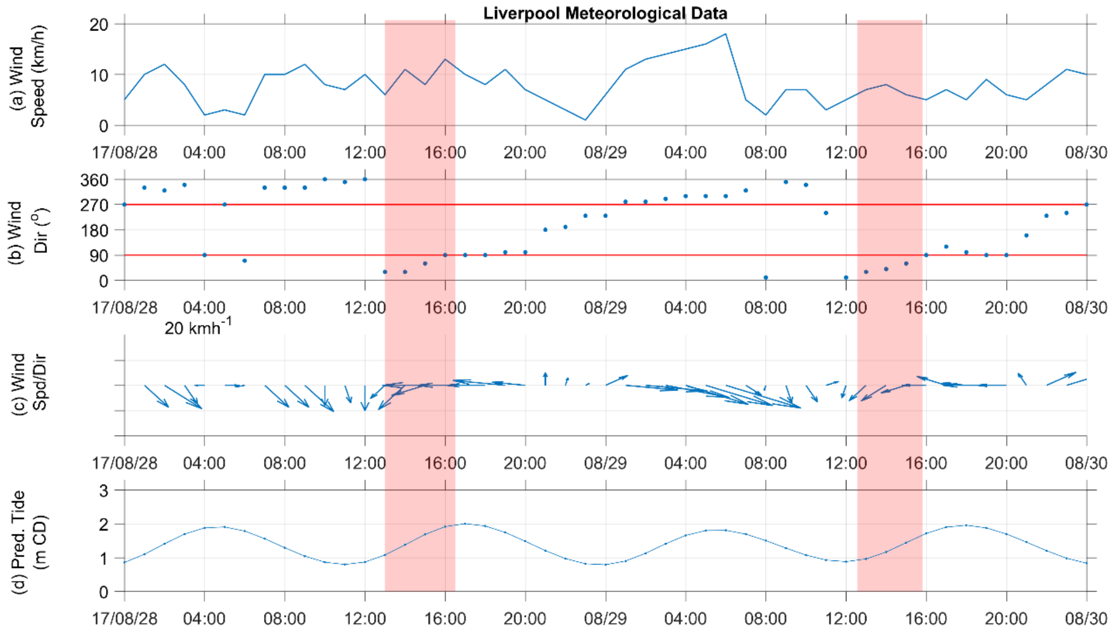

Figure 2.5: Weather during the Lockeport lidar surveys. Red boxes indicates the lidar survey duration. (a) Wind speed and (b) direction collected at the EC weather station at Liverpool between Aug 28 and Aug 30, 2017 at 1-hr intervals. Panel (c) shows a vector plot of the wind, where the arrows point in the direction the wind is blowing. Panel (d) shows predicted tide.

2.4 Ground Truth Data Collection

Ground truth data collection is a crucial aspect of topo-bathymetric lidar surveys. During the lidar survey on August 29, 2017, AGRG researchers conducted traditional ground truth data collection including hard surface validation and seabed elevation measurements to validate the lidar, Secchi depth measurements for information on water clarity, and underwater photographs to obtain information on bottom type and vegetation. Table 2.1 and Figure 2.6 summarize the ground truth measurements undertaken for Lockeport in 2017, Figure 2.7 shows a map of the distribution of ground truth measurements, and Figure 2.9 highlights fieldwork efforts. Underwater photos were captured using a 0.25 m^2 quadrat with a downward-looking GoPro camera for validating benthic classifications (Figure 2.9a, b) and shoreline imagery was captured (Figure 2.9c) for shoreline classification validation. Validation images are presented in Section 3.2.1. The seabed elevation was measured directly using a large pole onto which the RTK GPS was threaded. A series of drogue experiments was conducted for circulation model validation (Figure 2.9f, Figure 2.8). An AML Conductivity Temperature Depth (CTD) sensor was used to acquire observations of the vertical structure of the water column throughout the study area (Figure 2.7) to assist with model setup.

Currents near the tidal inlet were measured using three different ADCPs. A Teledyne RiverRay ADCP is a small towed vessel containing a downward-looking 600 kHz ADCP that measures the cross-sectional depth and flow of a channel. Multiple transects were collected with the RiverRay ADCP at different locations along the tidal inlet channel for model validation (Figure 2.10, Figure 2.9e). The RiverRay uses a GPS system mounted to the vessel for positioning. Two upward-looking Teledyne ADCPs were used for model validation (Table 2.2). The Teledyne RDI Sentinel V20 1000 kHz Acoustic Doppler Current Profiler (ADCP) was deployed twice to measure waves and currents. The first deployment was in ~7.4 m water depth for 40 days, while the second deployment was in the channel mouth in ~2.4 m water depth for only 3 days. The Teledyne RDI Sentinel V100 300 kHz ADCP was deployed in ~13.5 m deep water for 37 days and measured currents only. ADCP data are presented in Section 3.3.2.

Date	Secchi (Y or -)	Depth (see caption for options)	ADCP + Hobo underwater light and pressure sensors	Underwater Photos (see caption for options)	Hard Surface GPS (Y or -)	RiverRay (Y or -)	CTD	Drogues	Biosonics	Shoreline substrate mapping
July 27	Y	P, ES	V20 (shallow) and V100 (deep) deployed	Pole + GoPro			Y		Y	
Aug 29* (?)	Y	M,P,		Pole + GoPro, Quadrat			Y		Y	Y
Sept 6		P,ES	V20 (shallow) and V100 (deep) recovered							
Sept 12			V20 deployed in channel							
Sept 13										
Sept 14			V20 recovered from channel	3D camera		Y		Y		

Table 2.1: Lockeport ground truth data summary. * indicates fieldwork coincided with lidar survey. GPS Column: The GPS systems used were the Leica GS14 or handheld Garmin unit. Depth Column: P=GPS antenna threaded onto the large pole for direct bottom elevation measurement, M=manual depth measurement using lead ball or weighted Secchi disk, ES=single beam echo sounder. Underwater Photos: Underwater Photos: Pole for underwater still photos with GoPro; Quadrat Q50=0.25 m2 quadrat with downward-looking GoPro camera.

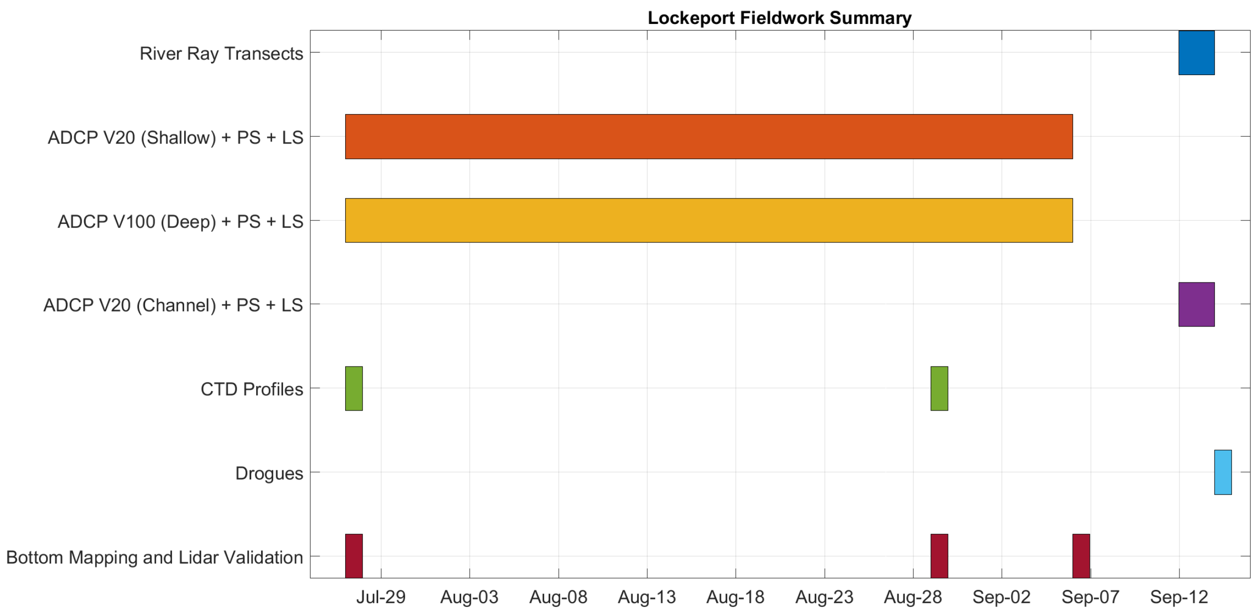

Figure 2.6: Fieldwork summary.

ADCP	Frequency	Deployed	Recovered	Currents	Waves	Depth	Location
V20 "Shallow"	1000 kHz	July 27	Sept. 5	✓	✓	7.4 m	43.688982, -65.116453
V20 "Channel"	1000 kHz	Sept. 12	Sept. 15	✓	✓	2.4 m	43.695717, -65.063276
V100 "Deep"	300 kHz	July 27	Sept. 2	✓		13.5 m	43.678315, -65.053408

Table 2.2: ADCP deployment and recovery summary.

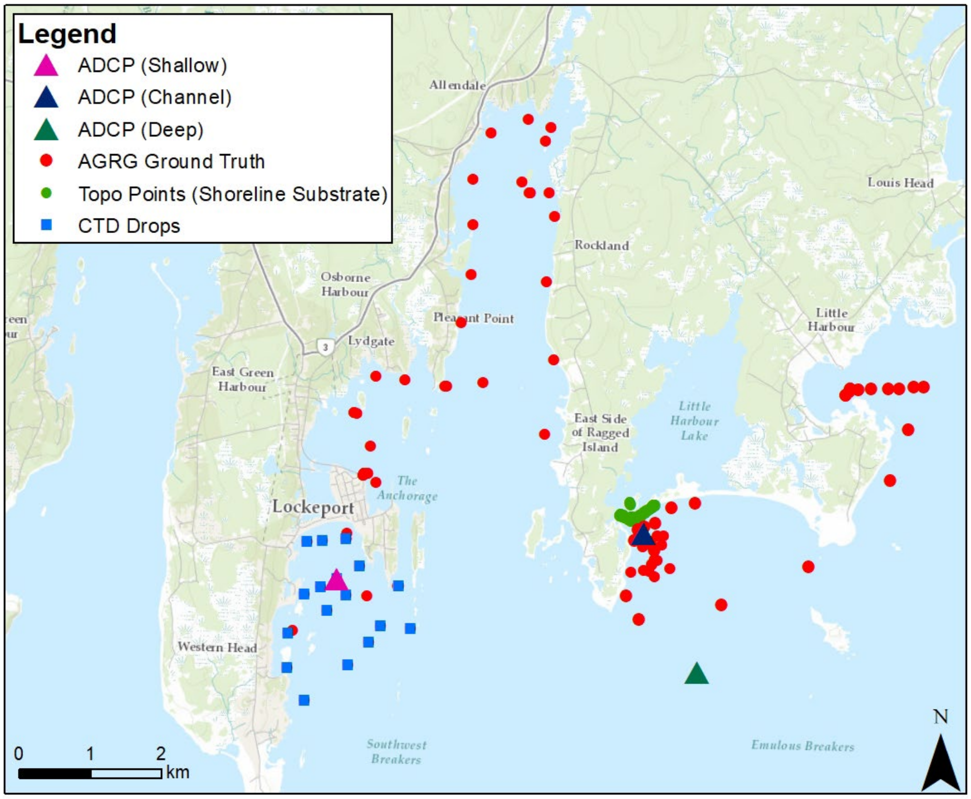

Figure 2.7: Location of topo GPS points collected on the shoreline (green), boat-based ground truth points (red), CTD drop locations (blue), and 3 ADCP deployment locations at Lockeport.

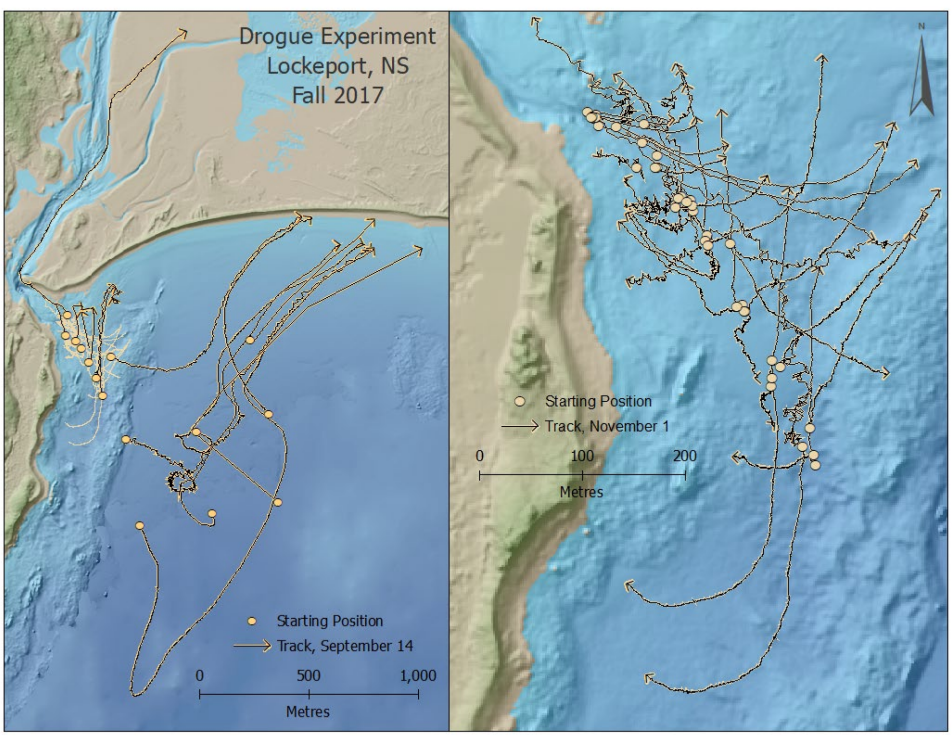

Figure 2.8: Drogues were released at Lockeport on Sept. 14 and Nov. 1. Map on the right is a close up of the mouth of the tidal inlet.

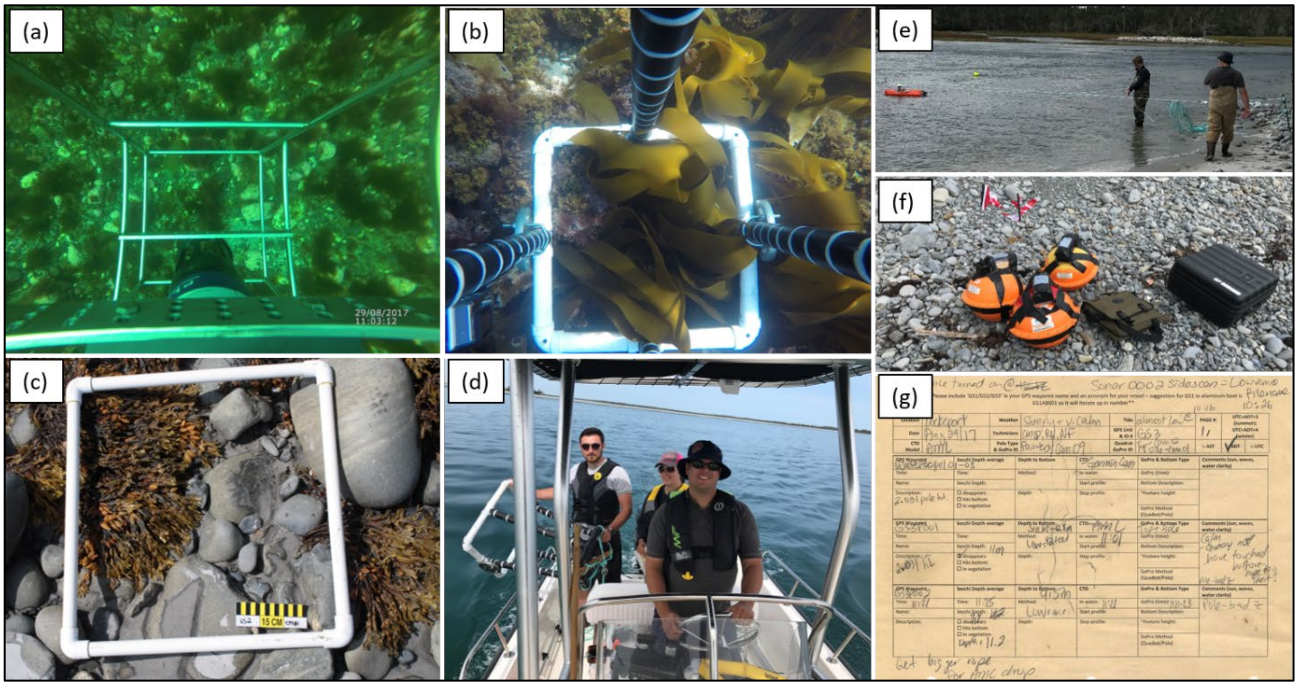

Figure 2.9: Ground truth collection at Lockeport in 2017. (a) Imagery results from CTD drop, (b) Ground truth imagery results from quadrat, (c) Shoreline substrate survey with quadrat and scale, (d) AGRG researchers conducting boat based fieldwork, (e) AGRG researchers conducting River Ray transect, (f) Drogue buoy equipment, (g) Example of AGRG fieldwork log sheet used for ground truth surveys.

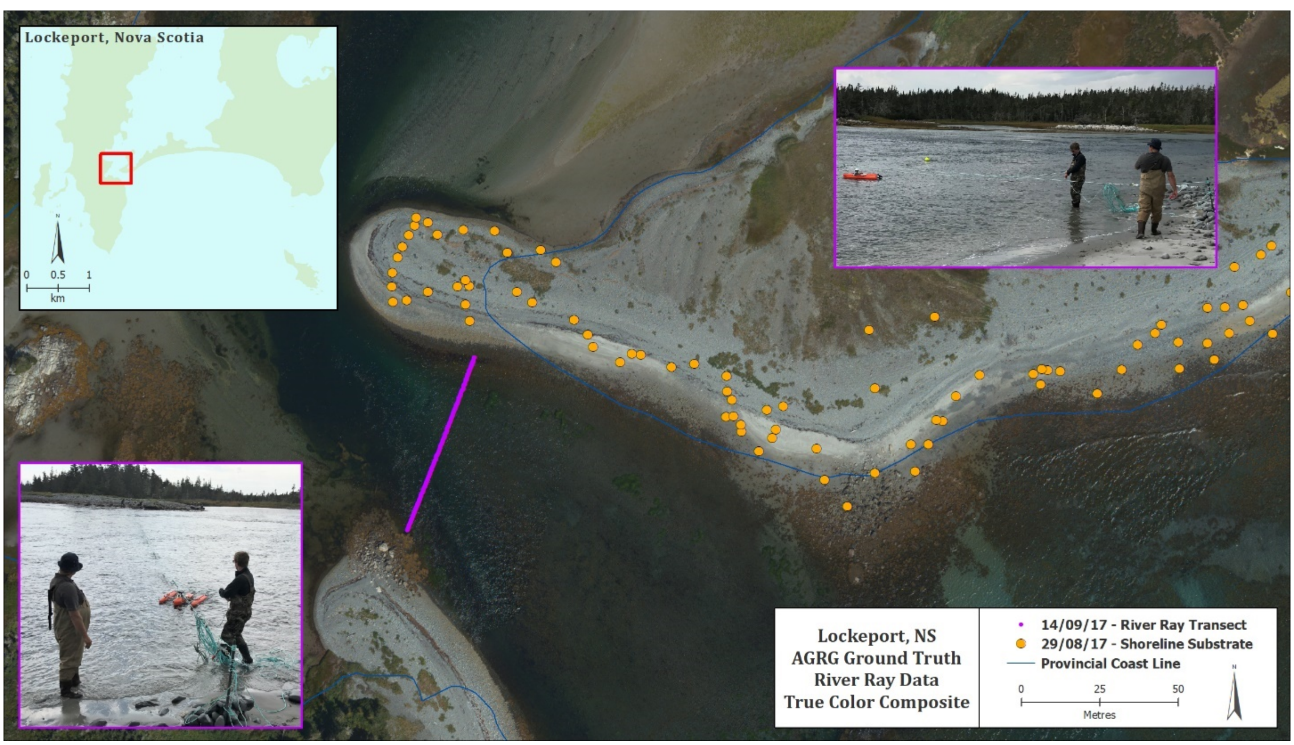

Figure 2.10: RiverRay transect locations collected on September 14.

2.5 Elevation Data and Image Processing

Lidar elevation data and image processing remained the same as in Year 1 of this project. These methods are presented here as **Error! Reference source not found.**, including information on Point Cloud Processing, Lidar Point Classification Codes and Descriptions, Gridded Surface Models, Depth Normalization of the Green Laser Amplitude, Aerial Photo Processing, and Ellipsoidal to Orthometric Height Conversion.

2.6 Classification

2.6.1 Shoreline

To isolate the shoreline area as the processing extent for classification, the lidar-derived digital elevation model (DEM) was used to mask elevations between the approximate Lower Low Water Low Tide (LLWLT) and Higher High Water Large Tide (HHWLT) + 3m. The resulting polygon was then buffered by 5m to guarantee inclusion of all shoreline in the upper marsh area of Matthew's Lake. All classification inputs were clipped to this extent. The study area was also reduced to focus on the main area of interest for this project; Matthew's Lake tidal inlet (Figure 2.11).

Shoreline substrates, such as cobble and sand, are defined by their grain sizes rather than their chemical compositions. This is due to the fact that they are typically derived from the same parent materials. As such, their spectral characteristics are quite similar and cannot be used as the sole basis for a robust classification. In order to achieve the latter, it is necessary to take image texture into account. In this analysis, image texture was quantified by means of a line density filter. In natural imagery, lines appear at the boundaries of objects (ex. boulders) and as such are analogous to edges. Theoretically, larger and brighter materials such as cobble, will produce stronger edges than finer ones such as sand, allowing them to be differentiated. An edge density raster was produced in the following way; firstly, a series of line detectors was convolved over the image, detecting all lines oriented at 0, 45, 90, and 125 degree angles in the RCD30 imagery. This produced 4 different rasters, each representing the intensity of the edges in the image that shared that specific orientation. These four rasters were averaged on a cell-by-cell basis and smoothed using a 9x9 mean filter to produce the final edge density raster. Iterating the line detector over different angles was necessary in order to ensure that the edge density metric was rotation-invariant, and as such sufficiently robust for use in the subsequent classification.

To help differentiate boulders with high edge density values from other naturally existing edges such as the transition between vegetation and sediment, a normalized height model (NHM) was included in the classification. To construct the NHM, a resampled (to 10cm) lidar-derived DEM was subtracted from a high resolution (10cm)

Figure 2.11: Matthew's Lake tidal inlet area of interest for shoreline and benthic classification.

photogrammetrically-derived digital surface model (DSM). The NHM highlights changes in elevation due to objects on the ground surface such as boulders, but does not reflect changes in ground elevation. Therefore, boulders have significantly different values than substrate transitions and low-relief vegetation edges.

A Normalized Difference Vegetation Index (NDVI) layer derived from the RCD30 imagery was also included in the classification, and was calculated from the near infrared (NIR) and red bands. The rationale for this was as follows. Firstly, rocky materials have low NDVIs whereas vegetation tends to have very high NDVI values. As such, NDVI provides a concise descriptor of the amount of rocky material that is exposed in regions with vegetation cover (ex.

swash zone). Rocky materials with vegetation on them tend to appear darker, and as such have weaker edges than they would without it. As such, based on the texture alone cobble with vegetation on it could statistically be closer to dry pebbles than it would be to dry cobble. Adding the NDVI takes this phenomenon into account, increasing the reliability of the classified results.

The NDVI, edge density and NHM rasters were then combined with multispectral RCD30 imagery bands to construct an image composite for use in a supervised Maximum Likelihood classification (Figure 2.12). Due to the fairly consistent weather and cloud cover during both surveys, there was no need to classify on a per flightline basis, so the Matthew's Lake area of interest was classified as a single image composite. One of the limitations of this classification approach was that it was difficult to reliably differentiate bedrock from other sediment classes. For example, very smooth bedrock was commonly confused for sand whereas rough bedrock was often mistaken for boulders. As such, the bedrock class was removed from the classification and outcrops of that nature were digitized manually post classification.

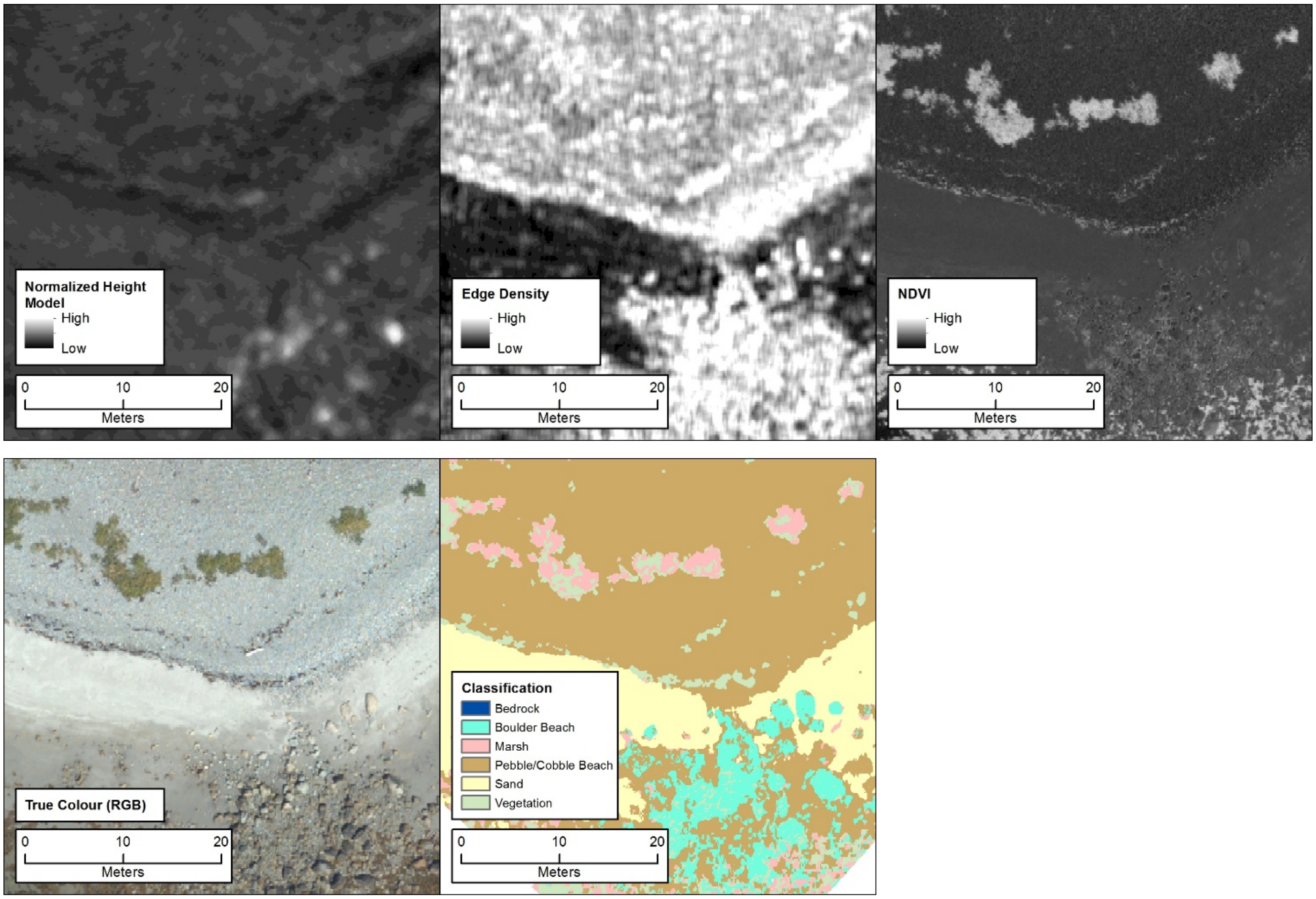

Figure 2.12: Example of input bands for shoreline classification with resulting classified raster. Top left is the normalized height to highlight boulders. Top middle is an edge density map to highlight the texture difference between sand and cobble. Top right is normalized difference vegetation index to highlight living vegetation. Bottom left is a true colour composite. Bottom right is an example of the final shoreline classification.

2.6.2 Benthic

Submerged Aquatic Vegetation mapping (SAV) was conducted using two contrasting methods and their results compared: (1) Unsupervised iso-cluster maximum likelihood and (2) Supervised Classification with Support Vector Machine. Both methods required first determining and preparing key vegetation presence-absence indicator raster layers as indicated by visually assessing the presence and absence of vegetation in the aerial photographs and consulting ground truth information.

The unsupervised approach was constructed iteratively in an iso-cluster using ArcMap. It is noted that careful preparations of the input layers were critical to avoid overrepresentation of signals such as solar glint and water conditions which would confuse the automated clustering algorithm. Classifications produced 50 auto generated clusters per attempt and performed on 0.50 m spatial resolution with a sample interval of 2.00 meters. The resulting clusters were then manually interpreted into descriptive bottom type classifications using RCD30 high resolution orthographic photography for visual reference with assistance from underwater photography. The iso-clustering approach has been proven successful for regional scale mapping of vegetation presence absence in the coastal zone for species such as eelgrasses (Hogrefe et al. 2014).

The supervised approach was conducted using the classification wizard in ArcPro. Sparse training polygons were generated manually using the available wizard whereby vegetated and non-vegetated features were highlighted as indicated by direct interpretation of the RCD30 high-resolution orthographic photography. The Support Vector Machine (SVM) classification routine was selected such that the effect of water clarity variability could be intrinsically reduced though providing training examples across a range of water conditions and depths. As such, the support vector machine approach has been considered a highly effective classification method when used in the coastal zone (Collin et al. 2011).

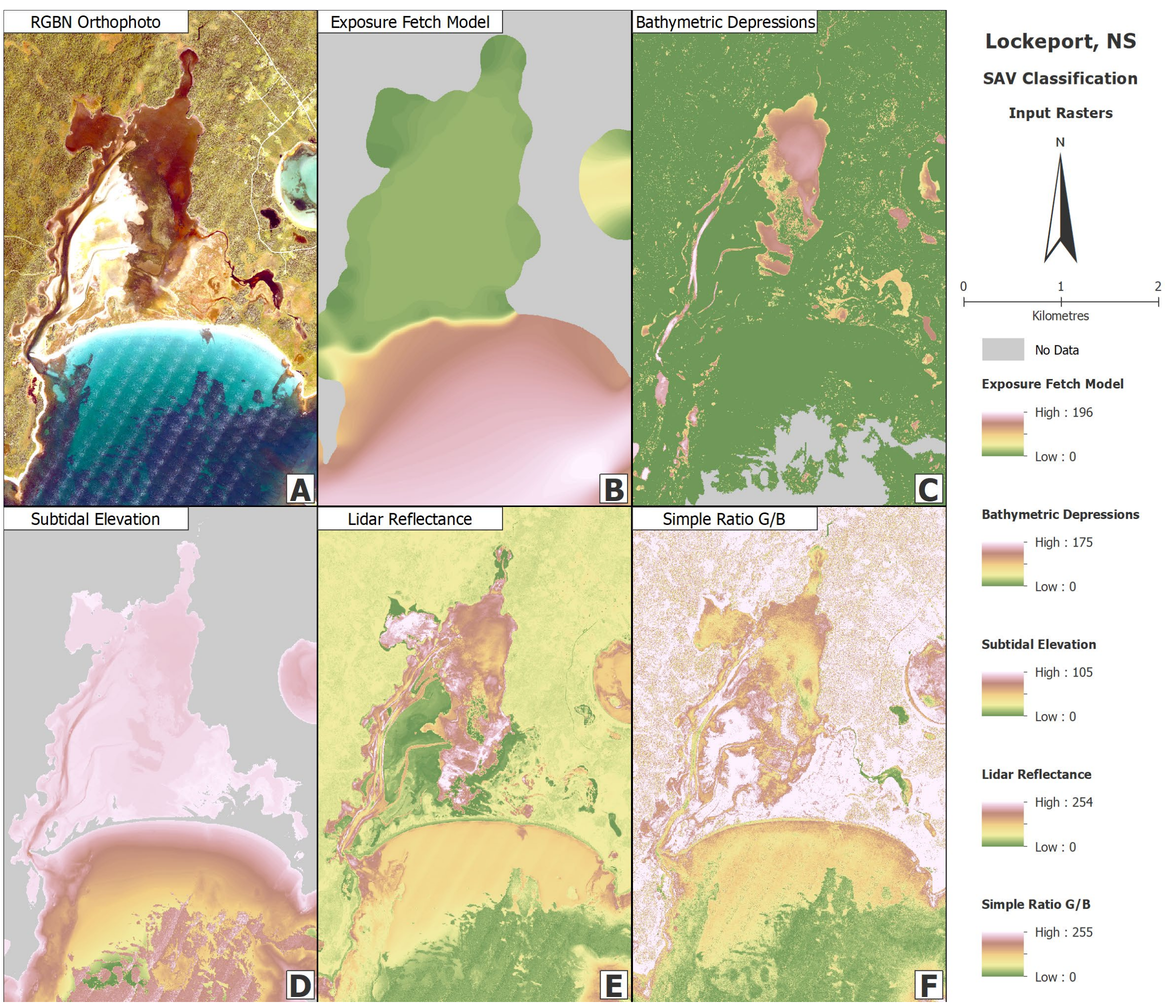

Figure 2.13: Each main input layer into the ISO and SVM clipped to the target Mathews Lake area.

The following layers were used in the final clustering and classification procedures:

- RCD30 high resolution orthographic photography
  - The RCD30 camera onboard the Chiroptera II provided 5 cm resolution true color (RGB) and near infrared composite images. For the clear water and relatively glint free conditions of the flight, this dataset provided good shallow water radiometry without much manipulation. The RGB channels are useful in differentiating vegetation by subtle color and to ensure good separation of shallow sand and vegetation. The near-infrared channel is essential in differentiating exposed terrestrial vegetation from sands and muds. To increase the radiometric signal strength, this layer was down sampled to a 0.50 m average value per band.
- Approximate Wind Fetch
  - A custom tool was constructed to approximate the magnitude of wind fetch, or the amount adjacent open water, at a high resolution. This dataset was deemed essential to ensure a clean separation of clustering between various coastal/submerged features which exhibit very similar radiometric and geometric properties such as sheltered shallow march muds and shallow exposed brown rock weeds. This analysis was performed on 20.00 m grid cells, and up-sampled to 0.50 m using a diffuse interpolation technique. The tool itself was built on top of the view shed estimating algorithm in ArcMap to approximate the magnitude of total visible ocean at any given point in the bay based on a simple coast line.
- High-High Water Large Tide Elevation
  - The seamless bathymetric elevation data was adjusted to the approximate high-high water large tidal elevation level for the Lockport area using vertical separation from NAD83 ellipsoid made available by the Canadian Hydrographic Service (CHS) continuous vertical tide datum initiative. This dataset provided a clean clipping geometry for subtidal features such that terrestrial features (buildings, roads, and trees) were not included in the clustering. This layer is also essential in helping differentiate clusters of deep vegetation classes such as kelp where radiometric backscatter signals become weaker and less distinguishable. This dataset was up-sampled from a native 1.00 m to 0.50 m using linear interpolation.
- Localized Bathymetric Depressions

    - The presence of pits, scours, and other depressions in bathymetry are key ecosystem indicators which can be used for biological segmentation. These features are detected at a high resolution in the lidar derived bathymetry by performing a hydrological fill-sink and differencing approach. This layer helps therefore further distinguish deep and dark areas which may otherwise appear radiometrically similar. This layer was generated on the native 1.00 m lidar resolution and up-sampled to the common 0.50 m spatial resolution for clustering analysis.

- Lidar Reflectance
    - Significant effort was put forth to ensure a lidar reflectance raster was generated with a minimum amount of artifacts such that it could be used at the highest reasonable spatial resolution successfully based on the sampling resolution of the lidar during the survey. Such techniques include separating the gridding process into forward-scan, back-scan and interleaved flight lines before integrating into a mosaic. Proper bottom reflectance calibration was not performed due to a wide variety of water clarity conditions exhibited throughout the bay. The lidar reflectance was similarly up-sampled from the native 1.00 m resolution grid to 0.50 m for use in the clustering analysis.

- Green-Blue Simple Ratio
    - The ratio of reflected light of the approximate green and blue (G/B) spectrums in aerial photography of submerged features has a well-known implicit depth normalization effect (Stumpf, 2003). This ratio enhances contrast by brightening high albedo features such as sands while features such as vegetation remain dark. G/B was calculated from the RCD30 green and blue bands and up-sampled to 0.50 m resolution for use in the classifications.

For the iso-cluster approach, several experimental radiometric normalization techniques were included to help distinguish vegetation classifications further while reducing the effect of sun glint and water column attenuation. These layers where critical for the unsupervised classification approach which must exhibit strong natural clustering of the desired classifications. It was experimentally determined that the lidar reflectance and the green band of the RCD30 performed best for this addition. Both of these layers was normalized across depth interactively using the water depth detected by the lidar during time of flight to best accommodate for loss of signal due to water column attenuation. Additional to these layers, the following index derived from RCD30 imagery was depth normalized and included:

Equation 2.1 $$\boldsymbol{Index} = \frac{\frac{NIR-RED}{NIR+RED}}{\frac{NIR-GREEN}{NIR+GREEN}}$$

Several additional layers were attempted in both classification approaches as well but were not included in the final best classification. Such layers include: (1) many additional derived layers as ratios of photo radiometry, (2) local deviation of the lidar bathymetry slope, (3) local deviation of the tangent of lidar bathymetry aspect, (4) local standard curvature or the lidar bathymetry, and (5) Average Monthly Current generated from the lidar based hydrodynamic modelling.

Textural layers such as slope, aspect, and curvature have been useful in the classification of submerged aquatic vegetation in the past. However, it was found that given the principal location of this study around a riverine marsh that the complex nature of the local texture at a high resolution –specifically at steeply sloping bounds of channels - added a significant amount of confusion to both classifiers. Further, while the average monthly current layer does illustrate promise for use in submerged aquatic vegetation mapping due to it high correlation to sediment stability and vegetation tolerance better results for a simple presence/absence classification were routinely established without including it in the classification routine.

Each of the previously listed key layers (Red, Green, Blue, Near-Infrared, Fetch, Tidal Elevation, Local Depressions, Lidar Reflectance, G/B ratio) were supplied into a 6 dimensional principal component analysis (PCA). The resulting 6 normalized layers exhibited the maximum variance across all 9 input bands. The PCA was then supplied to the SVM classification along with a small sample of training polygons for SAV and non-SAV. The ISO classification included the PCA bands, along with the additional depth normalized raster including lidar reflectance, green, and the additional SAV index (Equation 2.1).

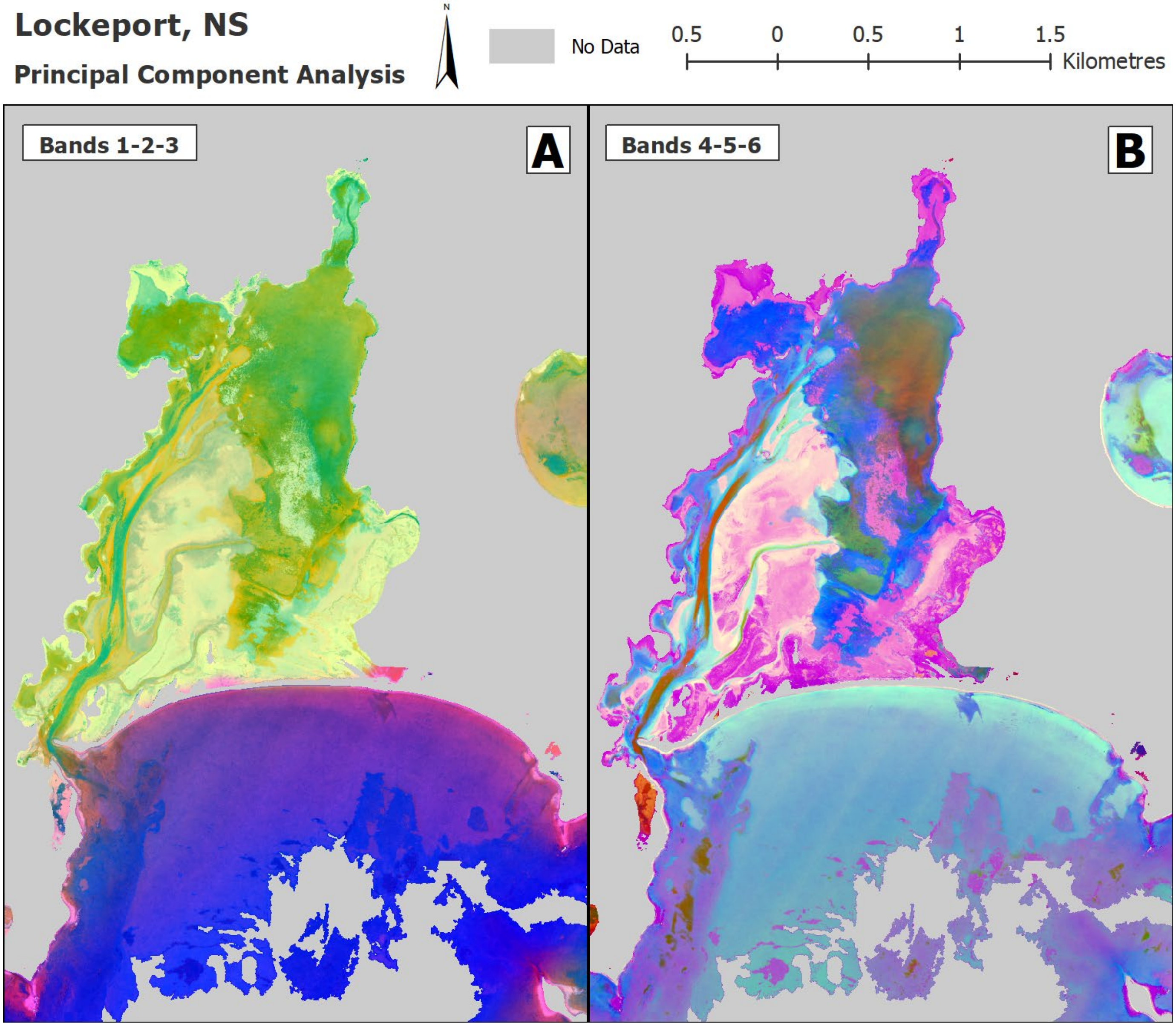

Figure 2.14: Principal Component Analysis. Left map is a composite of output components 1,2,3. Right map is a composite of output components 4,5,6.

2.7 Hydrodynamic Modelling

DHI's Mike 21 Flexible Mesh model was used to simulate ocean circulation and the fate of contaminants in the Lockeport study area. The flexible mesh model uses triangular elements in an unstructured format, which provides flexibility in terms of the representation of bathymetry compared to rectangular meshes of fixed dimensions. Element size can be chosen based on the level of detail desired by the modeler, optimizing information for a given amount of computational time (DHI Water & Environment, 2013). The model incorporated predicted tides and currents, observed winds, and baroclinic density variations. The Flexible Mesh Particle Tracking module was used to simulate the fate of contaminants such as an oil spill. This section describes model and simulation setup.

2.7.1 Model Setup

A variety of sources and resolutions of topography and bathymetry were required in order to complete the model mesh (Table 2.3). Topo-bathymetric lidar data from 2017, CHS single beam echo sounder data (Varma et al., 2008) between 20 and 60 m resolution. Single beam echo soundings collected by AGRG in 2017 using a Biosonics brand single beam echo sounder, bottom depth measurements from RiverRay, and RTK GPS bottom elevations collected during 2017 by AGRG were used for lidar validation.

Provider	Source	Native Resolution	Offsets applied/notes	Domain
AGRG	Lidar: Lockeport	1 m	Ellipsoidal to CGVD28 as noted in Appendix A	Topo/Bathy mesh
CHS	Single beam echo soundings	Variable (> 20 m)	-1.14 m (CD to CGDV28)	Bathy mesh
AGRG	Single Beam Echo Soundings (BioSonics)	Variable (< 5 m)	Survey grade GPS used to convert water depth at time of collection to CGVD28	Bathy Validation
AGRG	RiverRay ADCP	1 m	Survey grade GPS used to convert water surface time of collection to CGVD28	Bathy Validation
AGRG	RTK GPS measurements with pole	Variable	Ellipsoidal to CGVD28 as noted in Appendix A	Bathy Validation
NSTDB	Shuttle Radar Topography Mission (STRM)	20 m	Used only for islands outside the lidar domain	Bathy mesh

Table 2.3: HD model bathymetric data sources, resolution, domain and number of observations. NSDNR: Nova Scotia Department of Natural Resources.

A flexible mesh was generated such that areas of high importance (tidal inlet) were given finer resolution mesh and areas of less importance were assigned lower resolution mesh (Figure 2.15 - Figure 2.18). Resolution was defined by the maximum area of elements. The channel to the tidal inlet was assigned the finest resolution (maximum local area 100 m^2), the approach to the inlet was assigned maximum local area 1,000 m^2. The area of other elements was determined by shoreline complexity and elements were restricted to have a smallest allowable angle of 30˚. The final mesh had an overall element maximum area of 10^7 m^2, contained 61,702 nodes and 123,309 elements. Bathymetry data were interpolated to the triangular mesh using a Natural Neighbour interpolation scheme.

The model was setup using a combination of Mike 21 FM default values, study-specific values where they were available, and values that were determined in the calibration process (Table 2.4).

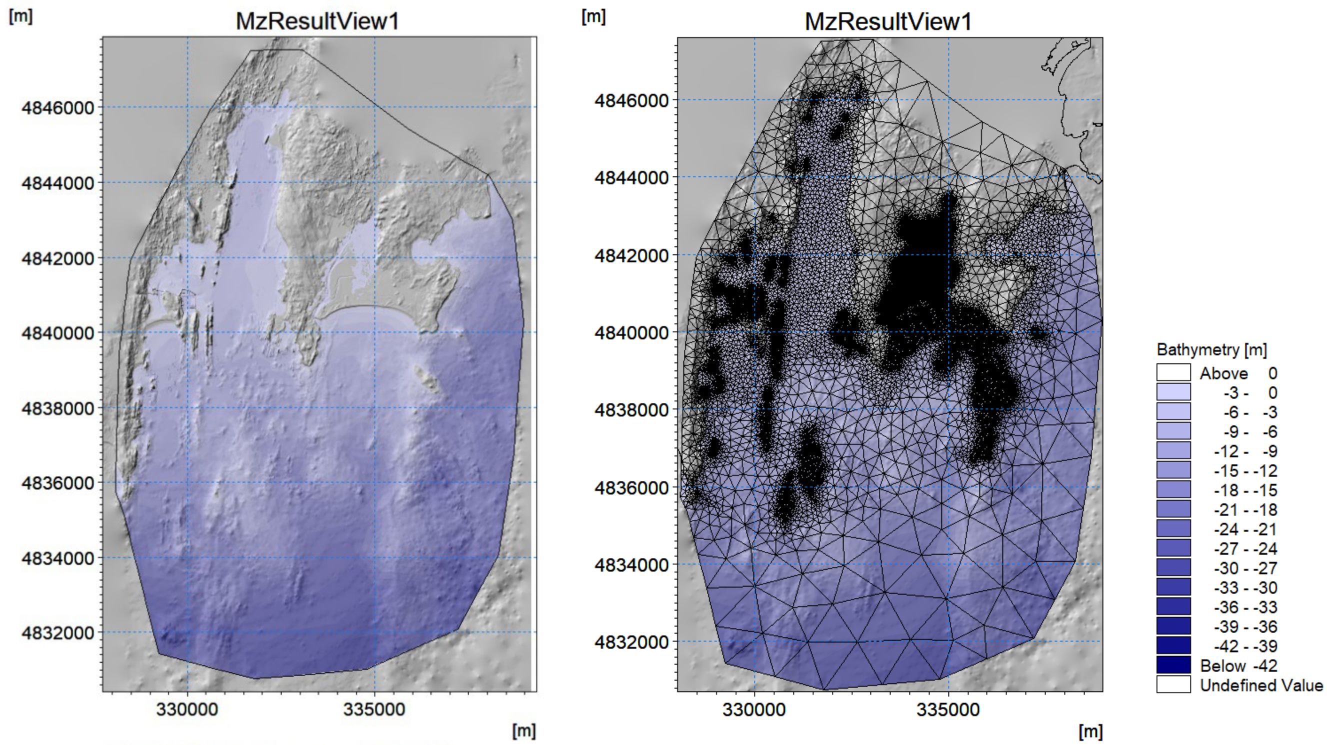

Figure 2.15: Entire model domain without element mesh and showing the variable resolution of the mesh.

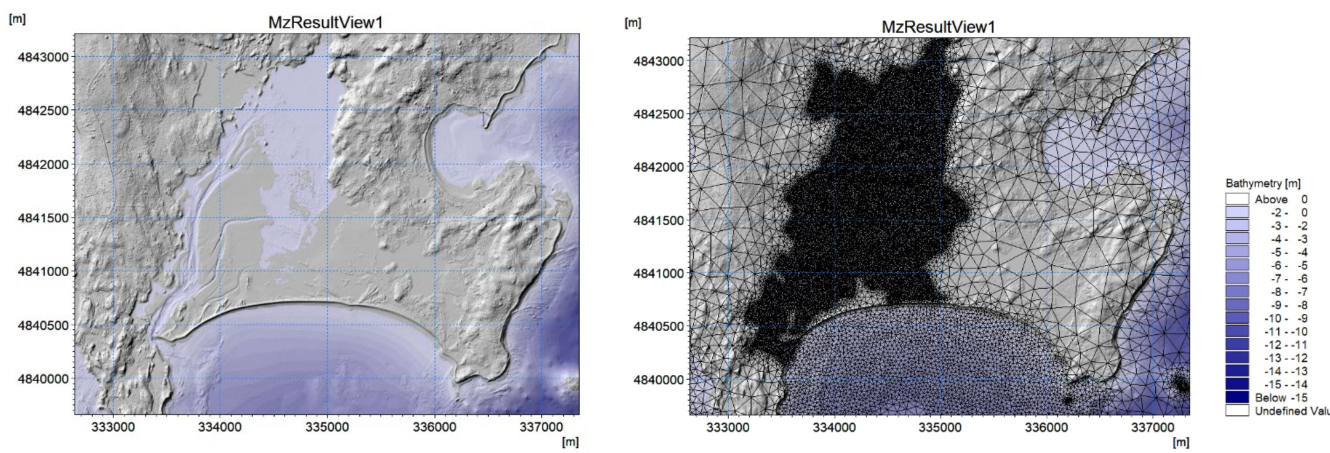

Figure 2.16: Tidal inlet without element mesh and showing the variable resolution of the mesh. The back inlet and the approach to the inlet were assigned finer resolution mesh than the surrounding area: local maximum element area 100 m^2 and 1000 m^2, respectively.

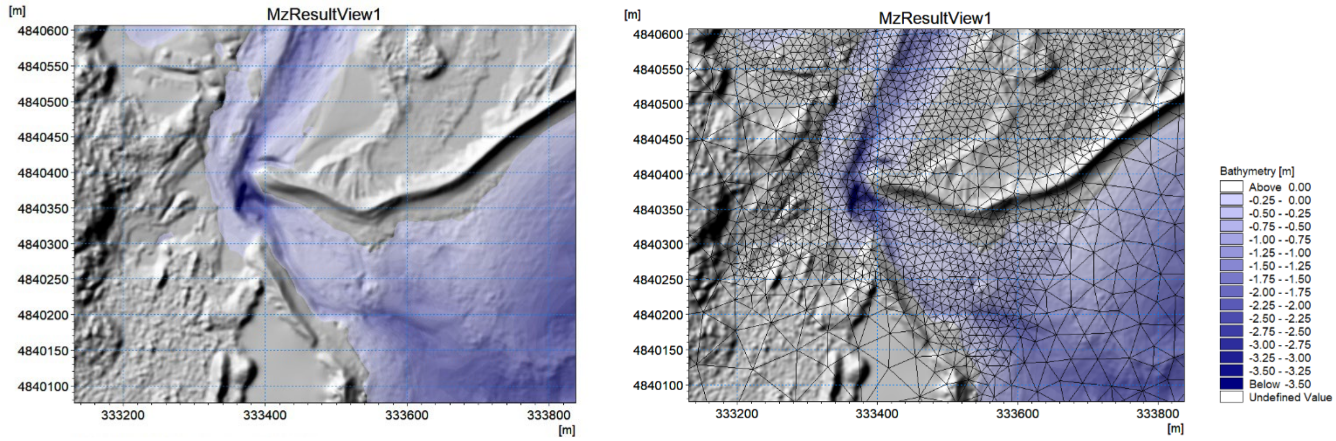

Figure 2.17: Closer inspection of the tidal inlet without element mesh and showing the variable resolution of the mesh. The back inlet and the approach to the inlet were assigned finer resolution mesh than the surrounding area: local maximum element area 100 m^2 and 1000 m^2, respectively.

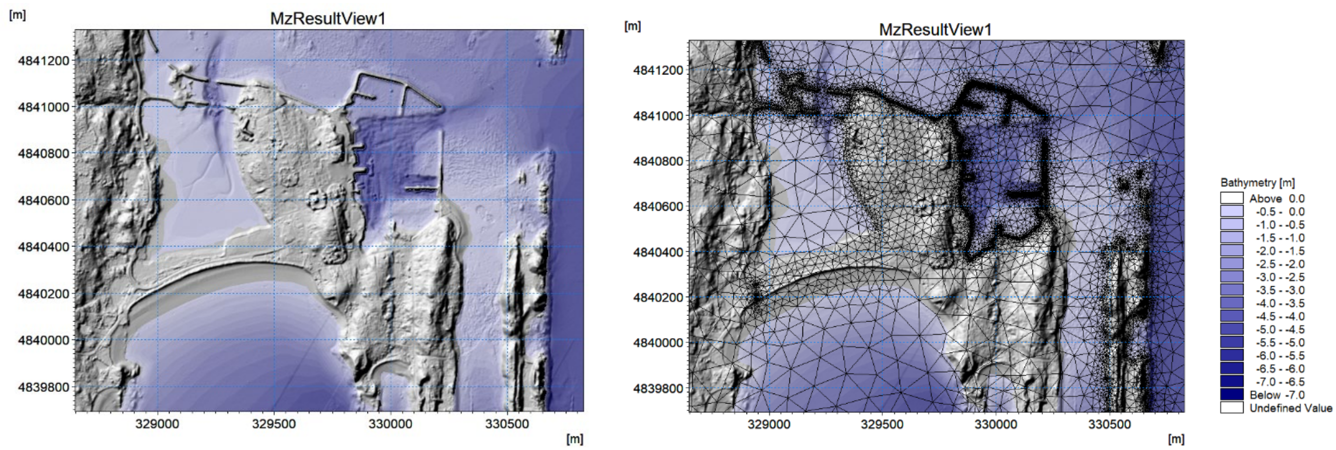

Figure 2.18: Lockeport Harbour without element mesh and showing the variable resolution of the mesh. The harbour infrastructure and surrounding islands and shoreline were assigned finer resolution mesh than the surrounding area: local maximum element area ranged from 100 m^2 to 1000 m^2.

Parameter	Value: Defaults
Simulation period	July 28 2017 3:30 AM – August 1 2017 3:30 AM
Time Step interval	60 sec
Enable flood and dry	Drying depth 0.01 m Flooding depth 0.05 m Wetting depth 0.1 m
Density	Function of temperature Reference temperature: 14˚C Reference salinity: 30.5 PSU Horizontal dispersion: constant scaled eddy viscosity formulation Initial conditions: determined from CTD and satellite data Boundary condition: constant temperature 6˚C
Eddy viscosity	Smagorinsky formulation, Constant 0.28 Minimum eddy viscosity: 0.033 m^2/s Maximum eddy viscosity: 10 m^2/s
Resistance	Manning number. Constant value 32 $m^{1/3}/s$
Coriolis	Varying in domain
Wind	Varying in time, constant in domain for calibration simulation
Wind friction	Varying with wind speed: 0.001255 at 7 m/s 0.002425 at 25 m/s
Precipitation	None
Wave radiation	None
Initial Conditions	Surface elevation: 0.8 m u-velocity: -0.1 m/s v-velocity: -0.05 m/s
Boundary Conditions	Flather condition Velocity and water level varying in time and along boundary, as predicted using WebTide

Table 2.4: HD Model calibration parameters

ADCP results were used to inform the choice of 2D or 3D model setup (Figure 2.19, Figure 2.20). At the shallow location the current was distributed over several directions over the water column, whereas at the deep ADCP location the flow was more homogenous, flowing mainly towards the northeast at all depths. Although the flow at the shallow ADCP and western portion of the study area may have been better represented by a 3D model, the deep ADCP observations showed that the flow near the critical area of interest, the Matthews Lake tidal inlet, would be well-modelled using a 2D model.

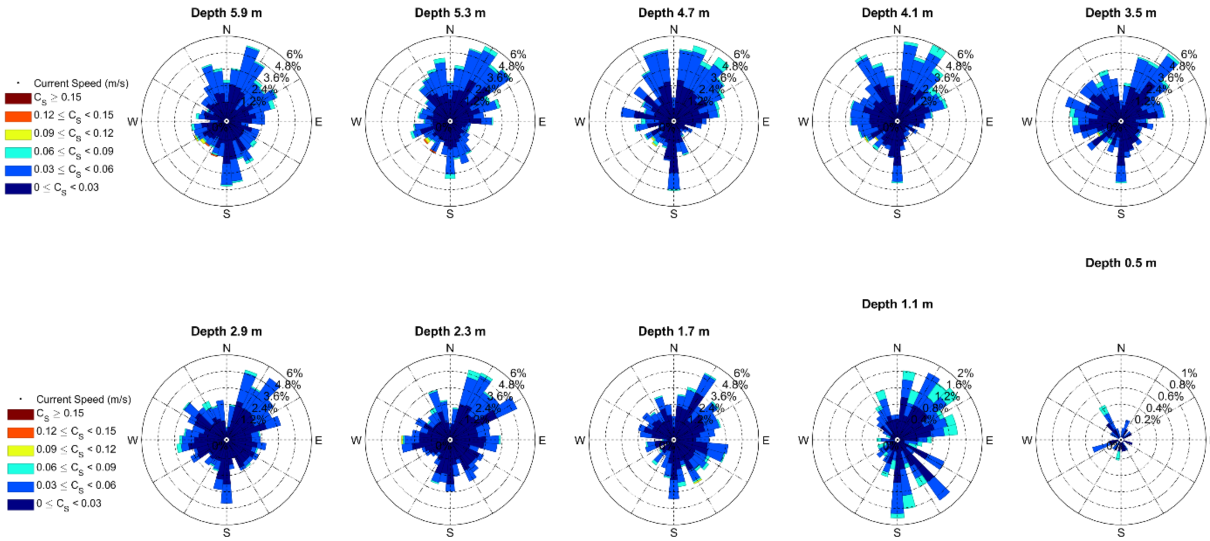

Figure 2.19: Current roses for depth bins of the Shallow ADCP. Flow was mainly towards the northwest, but there was also considerable flow moving in other directions.

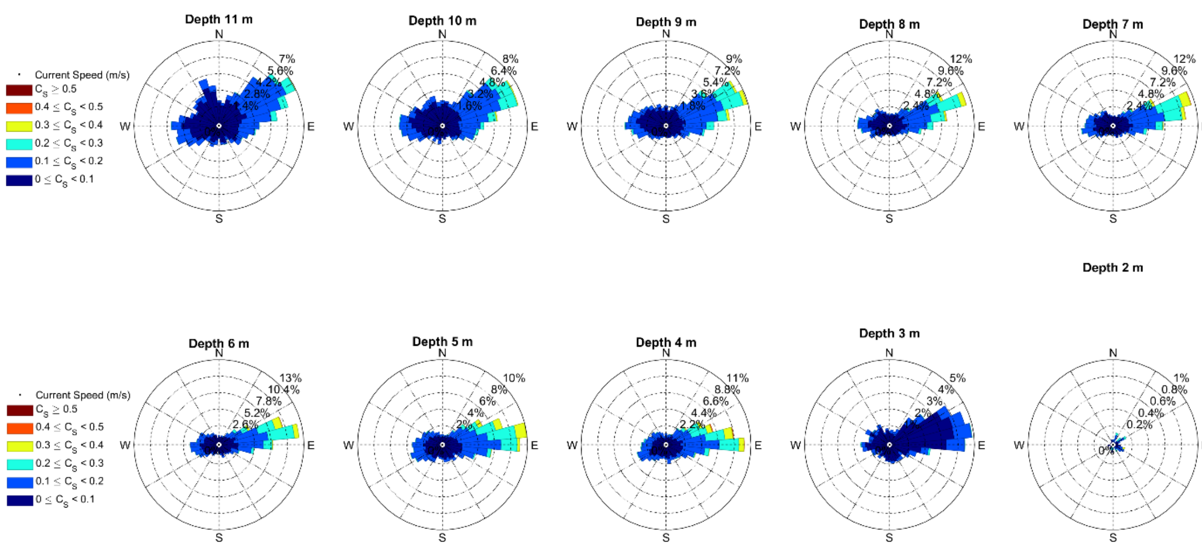

Figure 2.20: Current roses for depth bins of the deep ADCP. Flow at all depths was mainly towards the NE.

A baroclinic density scheme was used in order to represent the changes in flow resulting from varied ocean properties with depth as observed in the CTD data. A thermocline was observed in CTD (Figure 2.21) and the strong relationship between temperature and depth (Figure 2.22b). Effects of salinity were not included because a strong halocline was not observed (Figure 2.21) and salinity was not found to be depth dependent (Figure 2.22a). The linear regression model for temperature was used to predict temperature throughout the study area using lidar bathymetry for depth values (Figure 2.22c). Satellite imagery for the summer months was used to determine a minimum temperature value of 6˚C. The estimated temperature values were interpolated to the model mesh to generate an initial temperature file for model forcing. It was determined that a depth-dependent temperature boundary condition did not have an effect on model results, so a constant value of 6˚C was used.

For the calibration simulation hourly wind observed at the ECCC Liverpool meteorological station was used (Figure 2.25). Initial water level and current values were extracted from the deeper ADCP. The land boundary was closed, and was placed away from the coast in order to allow the simulation to include the shoreline in a situation where contaminants spilled into the beach region, for example; the open boundary extended south approximately 5 km from the end of the land boundary (Figure 2.24). A Flather boundary condition was used with WebTide predicted water level and currents at the western and eastern edges of the study area (Dupont et al., 2002) (Figure 2.26). The Flather condition is very efficient for downscaling coarse model simulations to local areas and overcoming instabilities at the boundary (DHI Water & Environment, 2013). During the calibration process the eddy viscosity and bed resistance were varied considerably to overcome instability at the boundary; however, these issues were ultimately overcome by utilizing the Flather boundary condition. Once the boundary issue was resolved, variations in eddy viscosity and bed resistance did not have a strong effect on model output and were returned to default values.

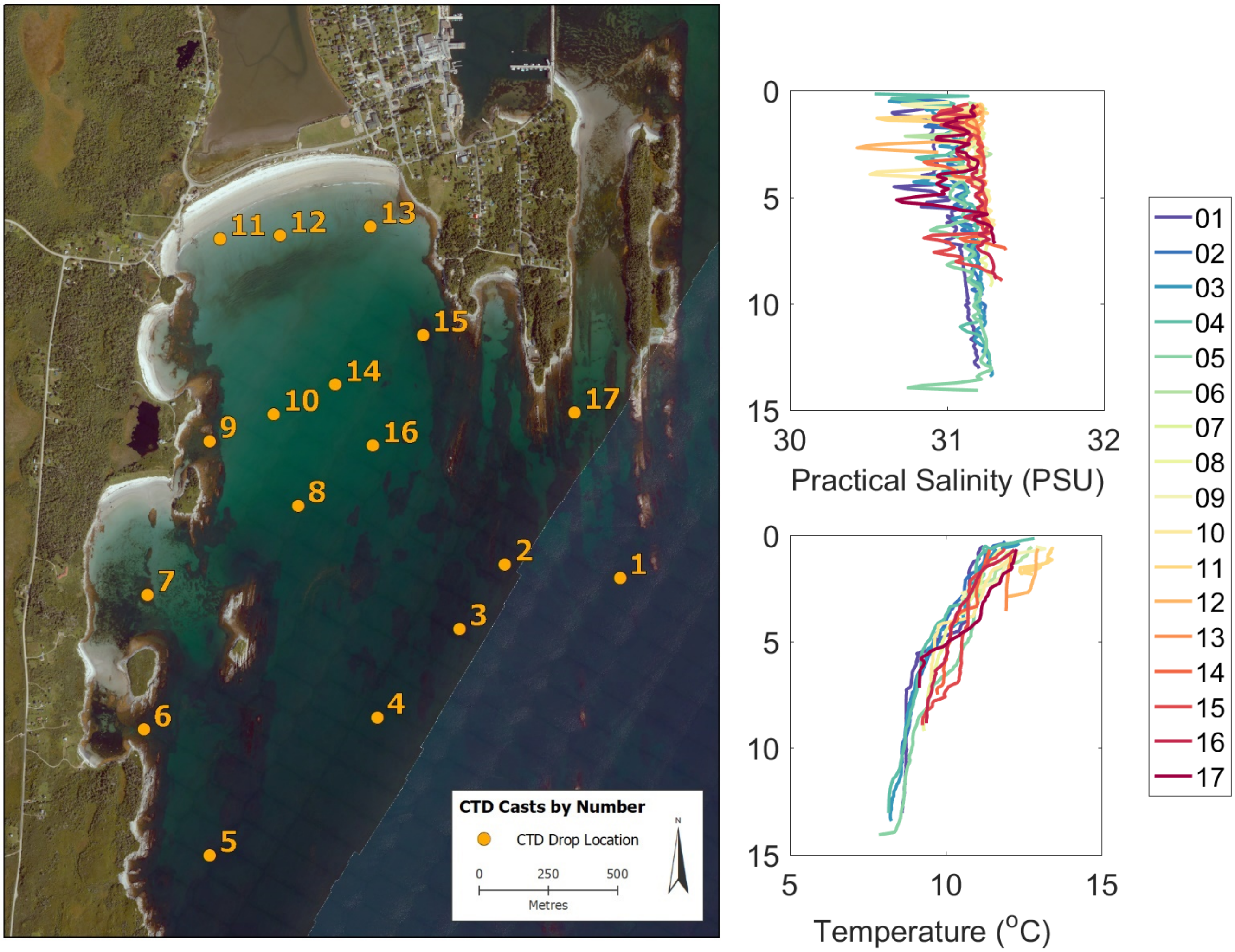

Figure 2.21: CTD cast numbers (left) and data (right).

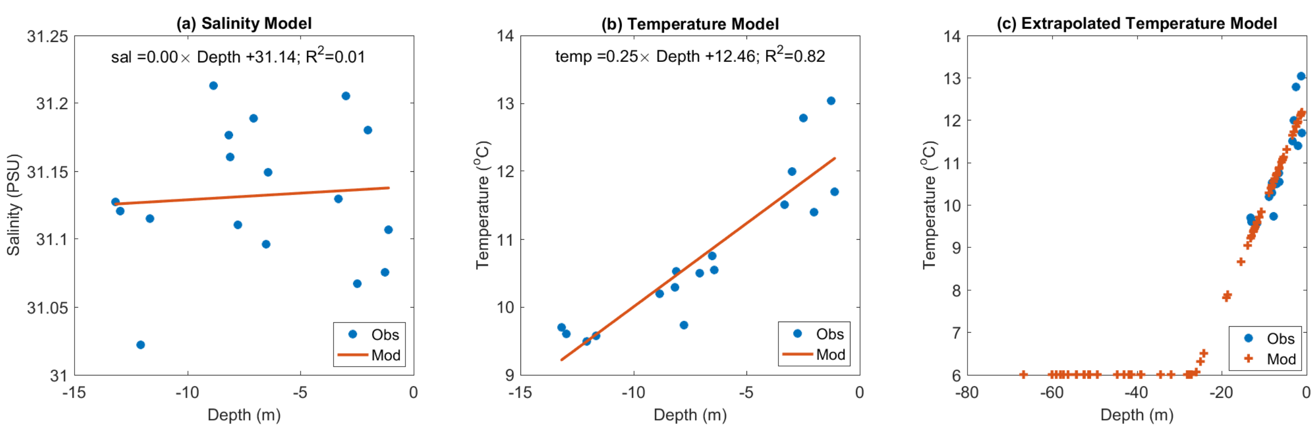

Figure 2.22: Regressions for observed salinity (a) and temperature (b) with depth; the temperature-depth model applied to greater depths (c).

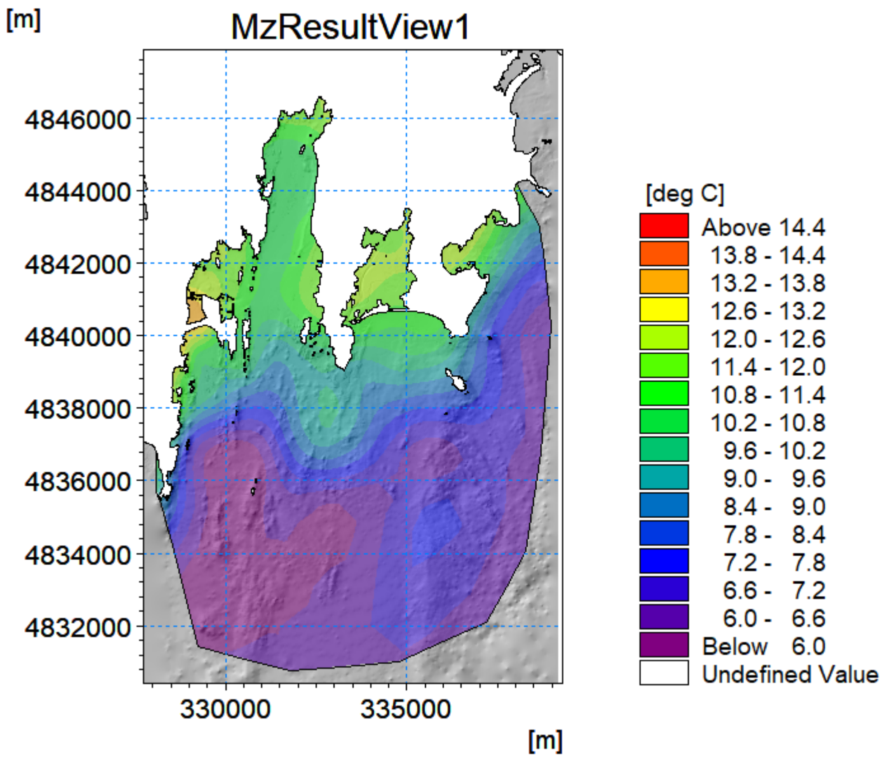

Figure 2.23: Initial temperature grid generated using the observed relationship between temperature and depth.

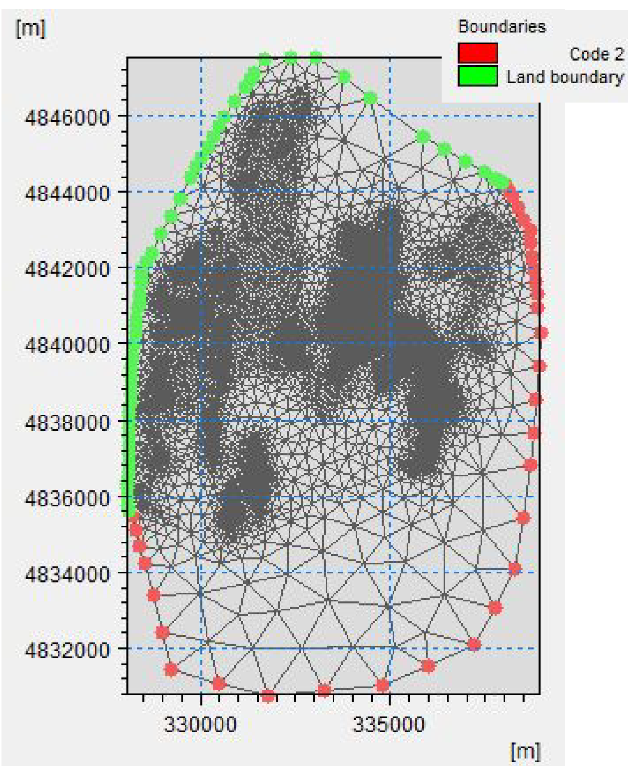

Figure 2.24: Model boundaries.

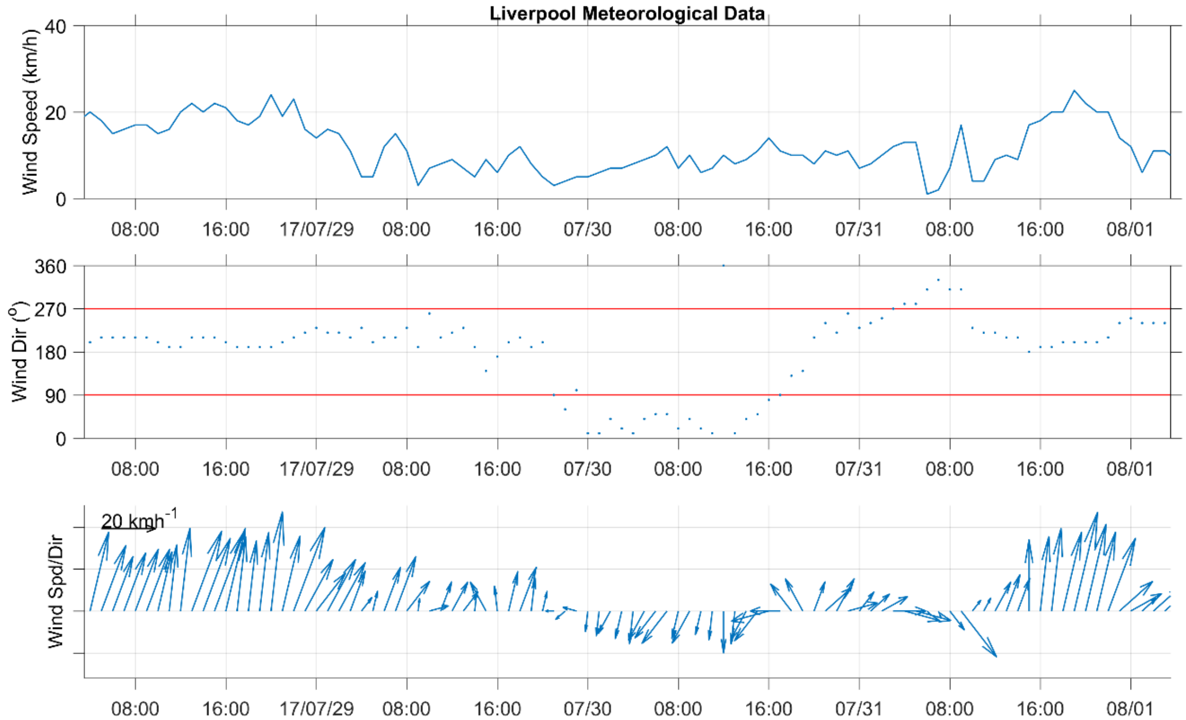

Figure 2.25: Wind speed and direction for model calibration.

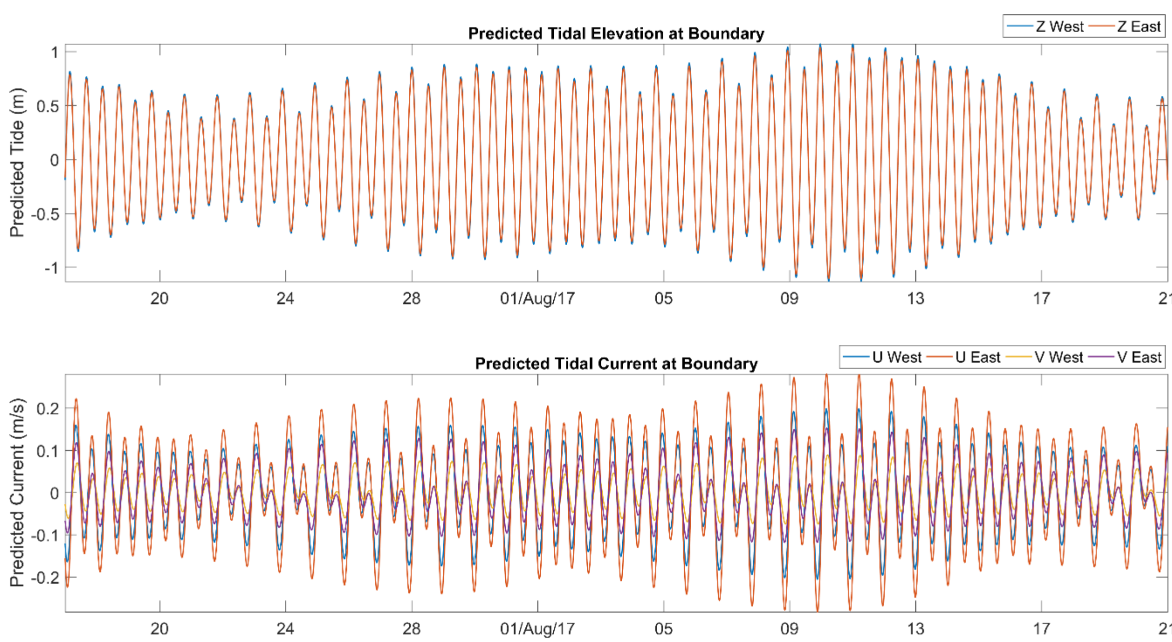

Figure 2.26: Predicted tidal elevations (top) and currents (bottom) during model simulations.

2.7.2 Spill Simulations

The Mike 21 FM Particle Tracking (PT) module was used to simulate oil spills within the study area. Parameterization of the PT module is summarized in Table 2.5. The model also included density and bed roughness from HD model, and settling of particles was set to include flocculation. Two scenarios were simulated in the PT modelling to represent typical winter and summer wind conditions as described in Horn and French-MacKay (2014) and presented in Table 2.6. The particles were released at low tide (July 28 10:00) for a duration of 5 hours. Additional scenarios were simulated to represent storm conditions. Wind speeds and directions represent major winter storms of December 2017 and January 2018 that were known to cause flooding due to storm surge at Lockeport Harbour (Figure 2.27). Particles were released from sources near the Matthews Lake tidal inlet and in an area offshore.

Class	Description	Decay (particles/s)	Settling Velocity (m/s)	Horizontal Dispersion (m^2/s)	Erosion (N/m^2)	Flux (kg/s)	Particles per Δt
Type 2	Light Oils (Diesel, No. 2 Fuel Oil, Light Crudes)	1e-005	0.1	8	0.01	100	20
Type 3	Medium Oils (Most Crude Oils)	1e-006	0.1	4	0.01	1,000	100
Type 4	Heavy Oils (Heavy Crude Oils, No. 6 Fuel Oil, Bunker C)	1e-007	0.1	2	0.01	10,000	1,000

Table 2.5: Settings for Particle Tracking modelling.

Scenario	Wind Description	Speed (m/s)	Speed (km/hr)	Knots	Direction	Particle Release Time	Tide at release	Source
1	Strong winter wind	10	40	20	NW (315)	July 28 10:00	LT	Horn and French-MacKay (2014)
2	Moderate summer wind	5	20	10	SW (225)	July 28 10:00	LT	Horn and French-MacKay (2014)
3	Winter storm 1	25	90	48	E (100)	July 28 10:00	LT	
4	Winter Storm 2	25	90	48	S (180)	July 28 10:00	LT	
5	Winter Storm with particle release at mid-tide rising	25	90	48	S (180)	July 28 12:50	MTR	

Table 2.6: Particle tracking simulation summary. LT indicates particle release at low tide, MTR indicates particle release at mid-tide rising. Times are in UTC.

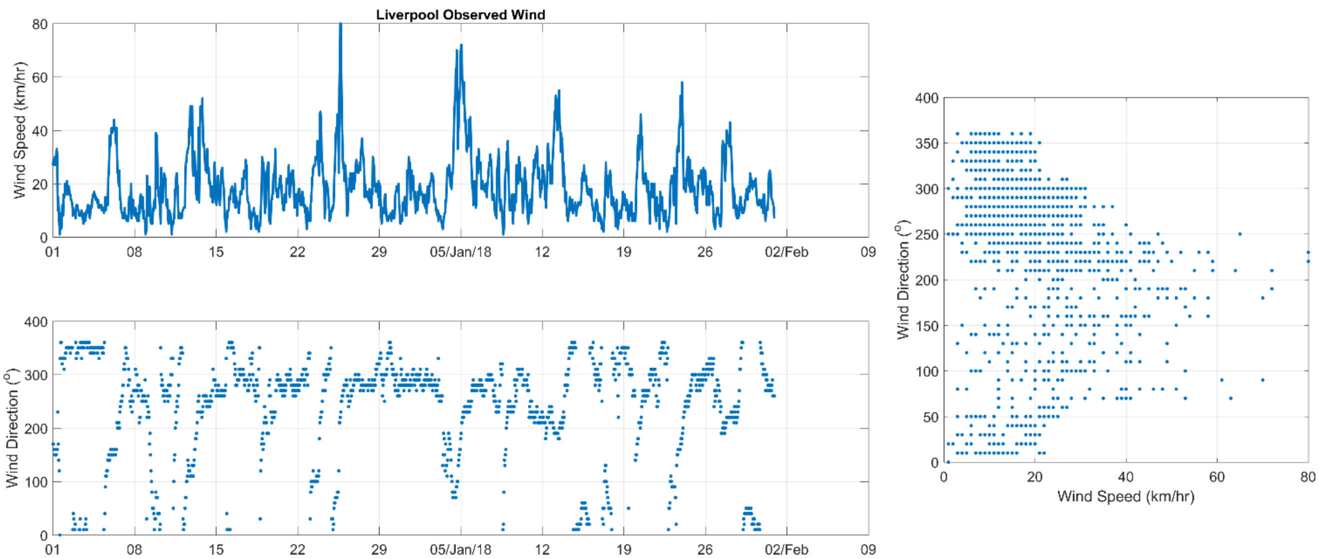

Figure 2.27: Wind speed and direction from Liverpool meteorological station. Major storms

3 Results

This section describes the lidar validation and map products, the classification validation and results, and the modelling validation and simulation results.

3.1 Lidar Results

3.1.1 Lidar Validation

Topographic ground truth data (3873 data points) were collected for lidar validation along the shoreline at Matthews Lake and on roads throughout the study area (Figure 3.1). Elevations were compared to lidar elevations and had a mean difference of -0.08 m, with standard deviation of 0.051 m. Bathymetry points (31 total) were collected throughout the study area to compare with the lidar bathymetry data (Figure 3.2); mean Δz was -0.21 m and standard deviation was 0.116 m. The overall validation (topography and bathymetry validation points) had a mean difference of -0.08 m, and standard deviation of 0.054 m (3904 data points).

Bottom profile information acquired using the RiverRay ADCP for the Matthews Lake channel were used to validate the lidar bathymetry. The lidar agreed with the observed bathymetry very well, mean Δz was 0.05 m and standard deviation was 0.04 m for the ~60 m wide channel (Figure 3.3).

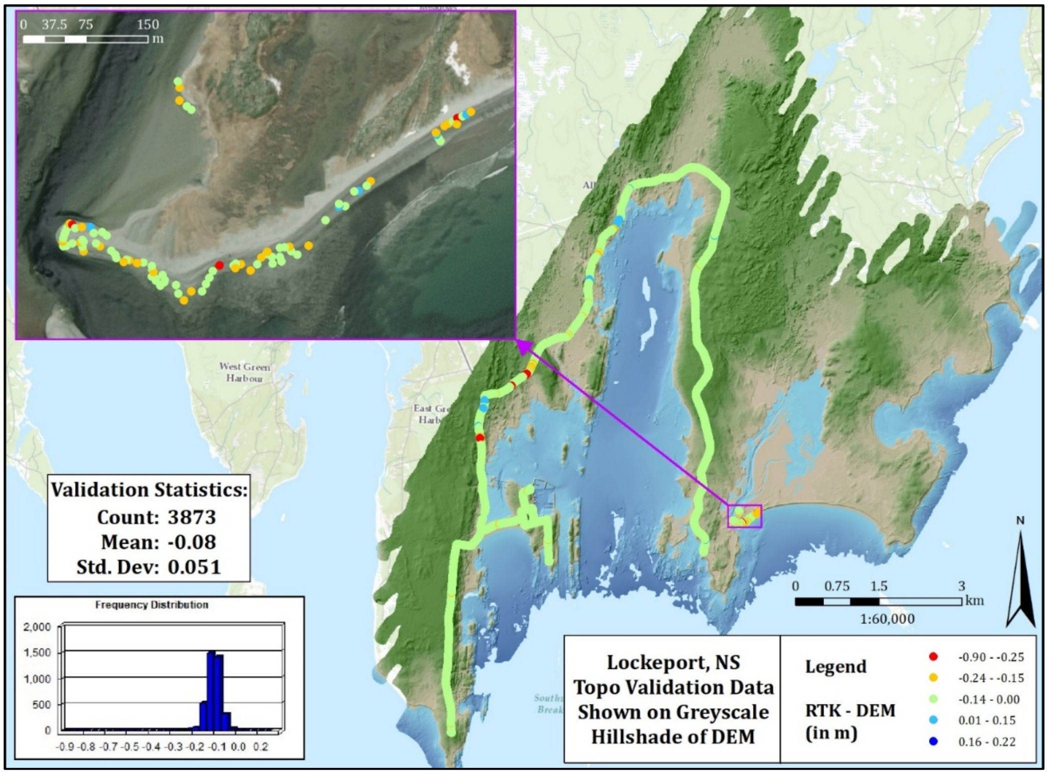

Figure 3.1: Lidar topography validation throughout the study area. Mean Δz was -0.08 m, standard deviation was 0.05 m.

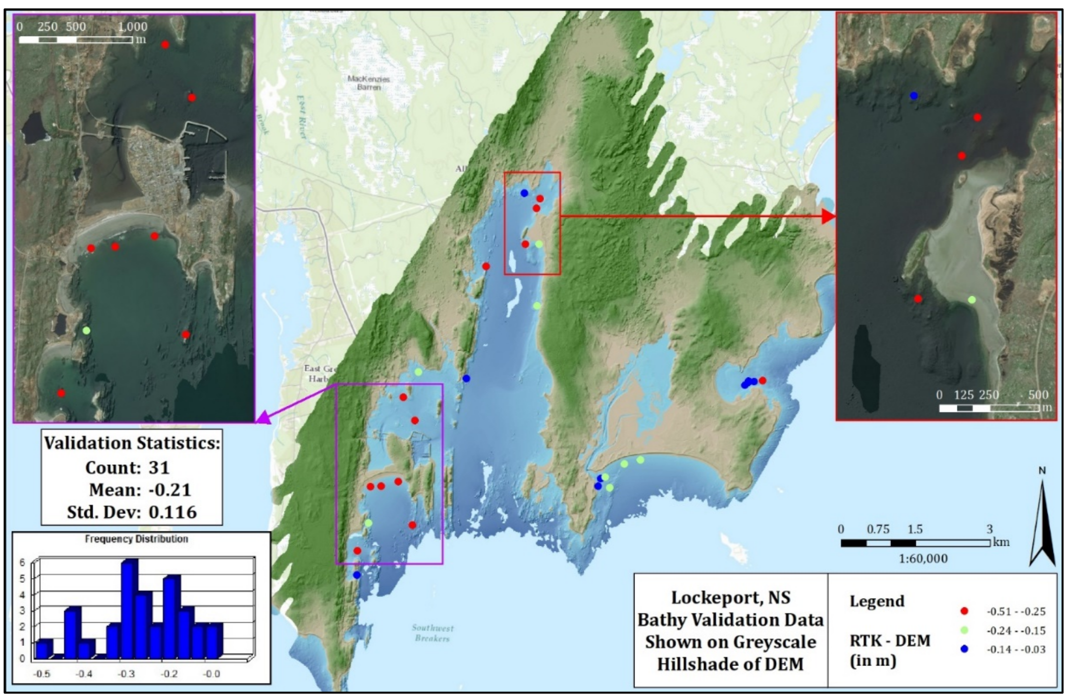

Figure 3.2: Lidar bathymetry validation throughout the study area. Mean Δz was -0.21 m, standard deviation was 0.12 m.

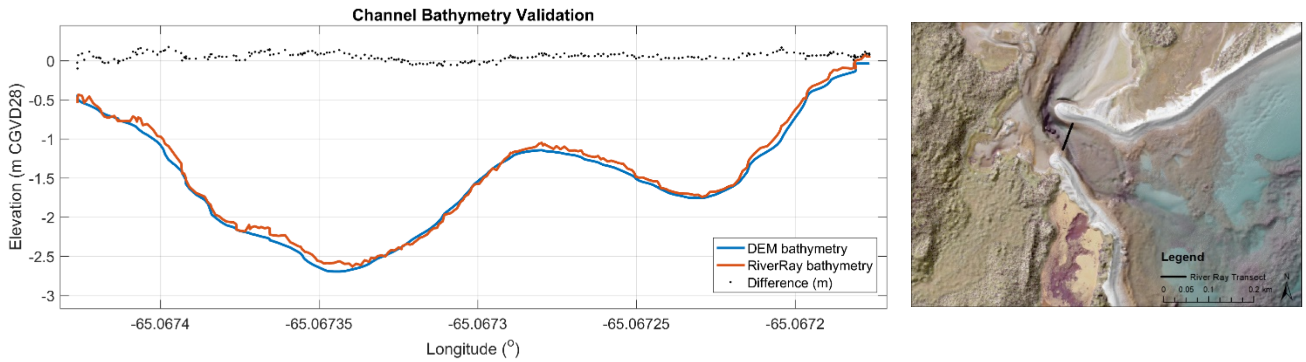

Figure 3.3: Validation of lidar bathymetry at the channel compared to river ray bottom track.

3.1.2 Lidar Products

The lidar survey achieved a bathymetric maximum of -15.25 m CGVD28 (Figure 3.5). Bathymetry at Lockeport Harbour was relatively flat, between -8 m and -6 m. The tidal inlet (Matthews Lake) was shallow, with exposed sand having elevation of between 0 and 1 m, the water outside of the channel was between -1 and 0, and the channel ranged from between -3.5 and -1 m (Figure 3.5). A large portion of the study area (26%, or 7.85 km^2) was shallow, falling between -1 and 1 m, and another 25% (7.6 km^2) was between -9 m and -6 m (**Error! Reference source not found.**, Table 3.1).

The Colour Shaded Relief Model displays the elevation data draped over a hillshade with a 5x vertical exaggeration applied (Figure 3.6). The hillshade uses two colour ramps to delineate the topography and bathymetry and highlights the features of the land or seabed such as rough shoals, smooth and flat areas, or areas of likely dredging.

The lidar intensity map is a representation of the light reflected off the land or seabed (Figure 3.7). Lighter sections represent more reflective seabed material such as sand, and darker sections represent less reflective seabed material, such as vegetation. This data product was a key component in the classification of seabed material discussed in Section 2.6.2.

The imagery acquired with the RCD30 camera during the lidar survey does not result in an appealing mosaic due to issues merging imagery from the two different survey days (Figure 3.8); however, the 5 cm imagery is still invaluable for examination at a close scale and was an integral part of the shoreline and benthic material classification discussed in Section 2.6 and presented in Section 3.2. The False Colour Composite imagery, which represents vegetation as a bright red colour, was also important for the classification process (Figure 3.9).

Lower Contour Limit	Upper Contour Limit	Area (km^2)
0	1	3.98
-1	0	3.87
-2	-1	2.49
-3	-2	2.55
-4	-3	2.23
-5	-4	1.94
-6	-5	2.02
-7	-6	2.55
-8	-7	2.64
-9	-8	2.43
-10	-9	1.01
-11	-10	0.81
-12	-11	0.61
-13	-12	0.37
-14	-13	0.26
-15	-14	0.075
-16	-15	0.002
TOTAL		**29.82**

Table 3.1: Area (km^2) of depth contours.

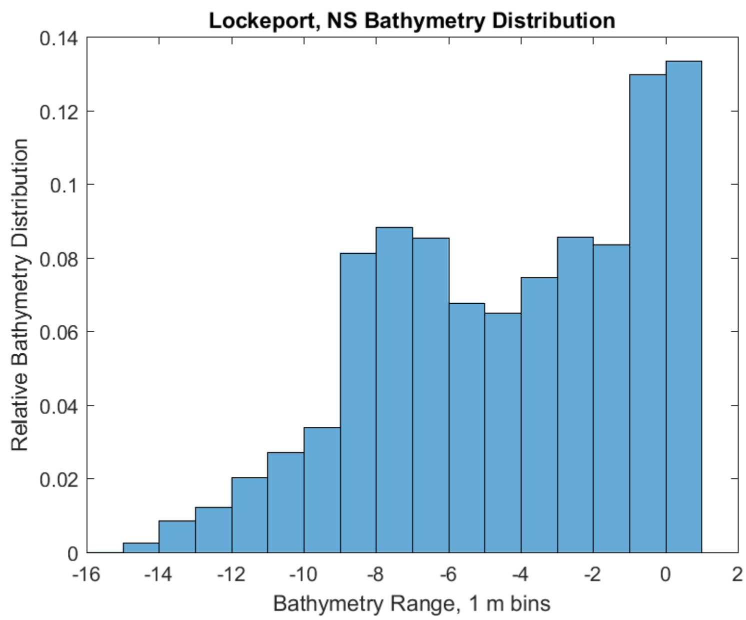

Figure 3.4: Bathymetry distribution: 26% of the bathymetry falls between -1 m and 1 m, and another 25% has elevation between -9 m and -6 m.

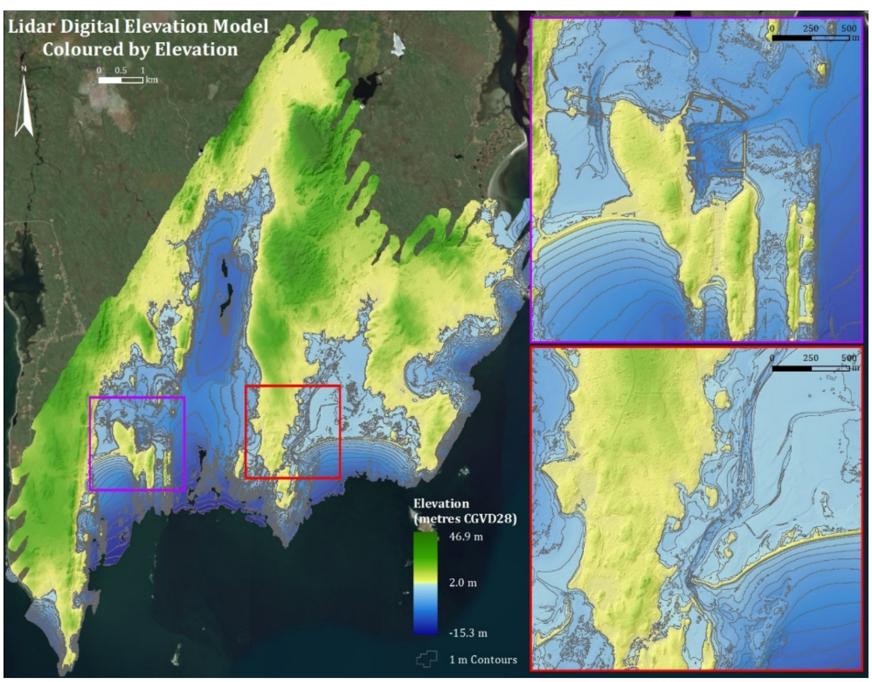

Figure 3.5: Digital Elevation Model for the entire study area and for two smaller areas. Depth contours at 1 m intervals are shown to emphasize slope and gradient. The maximum lidar penetration was -15.3 m CGVD28, and the highest topographic elevation was 46.9 m CGVD28.

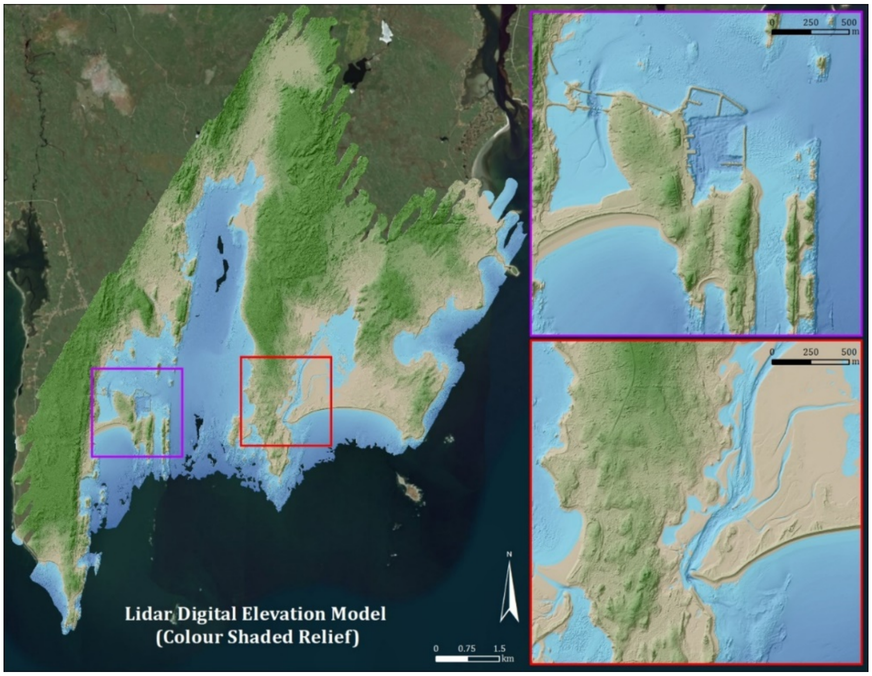

Figure 3.6: Digital Elevation Model/Colour Shaded Relief for the entire study area and for two smaller areas. Topographic elevations are represented by beige and green colours (beige = lower elevation, dark green = maximum elevation), and bathymetric elevations are represented by blues (darker blue = deeper water).

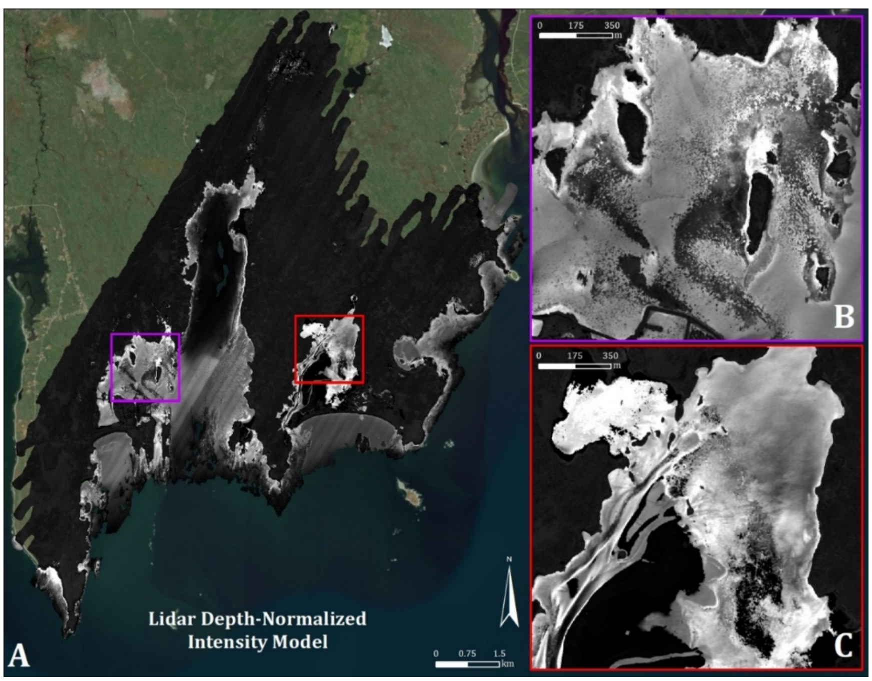

Figure 3.7: Lidar Intensity Model for the entire study area and for two smaller areas. Lighter sections represent more reflective seabed material such as sand, and darker sections represent less reflective seabed material, such as vegetation.

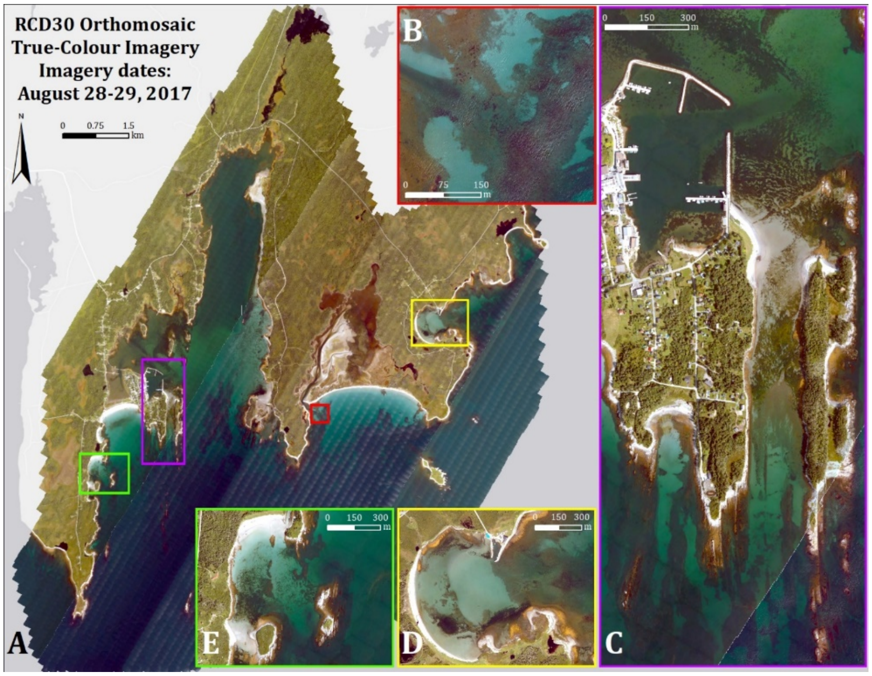

Figure 3.8: True Colour Mosaic from RCD30 camera. The insets highlight different bottom types and shoreline materials.

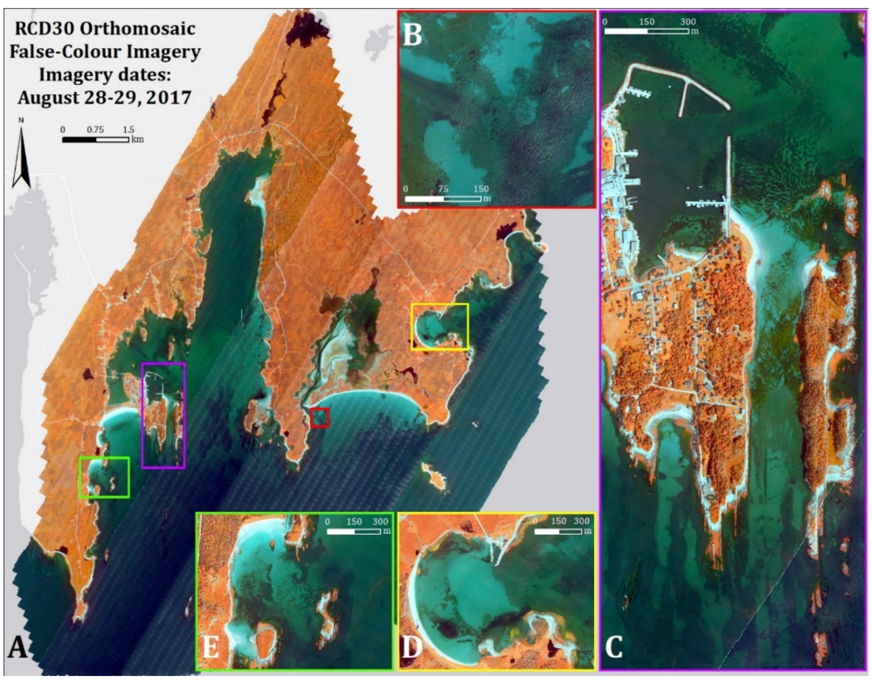

Figure 3.9: False Colour Mosaic from RCD30 camera. In a False colour image the Near Infrared band replaces the Red band, resulting in bright red colour where exposed vegetation exists.

3.2 Classification

3.2.1 Shoreline classification and validation

The distribution of classes within the Matthew's Lake area of interest is described in Table 3.2. The largest classes, due to the buffering of the processing extent past the Higher High Water Large Tide mark, are marsh and vegetation with a combined area of 4.467km^2. Sediment classes represent a very small portion of the study area, combining to less than 6%. The largest sediment class is sand with an area of 0.233km^2, and area of the remaining classes reduces as grain size of substrate increases, the smallest class being bedrock with 0.008km^2. Detailed maps of the classification are shown in Figures 3.10 to 3.16.

Class	**Total area of class (km^2)**	**Percent area of class (%)**
Boulder Beach	0.050	1.0
Pebble/Cobble Beach	0.181	3.7
Sand	0.233	4.7
Vegetation	3.044	61.6
Bedrock	0.008	0.2
Marsh	1.423	28.8

Table 3.2: Shoreline classification area and percent area.

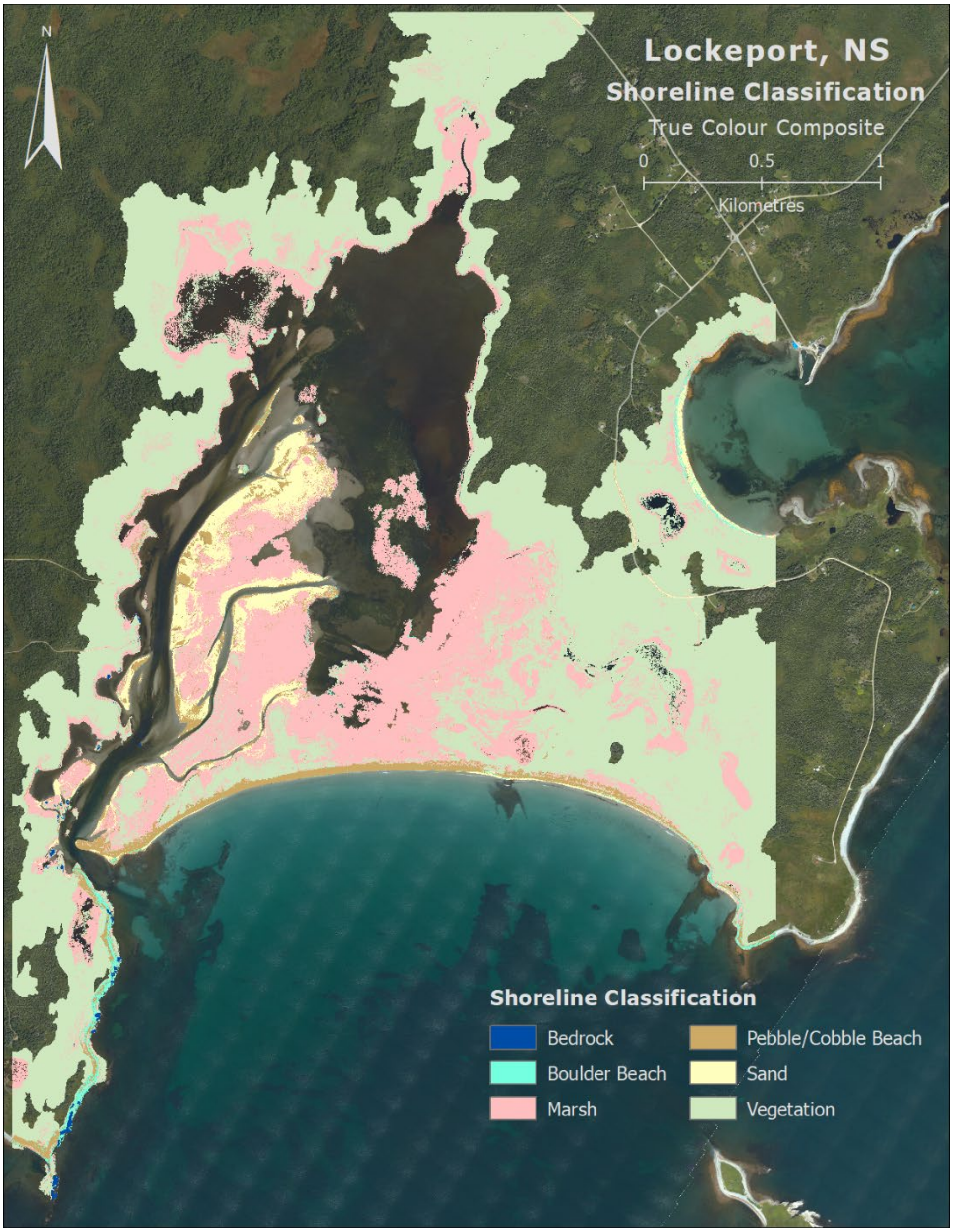

Figure 3.10: Overview of the shoreline classification of Matthew's Lake tidal inlet.

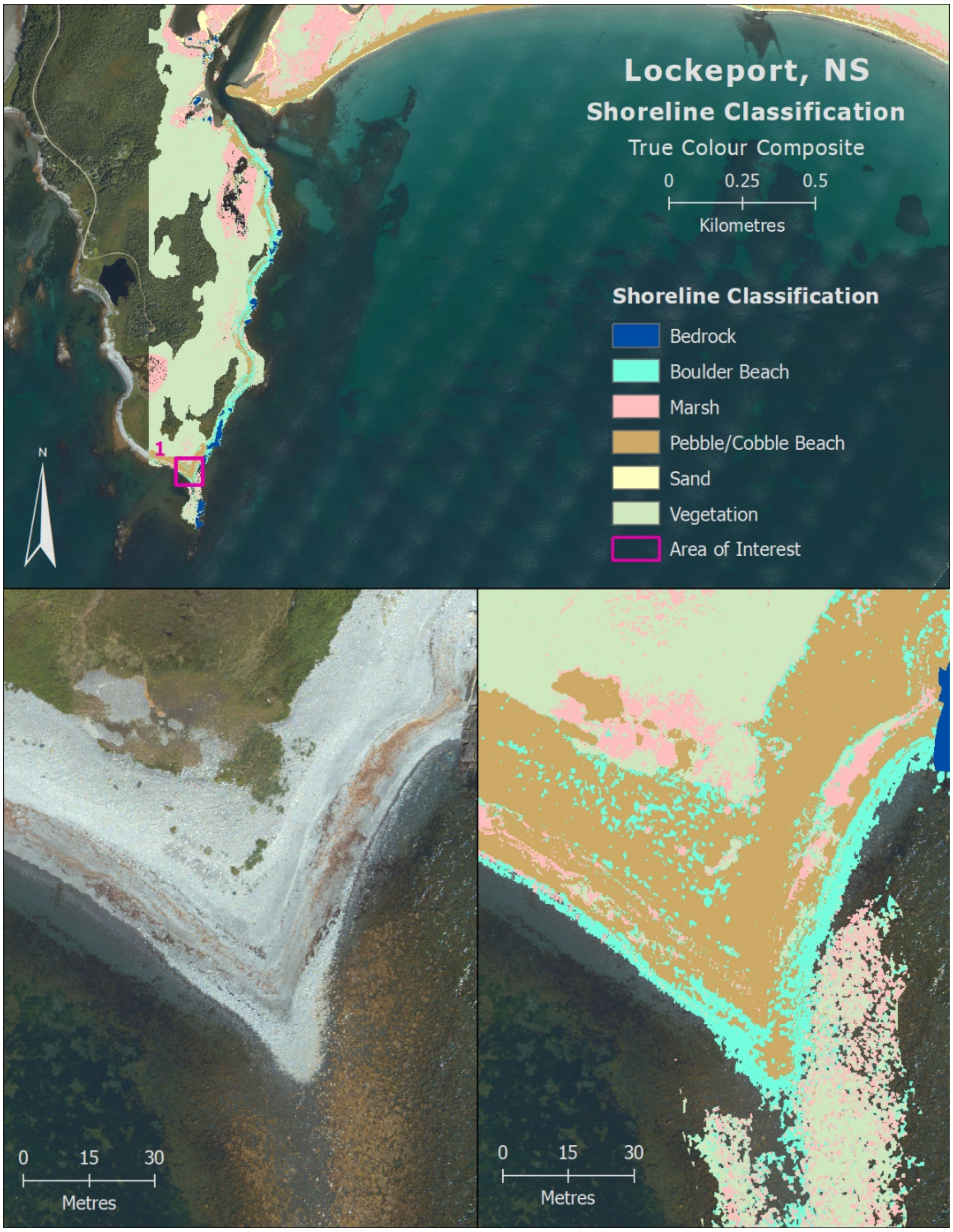

Figure 3.11: Detailed view of the shoreline classification.

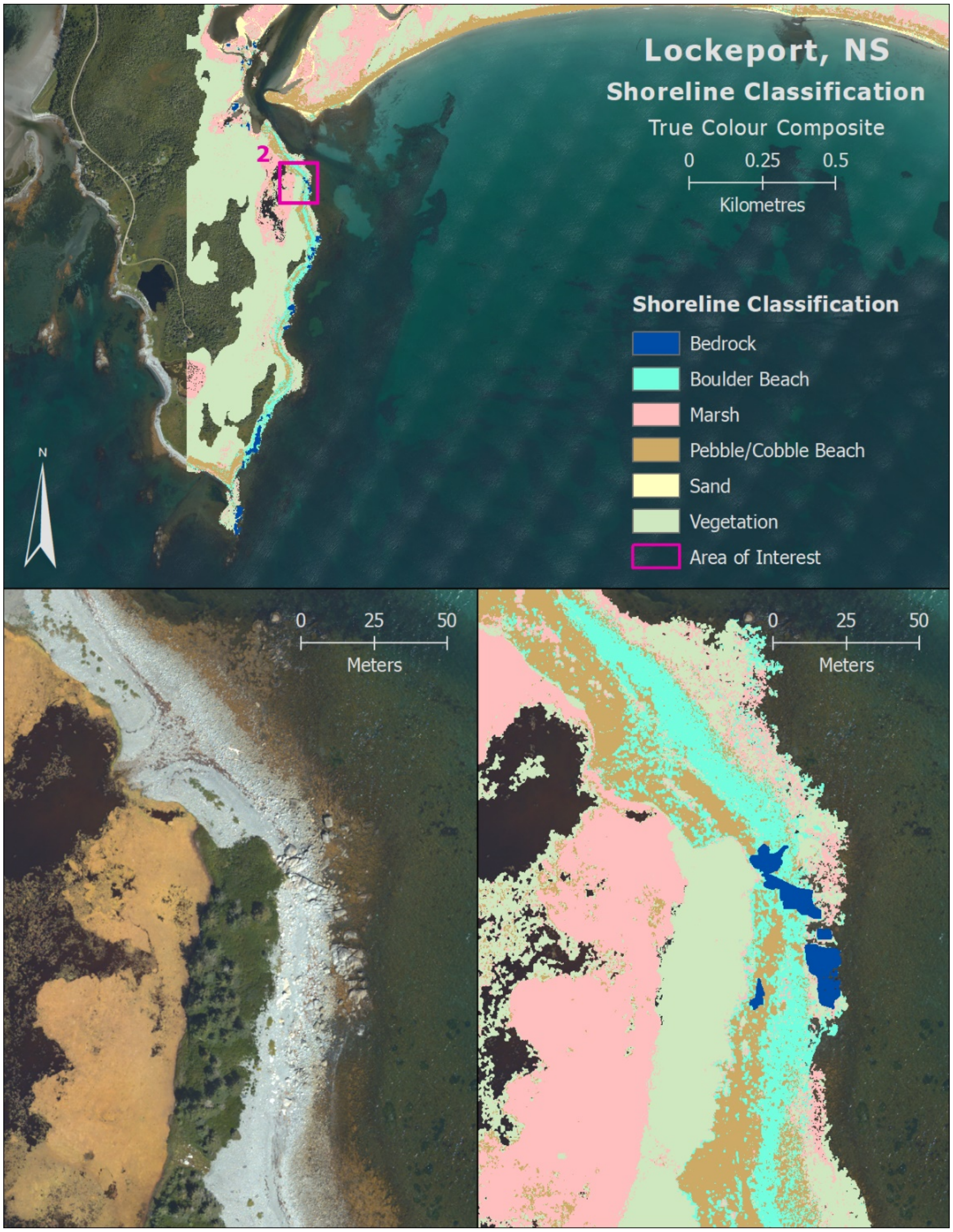

Figure 3.12: Detailed view of the shoreline classification.

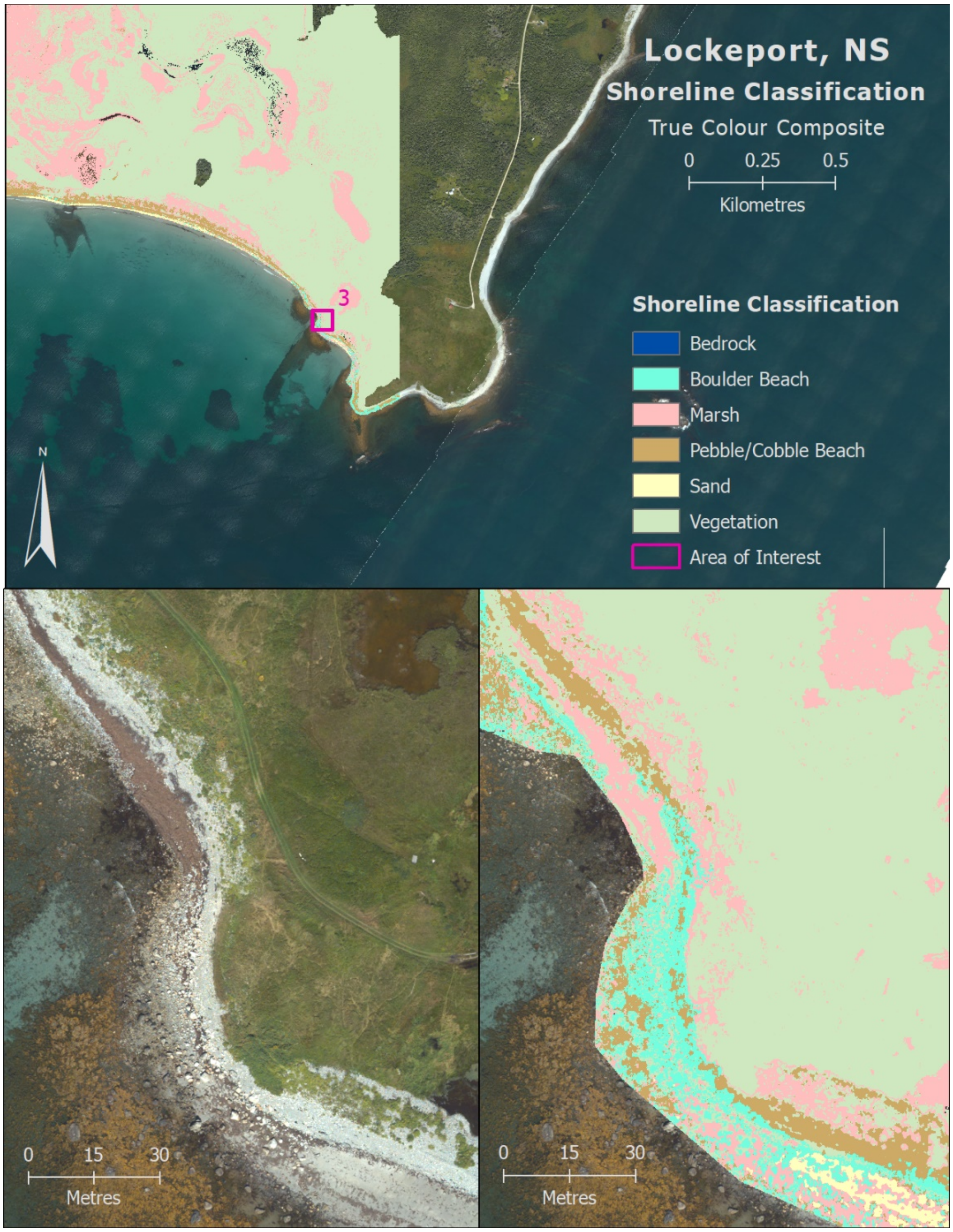

Figure 3.13: Detailed view of the shoreline classification.

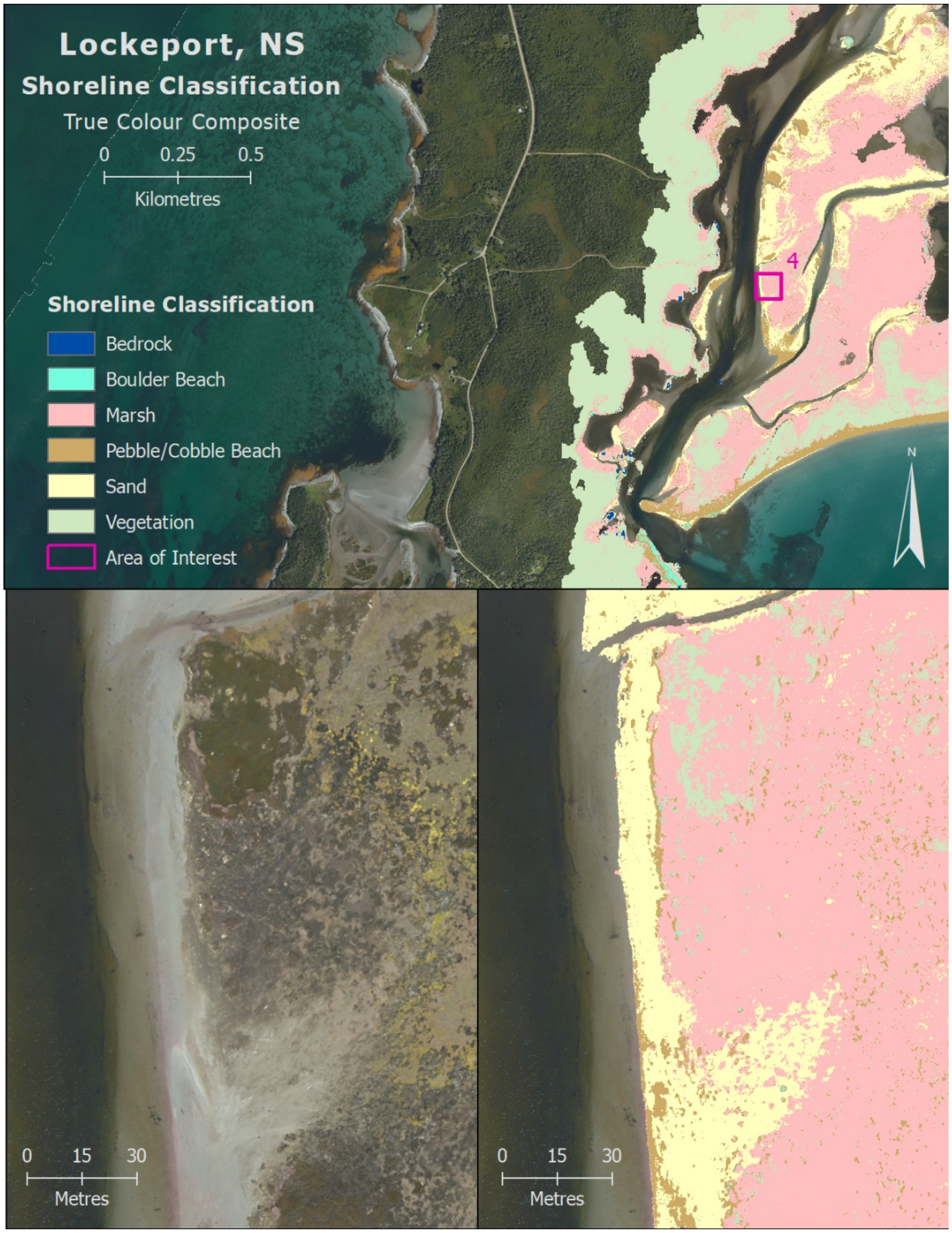

Figure 3.14: Detailed view of the shoreline classification.

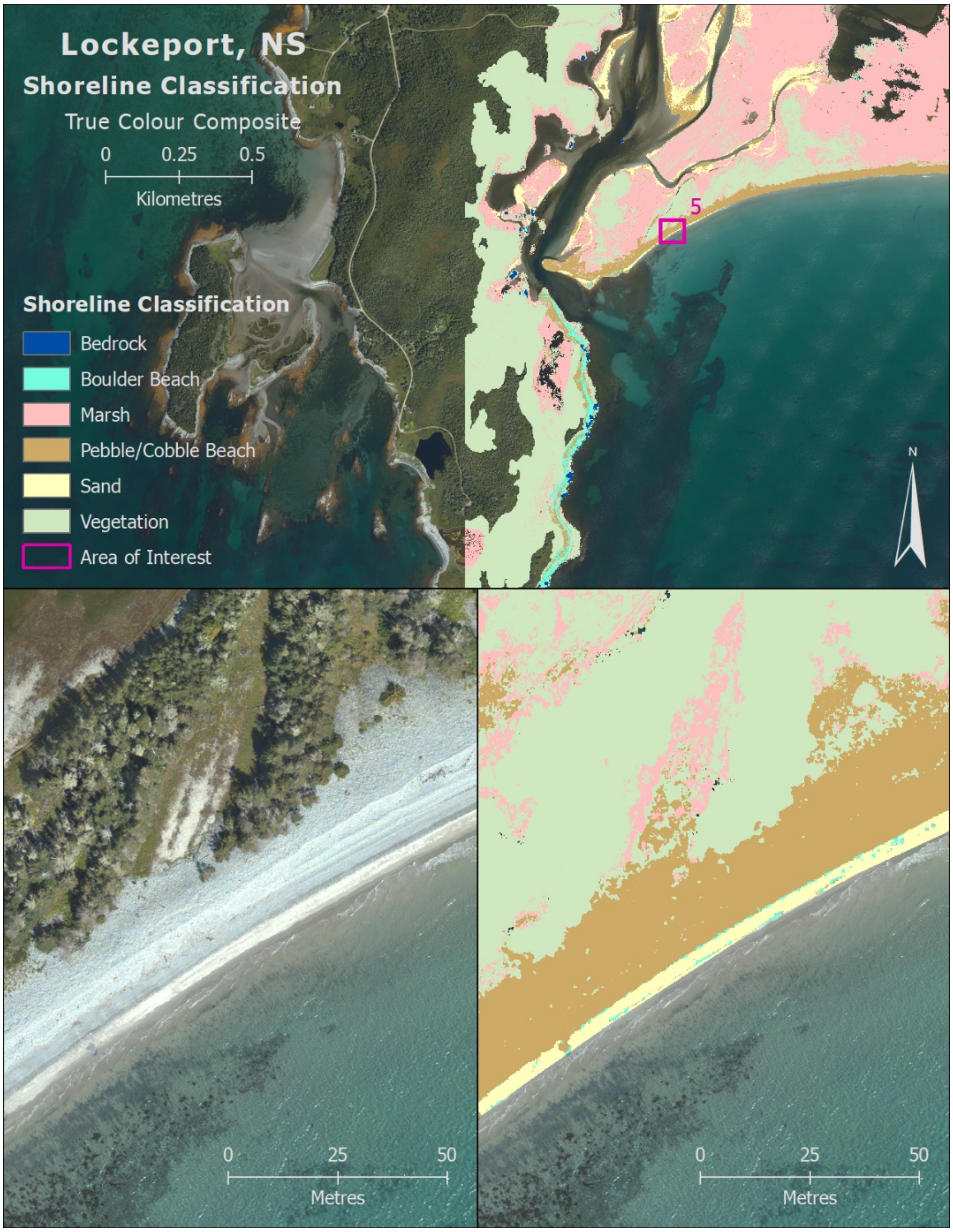

Figure 3.15: Detailed view of the shoreline classification.

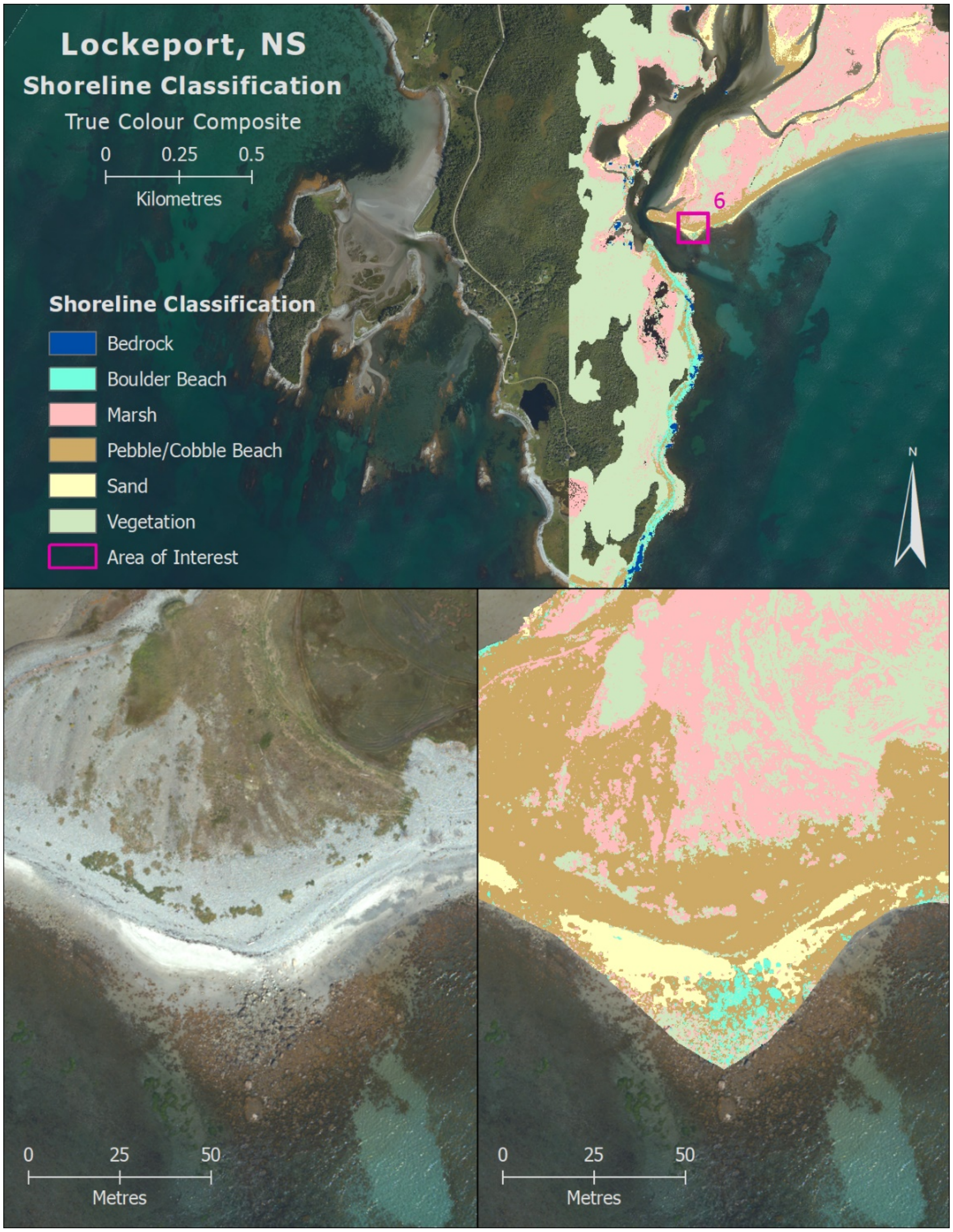

Figure 3.16: Detailed view of the shoreline classification.

The shoreline classification was validated with 61 ground truth points, using the majority substrate type in each quadrat photo. Ground truth samples were collected only within the boulder beach, pebble/cobble beach, sand and vegetation categories. The accuracy assessment is outline in Table 3.3, and shows 100% agreement in all classes other than sand, which shows a reduced agreement of 79%. Ground truth point locations and agreement results are shown in Figure 3.17

Classes that were not sufficiently represented in the ground truth data (vegetation, marsh and bedrock) were validated using 35 points located on photo identifiable features, and showed 100% agreement with the classification.

Class	**Number of quadrats identified as each ground type**	**Agreement of class with AGRG quadrat imagery**	**Agreement of class with AGRG quadrat imagery (%)**
Boulder Beach	3	3	100
Pebble/Cobble Beach	29	29	100
Sand	28	22	79
Vegetation	1	1	100

Table 3.3: Shoreline classification validation. Only quadrat images with >75% substrate homogeneity were included in the final classification validation, totaling 61 points.

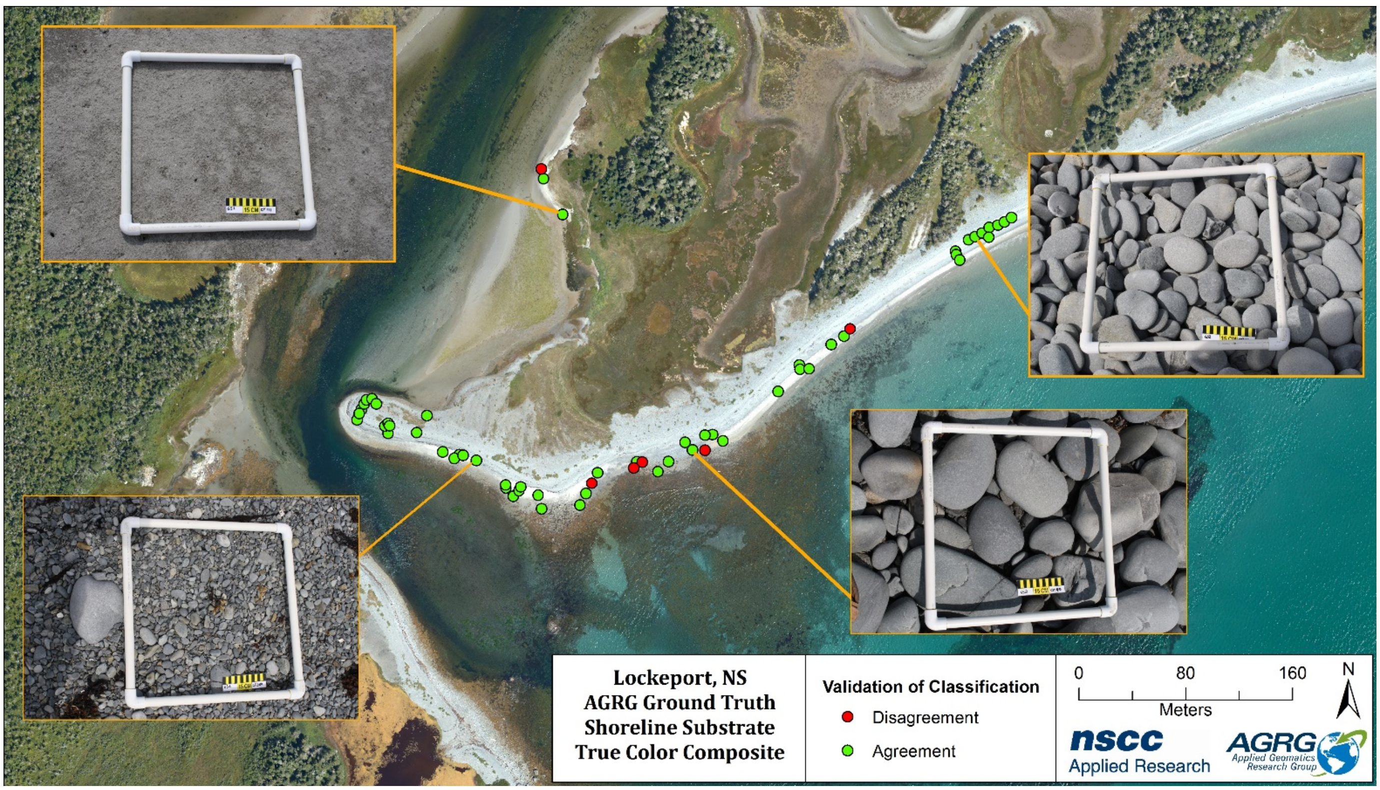

Figure 3.17: Shoreline classification ground truth points. Ground truth points that are classified correctly are green and those that are not are red.

3.2.2 Benthic classification and validation

In general, the SVM classification method outperformed the ISO classification (Figure 3.18, Figure 3.19, Figure 3.20,

Figure 3.21). Though a visual inspection the results this was most apparent in areas of notably dark waters and/or with dark bottom substrates such as the north eastern portion of the Mathews Lake and deep channels area wherein the ISO method returned a significant amount of dark muds/sands as SAV despite best efforts. Conversely, the ISO results seem to have performed slightly better returning non-SAV in the northern shallower sections of the same area. The exact reasoning for deviations in these results are complex to assess bases on the sensitivity of the clustering algorithms with regard to input layers. Both approaches performed similarly overall in the open bay with regard to rockweed and kelp differentiation from sand where the signals were consistently higher contrast. It is important to note that the ISO method exhibits a large amount of non-SAV just north of the sand bar inside the Matthews lake area relative to the SVM output. This is understood however as the manual re-classification of the ISO clusters purposely focused on classifying vegetation specifically submerged during the time of flight to facilitate good separation based fewest complicating factors in terms of depth normalization. The SVM approach however is capable of accommodating these variations though training and with an inherently more responsive clustering mechanism.

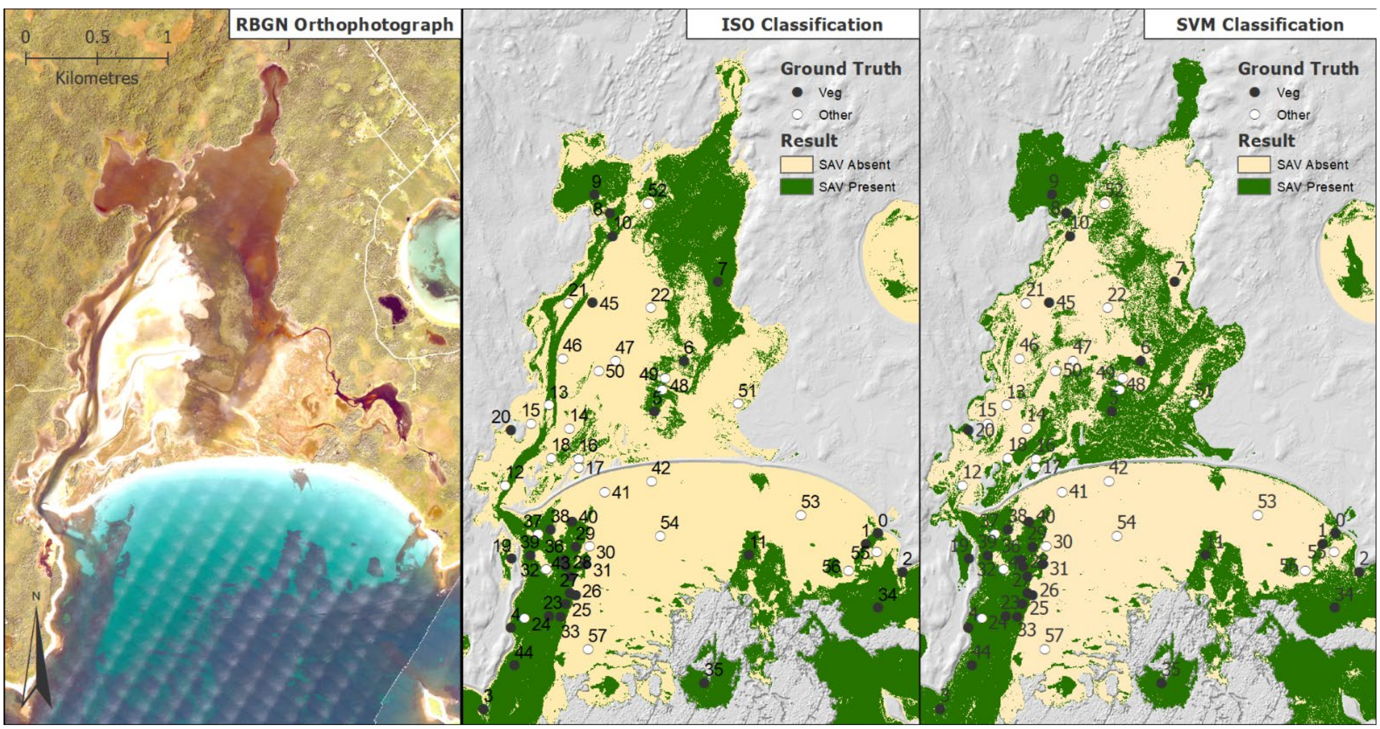

Figure 3.18: Shown are the comparison results of the two classification methods with an orthophoto mosaic (left), Iso-cluster k-mean (ISO) (middle) and Support Vector Machine (SVM) (right).

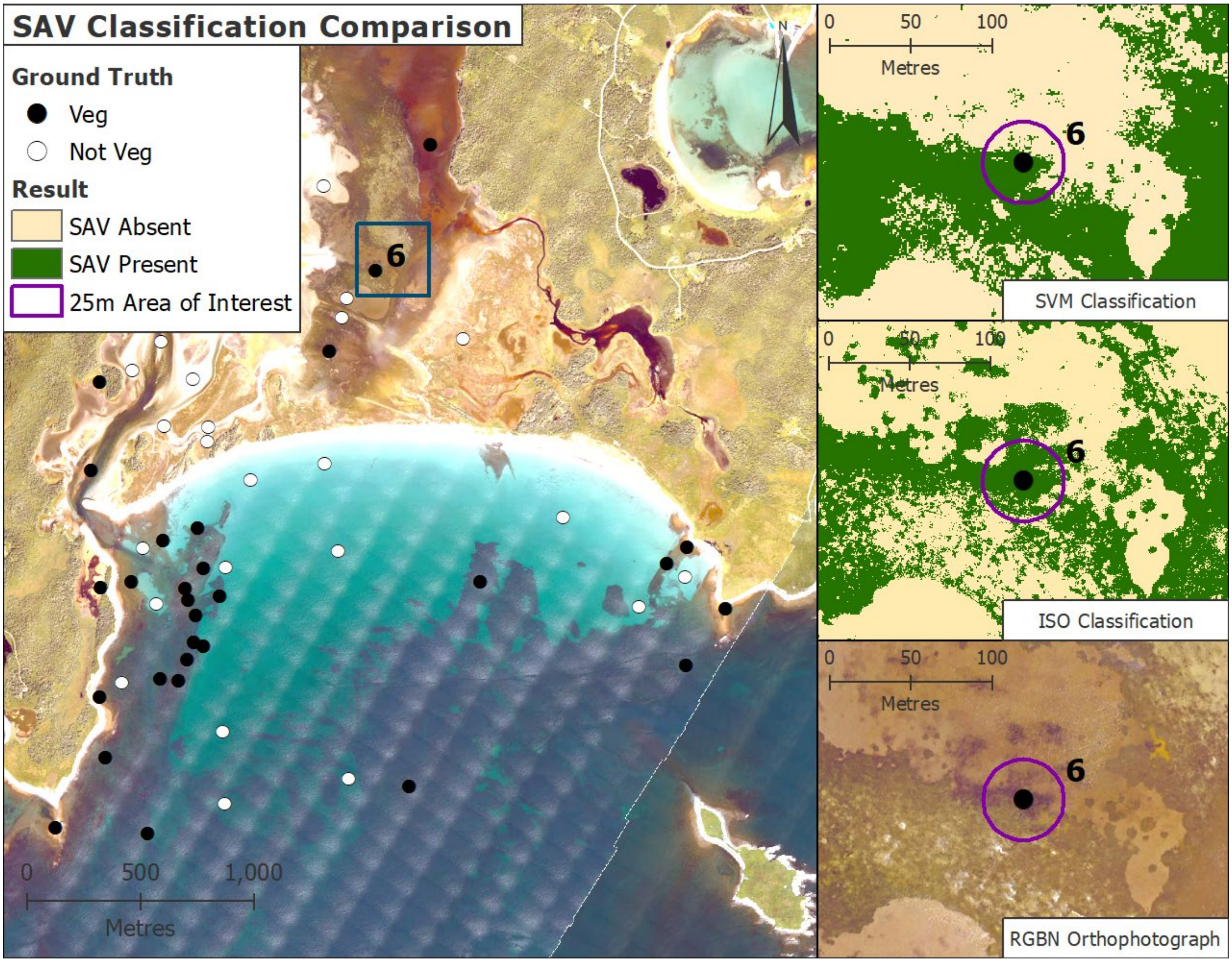

Figure 3.19 Shown is a more detailed view of the Matthews Lake area, validation point 6. Results between the two classifiers vary in highly detailed shallow areas such as the marsh. The Buffer indicates a 25m radius used for validating spatially.

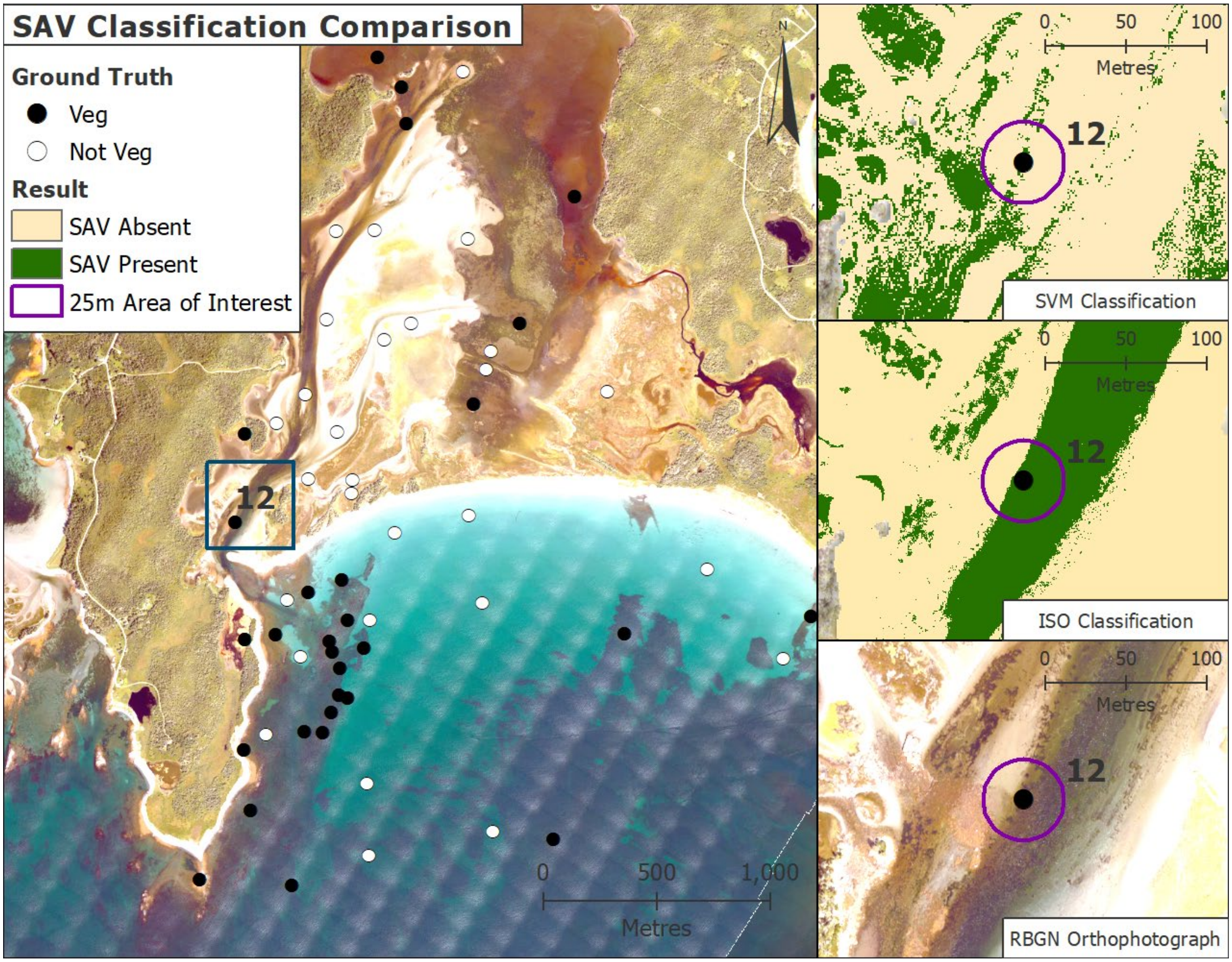

Figure 3.20: More Detailed view of SAV classifications. The ISO classification tended to produce SAV false positives in deeper-darker waters such as the channel feeding into the Mathews Lake marsh while the SVM classifier missed some deep vegetation visible in the same areas. The Buffer indicates a 25m radius used for validating spatially.

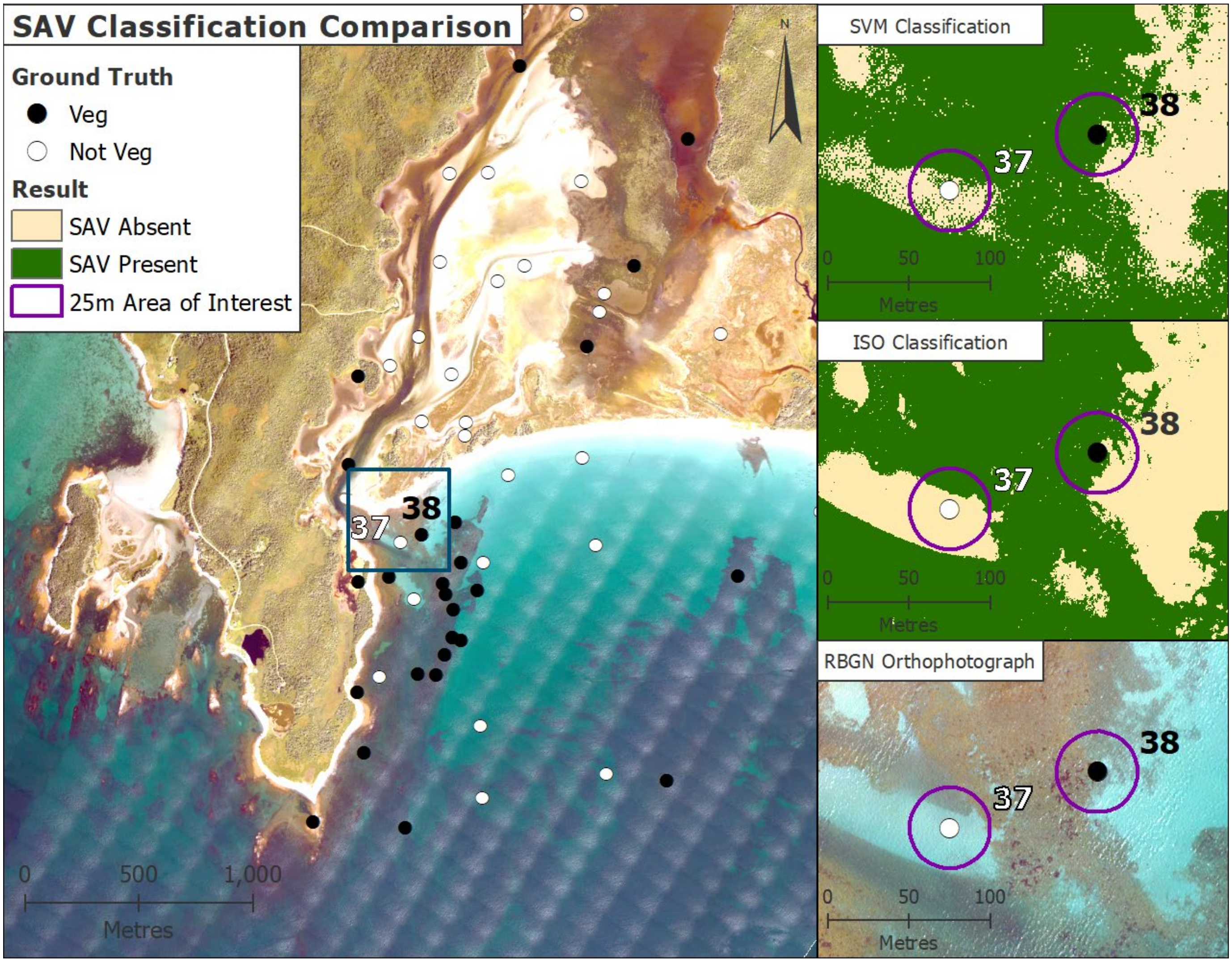

Figure 3.21: More detailed view of SAV classifications. Both Classifications performed similarly well in the outer bay where contrast between sand and SAV was generally higher. The Buffer indicates a 25m radius used for validating spatially.

Analysis both ISO and SVM clustering methods were explicitly compared to the underwater ground truth data. A focal statistics of each output classified raster was generated at a 25 metre circular radius counting cells of SAV for each ground truth point (Figure 3.22). The buffer distance used in this calculation can be seen in (Figure 3.21, Figure 3.22, Figure 3.23). This was done to incorporate a spatial component to the accuracy assessment whereby patches of complete SAV should indicate strongly in terms of the ground control and conversely those with low to zero SAV should be indicated as non-SAV. Points which range between the extrema indicate some confusion which may be based on the local spatial distribution of the real world SAV based on the model output. Figure 3.22 indicates that both classification methods validate well though the SVM method contained notably fewer extrema errors.

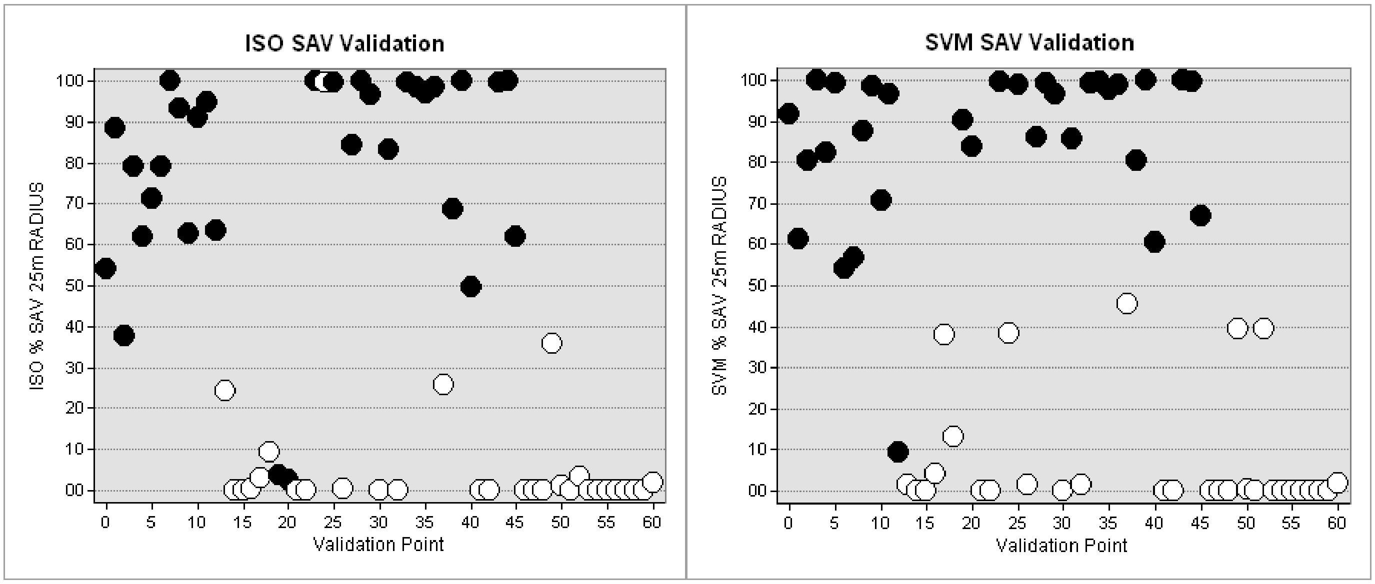

Figure 3.22: SVM classification performed slightly better than the ISO method when compared to expected ground truth data for SAV presence absence. Shown are a count of SAV pixels per validation point in a 25 metre radius. Separation of dark (SAV) and light (non-SAV) validation points indicates good classification at a 25m resolution.

When each classification is sampled at the exacting location of the ground truth points (totaling 61), the SVM performed with an overall agreement of SAV/non-SAV at 97%, while the ISO was 90% (Figure 3.22, Figure 3.23).

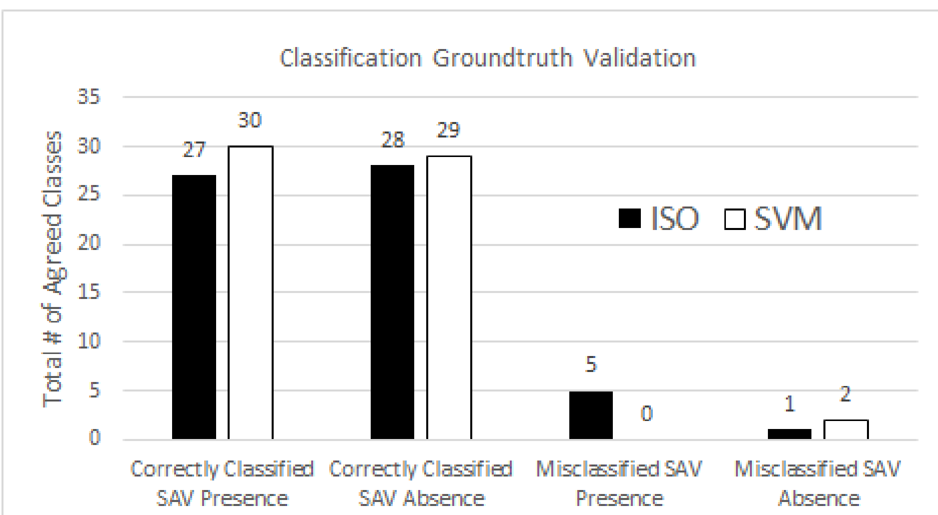

ISO
Overall Agreement=0.90%
Agreement by Chance= 0.50%
Cohen's Kappa Statistic= 0.80

SVM
Overall Agreement=0.97%
Agreement by Chance= 0.50%
Cohen's Kappa Statistic= 0.93

Figure 3.23: SVM vs ISO Classification results both indicate very high performance in terms of the available ground truth data.

Of the 23 collected Ground truth points only 17 included photos (Table 3.4 and Table 3.5). Of these photos 6 were classified as non-vegetation and only three of six had photos. Due to the limiting number of validation points (3 non-vegetation and 16 vegetation) additional ground truth points were created using the RCD30 ortho image to create a total of 61 points (31 Non-Vegetation and 30 Vegetation) (Table 3.6 and Table 3.7).

ISO Class	Number of quadrats identified as each ground type	Agreement of class with AGRG quadrat imagery	Agreement of class with AGRG quadrat imagery (%)
Vegetation	13	12	92.30
Not Vegetation	3	2	66.6

Table 3.4: Submerged Aquatic Vegetation classification validation. Quadrat images with vegetation present were included in the final classification validation, totaling 23 points.

SVM Class	Number of quadrats identified as each ground type	Agreement of class with AGRG quadrat imagery	Agreement of class with AGRG quadrat imagery (%)
Vegetation	13	12	92.30
Not Vegetation	3	3	100

Table 3.5: Submerged Aquatic Vegetation classification validation. Quadrat images with vegetation present were included in the final classification validation, totaling 23 points.

ISO Class	Number of quadrats identified as each ground type	Agreement of class with AGRG quadrat imagery	Agreement of class with AGRG quadrat imagery (%)
Vegetation	28	27	96.42
Not Vegetation	33	28	84.8

Table 3.6: Submerged Aquatic Vegetation classification validation Iso-clustering classification. Quadrat images with vegetation present were included in the final classification validation, totaling 61 points.

SVM **Class**	Number of quadrats identified as each ground type	Agreement of class with AGRG quadrat imagery	Agreement of class with AGRG quadrat imagery (%)
Vegetation	30	30	100
Not Vegetation	31	29	93.5

Table 3.7: Submerged Aquatic Vegetation classification validation for SVM classification. Quadrat images with vegetation present were included in the final classification validation, totaling 61 points.

Of the two images the SVM classification had 37.47% vegetation (5846450 sq. meters) and 62.52% non-vegetation (9753854 sq. meters). The ISO classification had 43.47% vegetation (3360769 sq. meters) and 56.52% non-vegetation (4368809 sq. meters).

3.3 Model Results

3.3.1 Validation with ADCP

Two month-long ADCP deployments and one two-day deployment occurred at Lockeport in 2017 (Table 2.2). The data from the deployments are presented in Appendix B Section 6.2. The depth averaged ADCP data were used to validate the model (Figure 3.24, Figure 3.25, Figure 3.26 and Table 3.8). Surface elevation for each validation was matched well in each simulation. At the Deep ADCP (Figure 3.24), EW currents (u-currents) were well-modelled in amplitude and phase. The NS currents (v-currents) were smaller in amplitude than the EW current, and the model simulated amplitude fairly well. At the Shallow ADCP (Figure 3.25) the model was less successful in simulating flow; EW flow was better modelled than NS flow. At the Channel ADCP the model again simulated EW currents better than NS, which lagged the observed shift from flood to ebb tide and under-predicted amplitude during the peak flood tide (Figure 3.26).

ADCP Location	Mean Current Speed (m/s)		Max Current Speed (m/s)		Mean Current Direction (˚)	
	Observed	**Modelled**	**Observed**	**Modelled**	**Observed**	**Modelled**
Deep	0.10	0.10	0.34	0.06	153	141
Shallow	0.03	0.01	0.08	0.11	148	160

Table 3.8: Modelled and observed mean and max current speeds and directions.

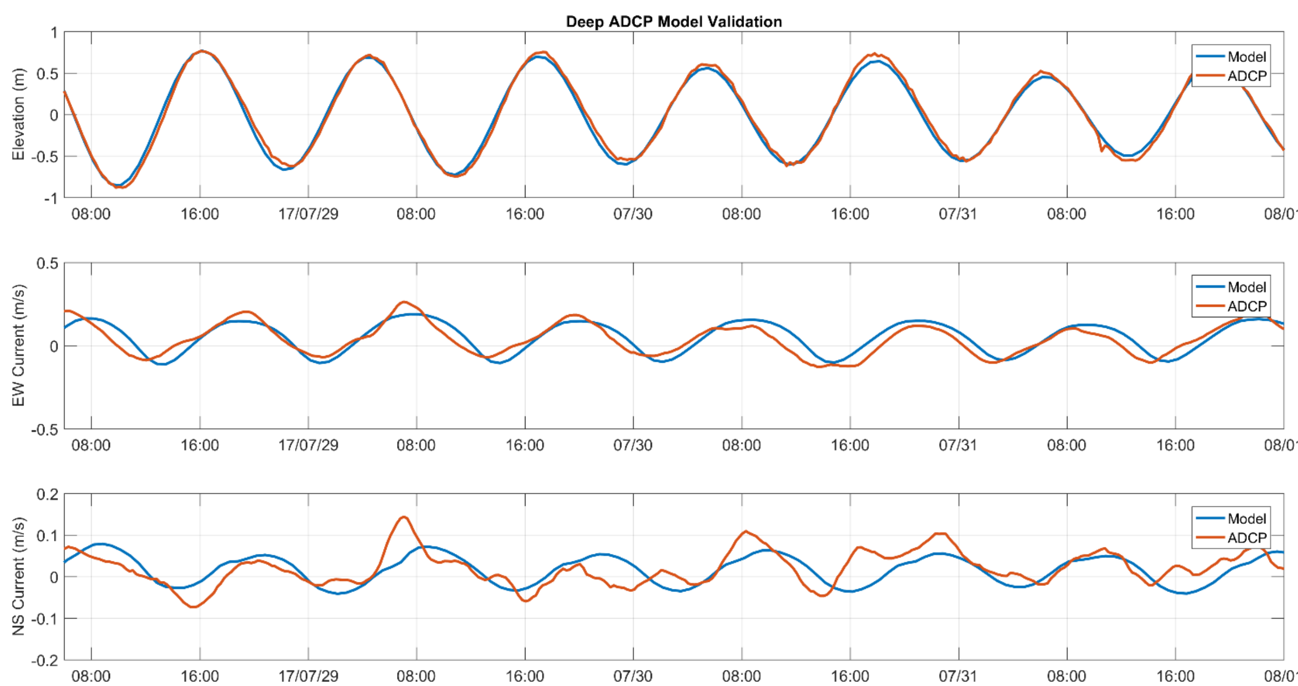

Figure 3.24: Deep ADCP model validation.

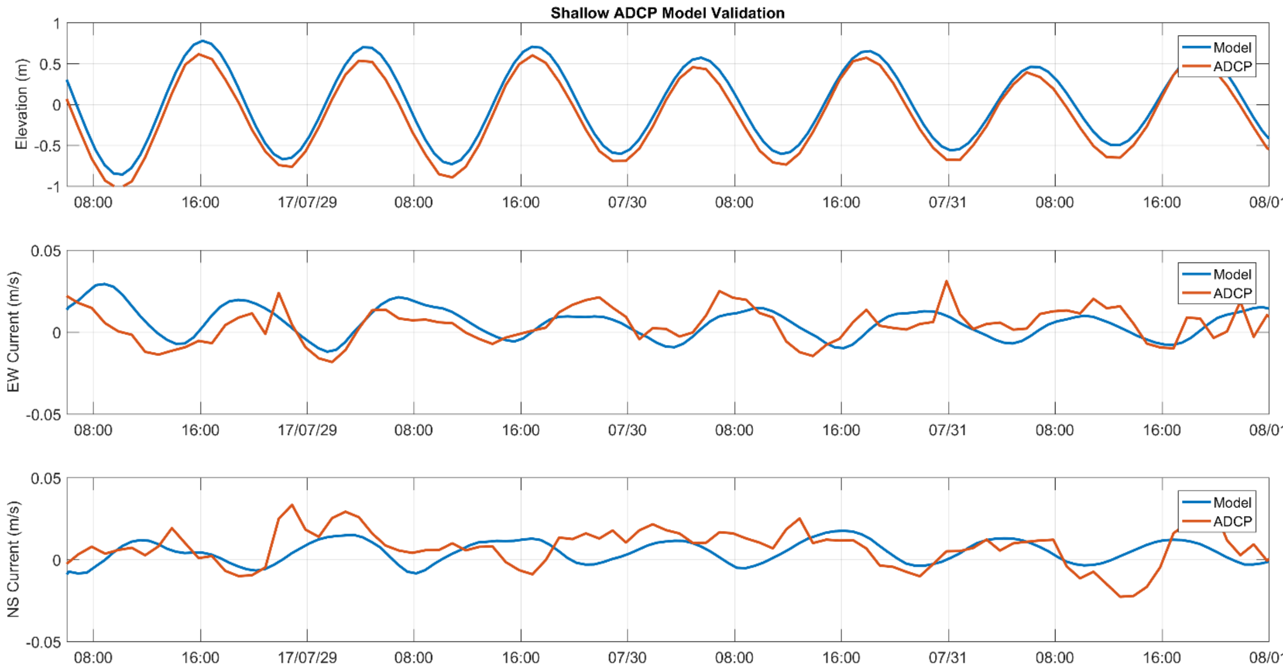

Figure 3.25: Shallow ADCP model validation.

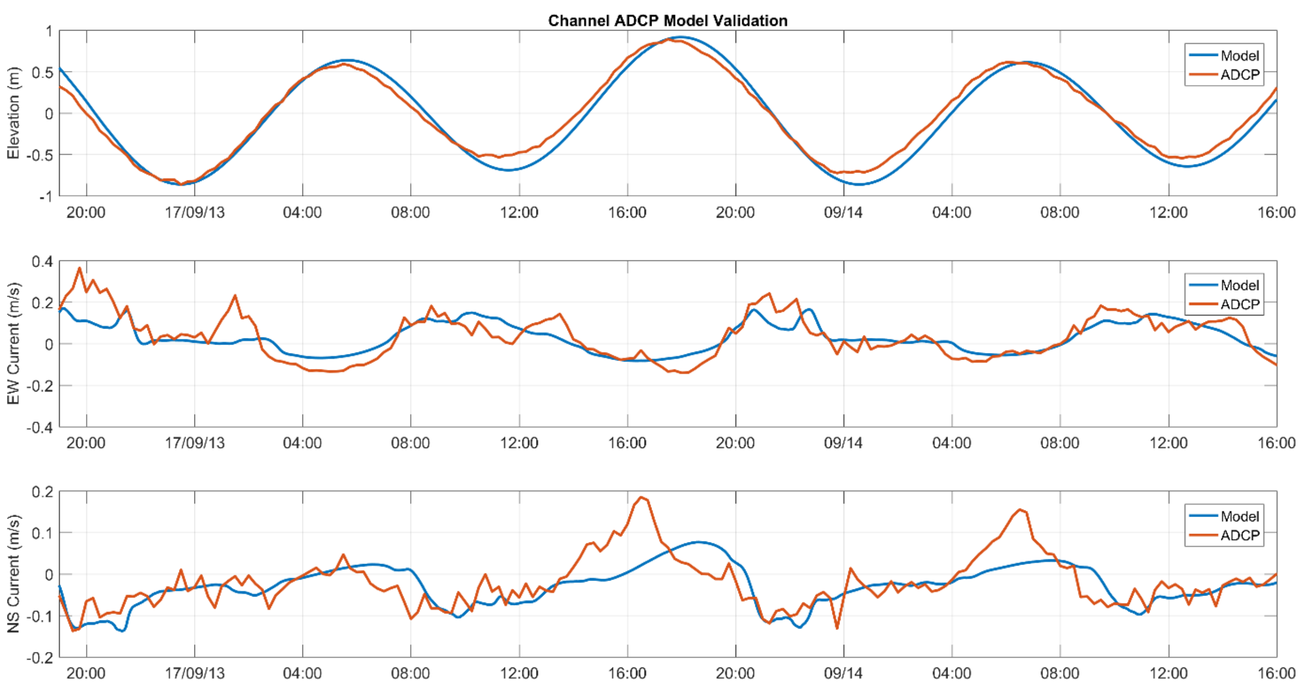

Figure 3.26: Channel ADCP model validation.

3.3.2 Validation with RiverRay ADCP

The modelled velocity and discharge appear to lag the observations by approximately 0.5 hour, which agrees with the ADCP results above (Table 3.9, Figure 3.27).The bathymetry observed at the channel by the RiverRay was represented well by the model (Figure 3.28).

RiverRay Transect	Observed Velocity (m/s)	Modelled Velocity (m/s)	Modelled Direction (˚)	Observed Discharge (m^3/s)	Modelled Discharge (m^3/s)
15:05	-0.03	0.17	121	-2.57	10.5
15:15	-0.14	0.14	121	-14.2	8.3
15:22	-0.2	0.08	120	-21.2	5.1
15:36	-0.35	0.11	308	-38.1	7.9
15:42	-0.43	0.16	310	-48.6	12.4
15:47	-0.5	0.20	311	-55.8	15.8
15:52	-0.51	0.24	311	-57.3	18.6
16:21	-0.64	0.41	314	-81.4	38.3
16:25	-0.68	0.44	313	-86.5	41.0
16:30	-0.72	0.47	313	-78.2	44.2
16:35	-0.79	0.49	313	-102	47.5
16:58	-0.89	0.61	312	-119	68.0
17:02	-0.84	0.63	312	-115	70.5
17:05	-0.91	0.64	312	-125	72.4
17:08	-0.95	0.65	312	-131	74.2
18:11	-1.15	0.82	311	-174	107.0
18:14	-1.08	0.82	311	-163	107.5
18:20	-1.10	0.83	312	-176	109.4
18:24	-1.14	0.84	312	-172	110.7

Table 3.9: River Ray transect summaries on September 14, 2017. The negative sign in the observations indicates that flow was moving into the inlet (NW) on all of the observed transects. The modelled velocity and discharge appear to lag the observations by approximately 0.5 hour.

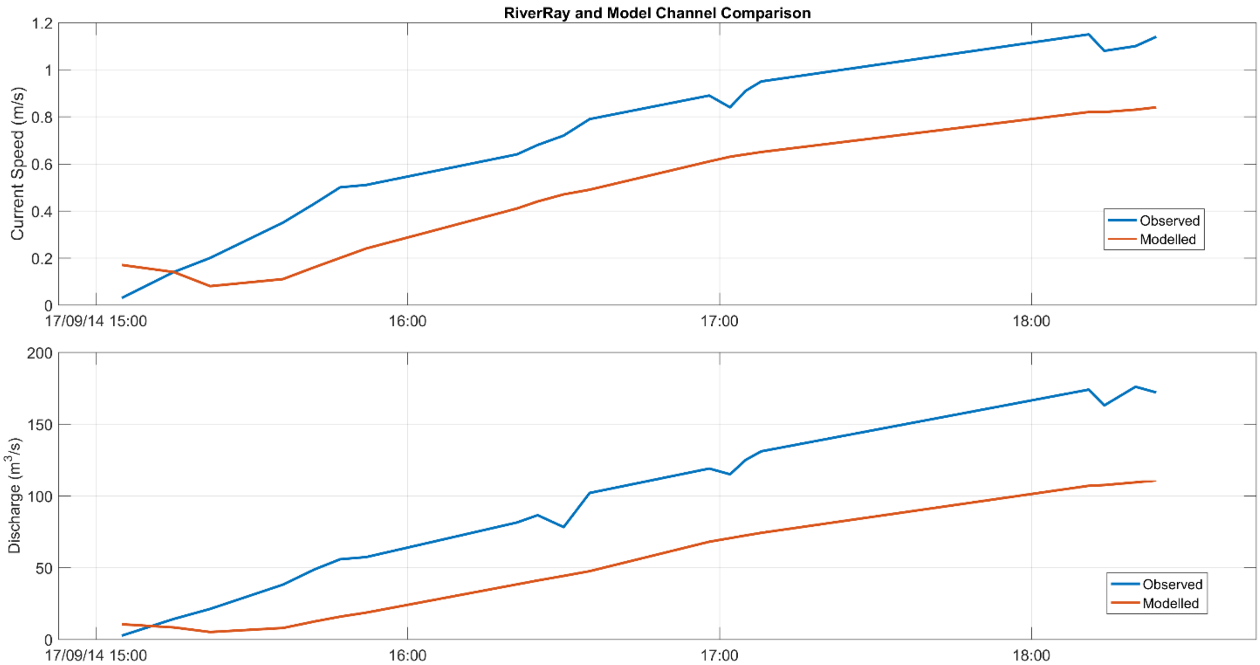

Figure 3.27: RiverRay and modelled current speed (top) and discharge (bottom).

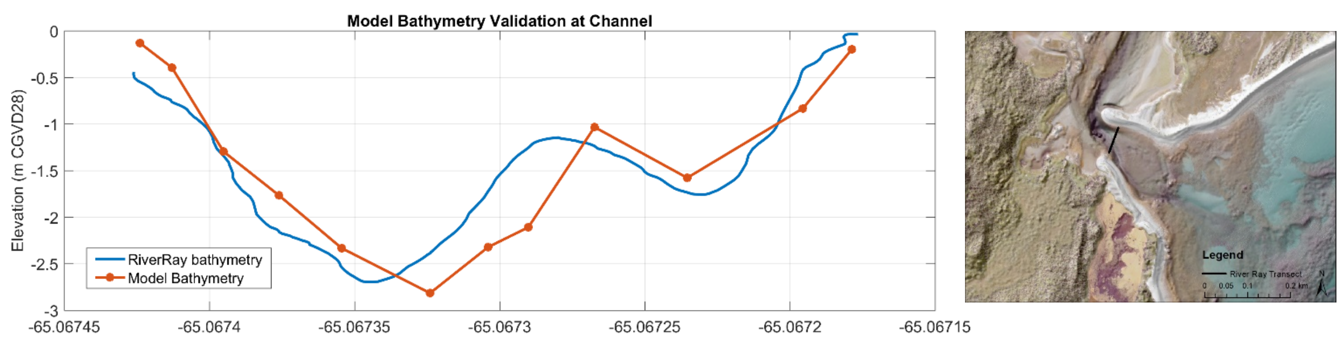

Figure 3.28: Validation of model bathymetry at the channel compared to river ray bottom track.

3.3.3 Validation with Drogues

The particle tracking module was employed to model the release of seven drogues in the area of the tidal inlet (Table 3.10). Particles were parameterized to act as conservative particles with no decay, erosion, or dispersion; mass flux and number of particles were set to 1. Drogue experiments were chosen to represent drogues released at several distances away from the inlet, whose tracks varied. The experiments in the field revealed a strong tendency for drogues to float away from the tidal inlet, and for drogues on the north side of the shoal to behave differently from those on the south side of the shoal. The simulations suitably represented that tendency (Figure 3.29).

Drogue	Start Time	Easting (m)	Northing (m)
1	9/14/2017 17:57	333597	4840233
2	9/14/2017 17:55	333697	4840016
3	9/14/2017 17:56	333662	4840078
4	9/14/2017 17:53	333759	4839863
5	9/14/2017 13:29	333863	4839665
6	9/14/2017 13:39	334516	4839778
7	9/14/2017 13:41	334558	4839377

Table 3.10: summary of drogues used for validation.

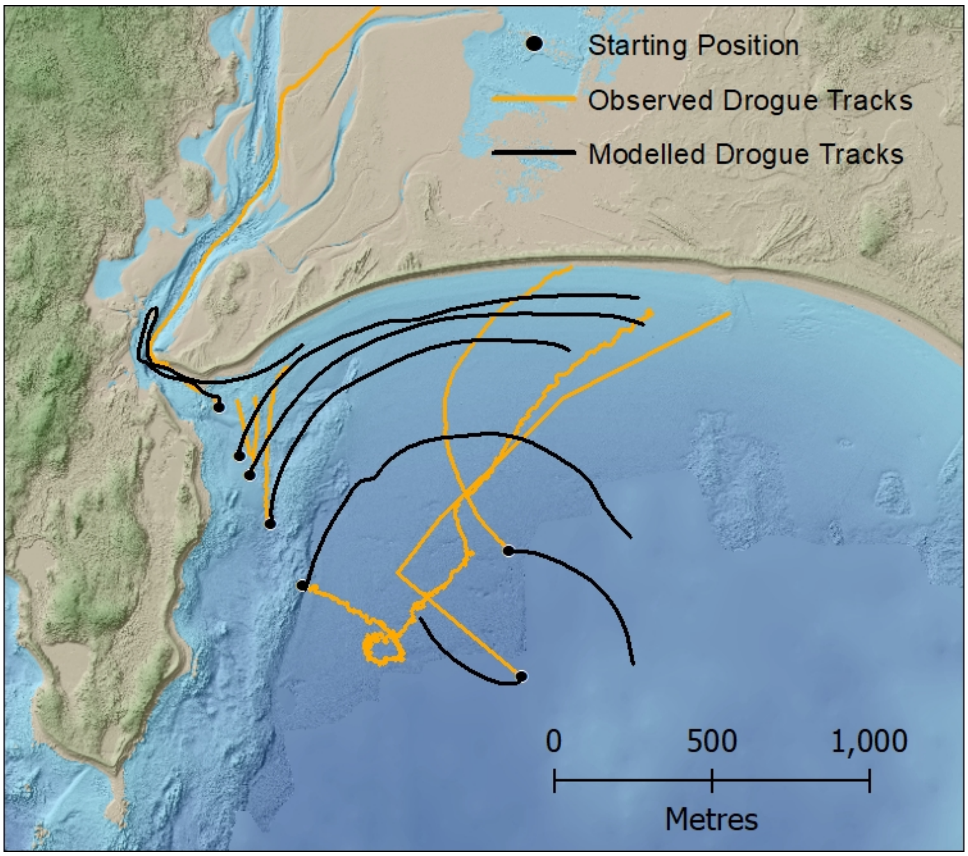

Figure 3.29: Drogue simulation results.

3.3.4 Current Characterization

Figure 3.30 and Figure 3.31 show the maximum and mean monthly currents generated during the one-month model simulation. The maximum monthly currents show the strong current speed in the tidal inlet, > 0.3 m/s. The figures below show the shaded bathymetry with the current speeds overtop. West of the inlet there is a rock shelf creating a shoal that appears to impede the current speed of water entering and exiting the tidal inlet where maximum speeds are reduced from > 0.3 m/s to > 0.1 m/s.

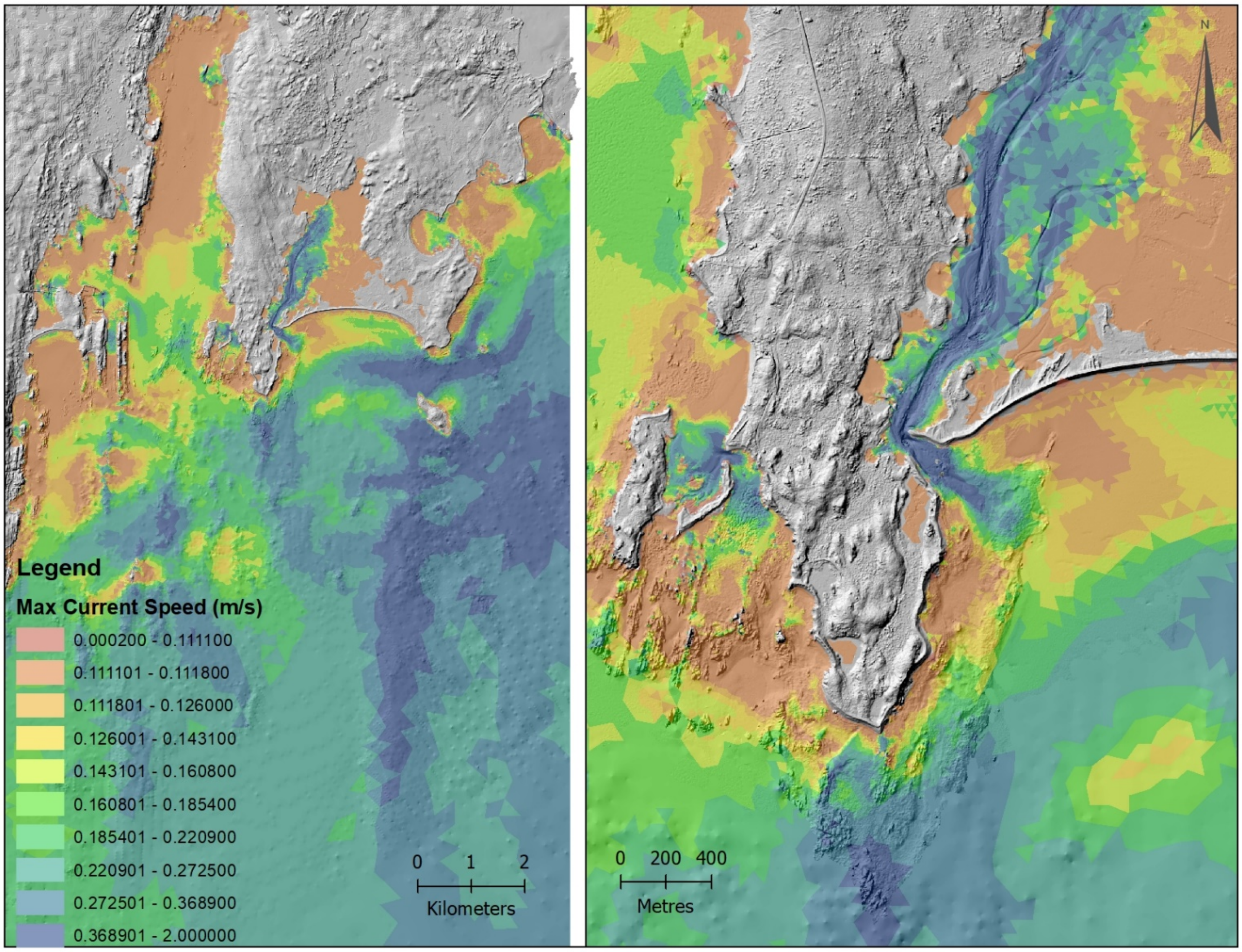

Figure 3.30: Maximum modelled monthly currents. Left map is for a small scale overview. The right map is a zoom in on the tidal inlet.

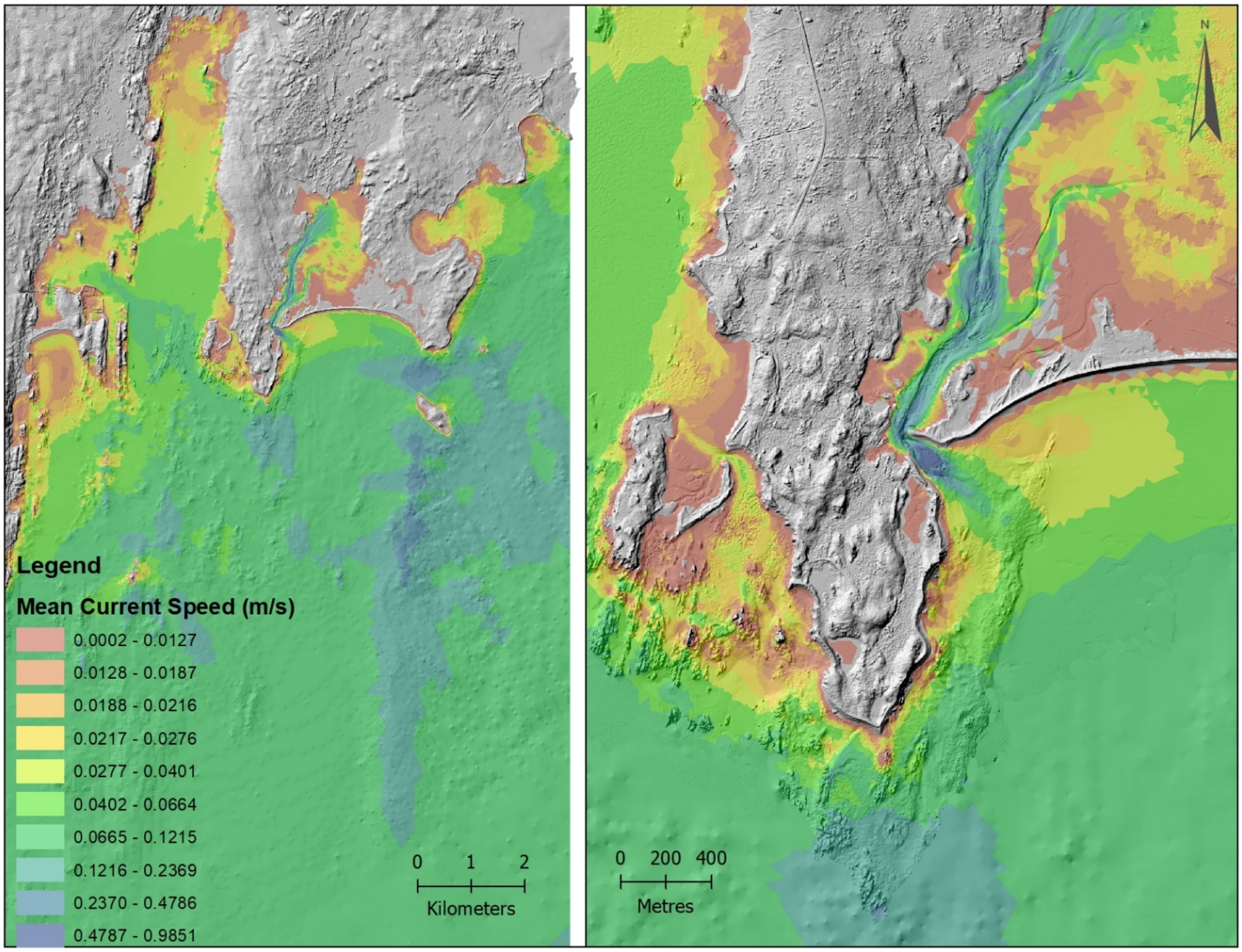

Figure 3.31: Mean modelled monthly currents. Left map is for a small scale overview. The right map is a zoom in on the tidal inlet.

3.3.5 Spill Simulations Results

The contaminant spill simulations were executed under different wind conditions as described in the Shell Environmental Impact Assessment for drilling offshore southwest Nova Scotia (Table 3.11). The results of the contaminant spill simulations show an interesting circulation pattern with the bay seaward of the tidal inlet. The following figures show the maximum concentration per element from the whole simulation (Figure 3.32-Figure 3.36). Note that none of the offshore point sources ever came near the shore at all. The only one where particles went in the inlet was scenario 5 (Figure 3.36).

Scenario	Wind Description	Speed (m/s)	Direction (˚)
1	Strong winter wind	10	NW (315)
2	Moderate summer wind	5	SW (225)
3	Winter storm 1	25	E (100)
4	Winter Storm 2	25	S (180)
5	Winter Storm with particle release at mid-tide rising	25	S (180)

Table 3.11 Wind speeds associated with the different particle tracking simulation scenarios.

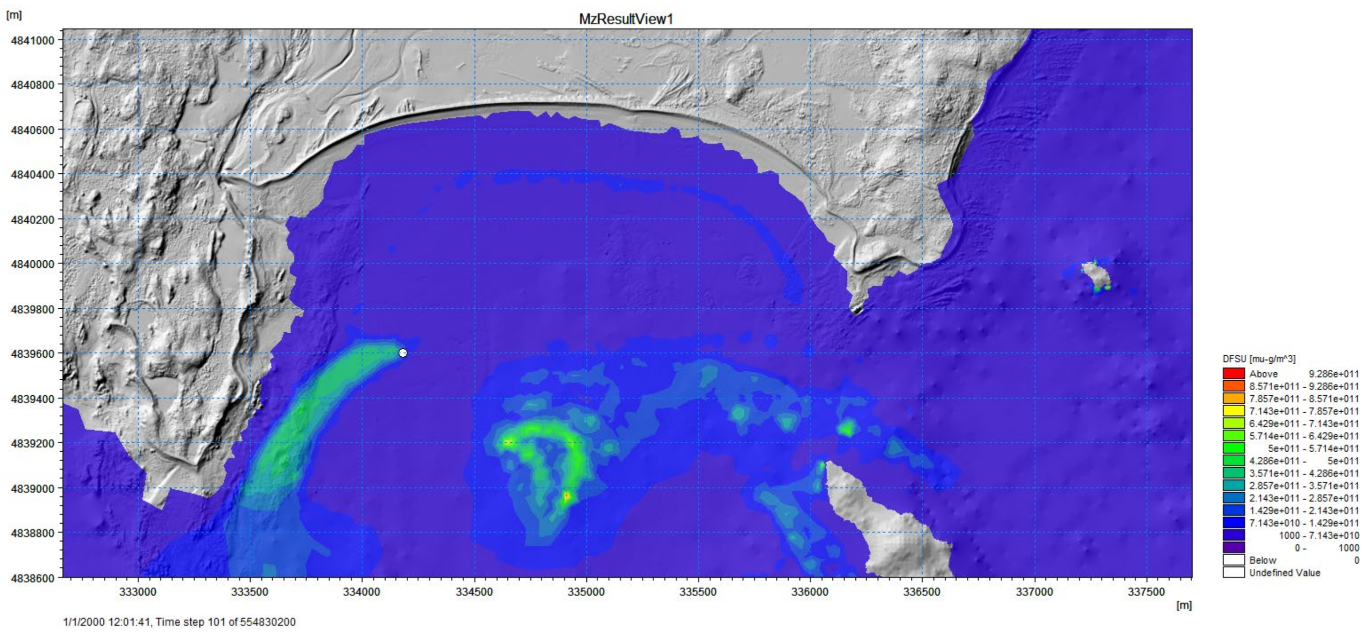

Figure 3.32: Heavy suspended winter maximum concentration (Scenario 1). The white circle represents the source of the spill.

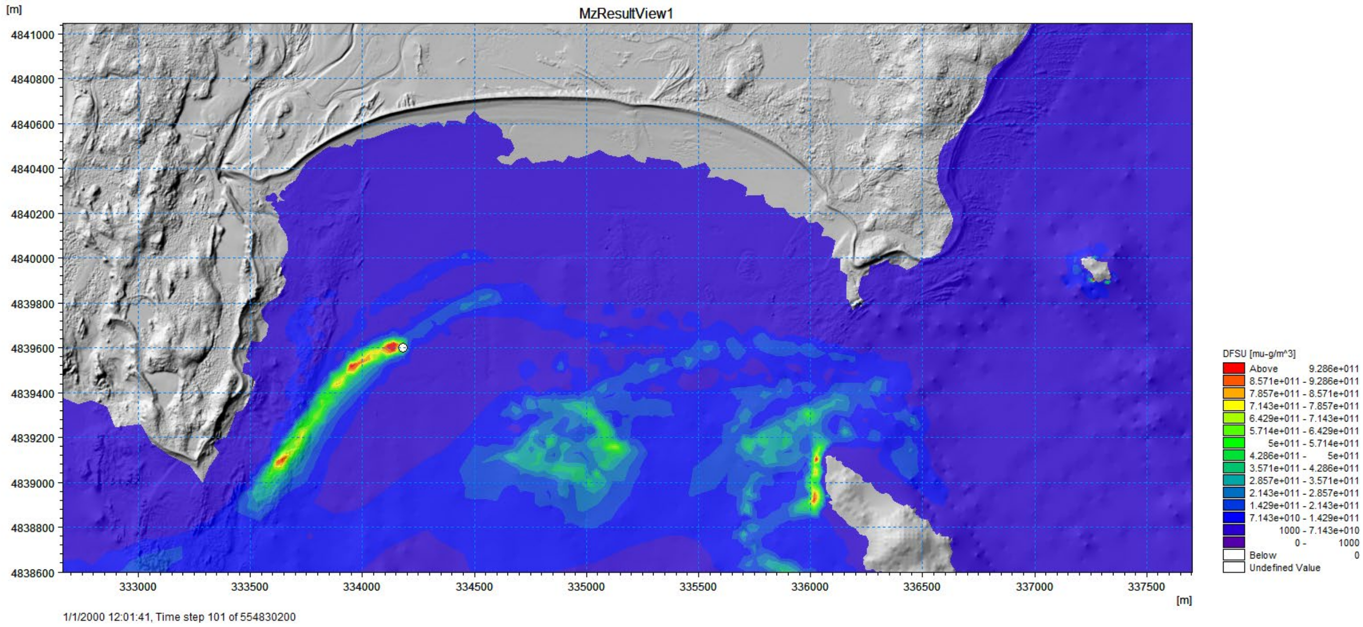

Figure 3.33: Heavy suspended summer maximum concentration (Scenario 2). The white circle represents the source of the spill.

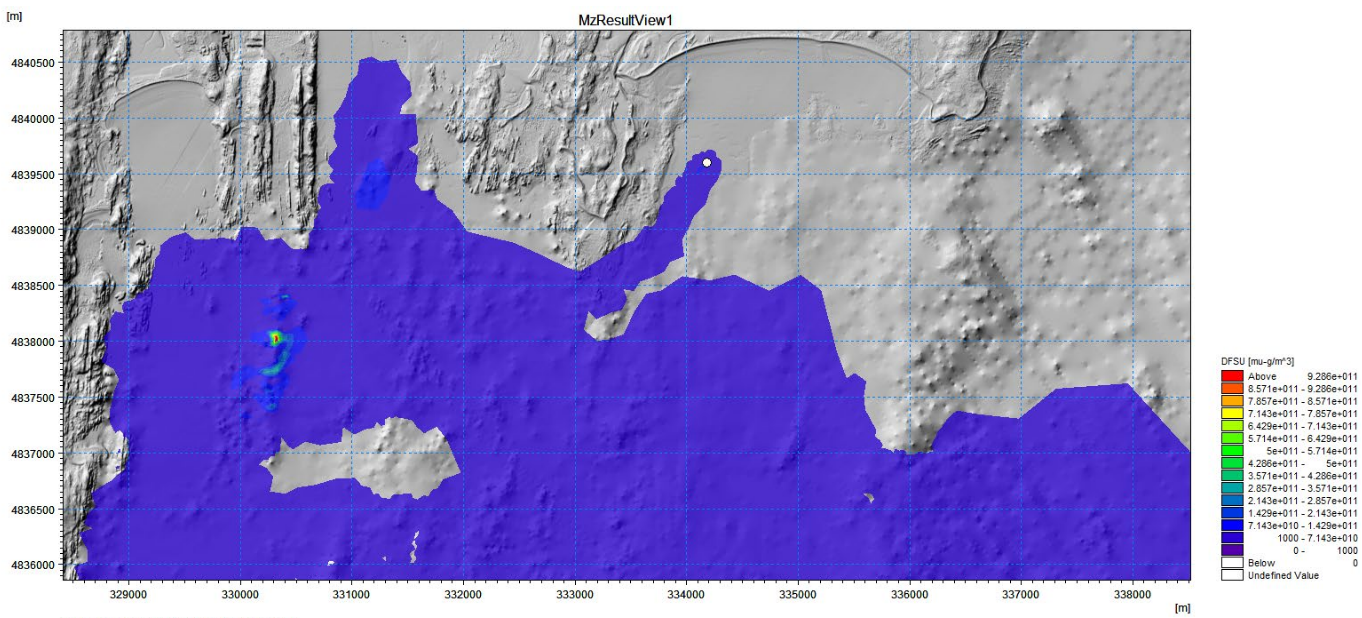

Figure 3.34: Heavy suspended maximum concentration during a winter storm with easterly wind (Scenario 3). The white circle represents the source of the spill. Note the extent and scale of this map is different from the previous two figures because of the way the particles have been distributed.

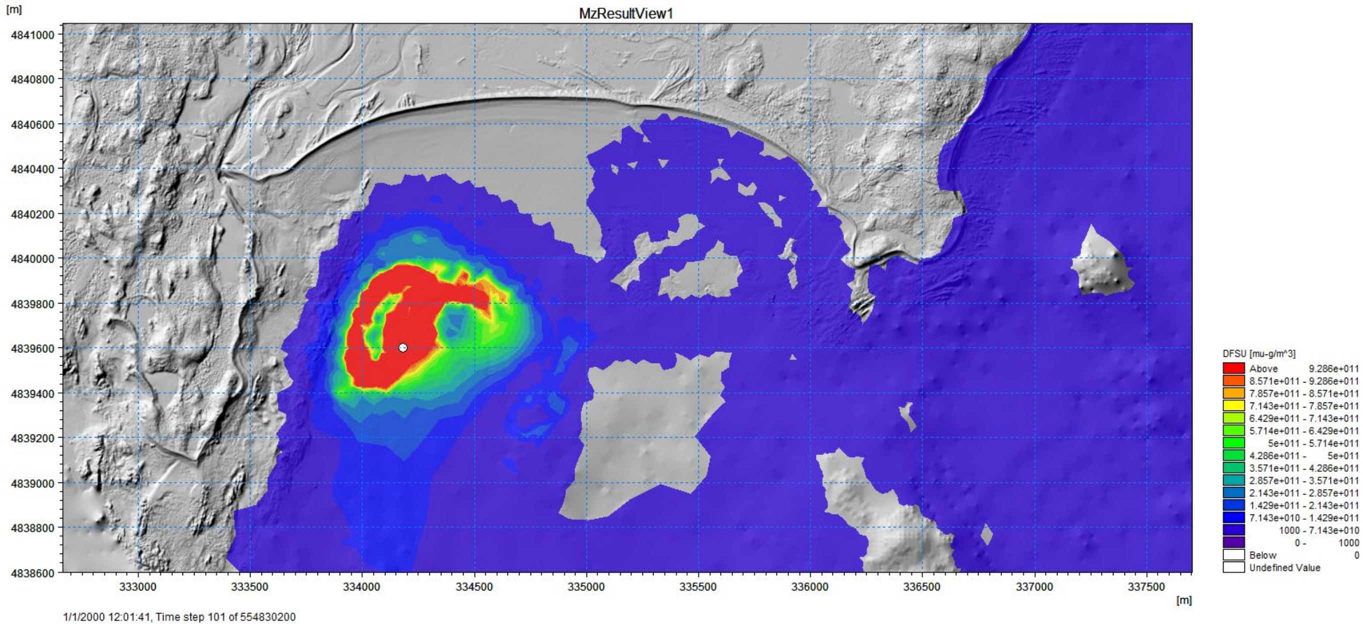

Figure 3.35: Heavy suspended maximum concentration during a winter storm with southerly wind (Scenario 4). The white circle represents the source of the spill. The extent and scale are the same of Figures 3.32-3.33.

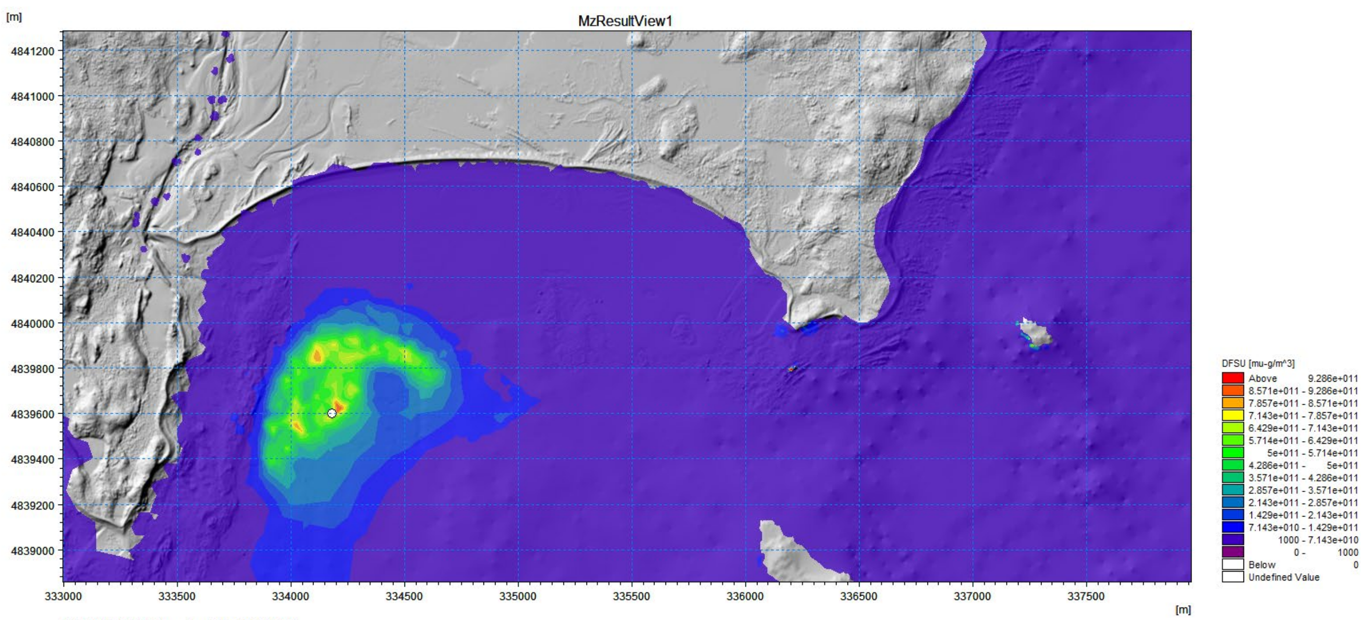

Figure 3.36: Heavy suspended maximum concentration during a winter storm with southerly wind with particles released at mid-tide rising (Scenario 5). The white circle represents the source of the spill. Note the purple-blue particles within the inlet channel.

4 Conclusions

This report has documented the innovative uses of data derived from a single topo-bathymetric lidar survey. The collection of high-resolution seamless elevation data from land into the near shore bathymetry and aerial photographs provides the foundation for a suit of analytical techniques to support contaminant spill preparedness.

The lidar sensor reached a depth of 13 m indicating the water conditions were clear and very suitable for this technology. The aerial photographs were processed and orthophoto mosaics produced. Two maps were produced that demonstrate the enhanced capabilities of this approach as compared to the standard video data collection and manual interpretation of shoreline attributes conducted by Environment Canada. The original elevation products and orthophotos were processed in different ways to produce derivative products that were used as the input into the classification algorithms. Several analysis methods were explored to derive the thematic information from the orthophotos. The supervised maximum likelihood classification was presented here for the derivation of the shoreline substrate maps. For the benthic habitat and specifically the submerged aquatic vegetation (SAV) maps two methods were presented and compared; the Support Vector Machine (SVM) approach and the unsupervised ISO clustering method. Through comparison with ground truth and visual assessment, the SVM classification method outperformed the ISO classification method.

These lidar bathymetric data were merged with lower-resolution chart soundings to construct a variable resolution mesh that was used in the hydrodynamic modelling phase of the project. Two ADCPs were deployed at different water depths and used to validate the model results. Special interest was paid to the interaction between the open ocean and the tidal inlet. Field experiments were conducted using drifter buoys on two different occasions to compare to the model results and better understand the interactions of the current velocities associated with the tidal inlet. An ADCP was deployed near the mouth of the inlet for a short duration and a RiverRay ACDP was used to measure the cross-section and current speeds at the mouth of the inlet over the tidal cycle. These various in-situ current measurements were used to validate the HD model. Once satisfied with the validation of the model various simulations were executed and particles representing contaminants were released seaward of the inlet. Different atmospheric forcing parameters were used in the simulation scenarios to represent typical wind patterns that occur in southwest Nova Scotia. For all simulations but one, no particles entered the inlet. The only simulation where particles entered the inlet occurred during a winter storm associated with a southerly wind. These results are consistent with our field observations related to our drifter experiments. Drifters buoys were deployed seaward of the tidal inlet mouth and tracked over the tidal cycle or until they made it to shore or entered the inlet. In most cases the drifters trajectory showed them deflected in a clockwise rotation past the tidal inlet and not entering it. A second set of drifter experiments were conducted where they were placed in a line moving seaward of the mouth of the inlet. In this case one drifter did enter the inlet channel and make it's way into the salt marsh. Upon inspection of the nearshore bathymetry and by analyzing the tidal currents and other model outputs we interpret this behavior to be a result of a shoal that exists seaward of the tidal inlet that deflects much of the current way from the mouth of the inlet and thus protects it from particles that originate seaward.

We have concluded from this study that this approach provides a rich set of information products that can be utilized by a variety of coastal management stakeholders. The objective of this project was to demonstrate how this technology and approach can provide enhanced information to groups such as ECRC who are responsible for clean up in the event of a contaminant spill. We believe this approach should be carried out throughout our entire coastal area or at the very least in areas of tidal inlets and sensitive habitats such as salt marshes.

5 Appendix A

5.1.1 Lidar processing

5.1.1.1 Point Cloud Processing

Once the GPS trajectory was processed for the aircraft using the Nova Scotia Active Control Stations (NSACS) network as a base station, where the aircraft GPS observations were combined with the inertial measurement unit to determine the trajectory in Inertial Explorer. Once determined the navigation data was linked to the laser returns and they were georeferenced. Lidar Survey Studio (LSS) software accompanies the Chiroptera II sensor and was used to process the lidar waveforms into discrete points. These data were then inspected to ensure sufficient overlap between flight lines (30%) and that no gaps existed in the lidar coverage.

Integral to the processing of bathymetric lidar is the ability to map the water surface. The defined water surface is critical for two components of georeferencing the final target or targets that the reflected laser pulse recorded: the refraction of the light when it passes from the medium of air to water and the change in the speed of light from air to water. The LSS software computes the water surface from the lidar returns of both the topo (NIR) and bathy (green) lasers. In addition to classifying points as land, water surface or bathymetry, the system also computes a water surface that ensures the entire area of water surface is covered regardless of the original lidar point density. As previously mentioned, part of the processing involves converting the raw waveform lidar return time series into discrete classified points using LSS signal processing. Waveform processing may include algorithms specific to classifying the seabed. The points were examined in LSS both in planimetric and cross-section views. The waveforms for each point can be queried so that the location of the waveform peak can be identified and the type of point defined, for example water surface and bathymetry.

The LAS files, the file type output from LSS, were then read into TerraScan™ with the laser returns grouped by laser type so they could be easily separated, analyzed and further refined. Because of the differences in the lidar footprint between the topo and bathy lasers, the bathy points are derived from the bathy green laser and the topo points that represent targets on the land were derived from the topo NIR laser. See Table 5.1 and the attached

Data Dictionary report for the classification codes for the delivered LAS 1.2 files. The refined classified LAS files were read into ArcGIS™ and a variety of raster surfaces at a 1 m spatial resolution were produced.

Class number	Description
0	Water model
1	Bathymetry (Bathy)
2	Bathy Vegetation
3	N/A
4	Topo laser Ground
5	Topo laser non-ground (vegetation & buildings)
6	Hydro laser Ground
7	Bathy laser non-ground
8	Water
9	Noise
10	Overlap Water Model
11	Overlap Bathy
12	Overlap Bathy Veg
13	N/A
14	Overlap Topo Laser Ground
15	Overlap Topo Laser Veg
16	Overlap Bathy Laser Ground
17	Overlap Bathy Laser Veg
18	Overlap Water
19	Overlap Noise

Table 5.1. Lidar point classification Codes and descriptions. Note that 'overlap' is determined for points which are within a desired footprint of points from a separate flight line.

5.1.1.2 Gridded Surface Models

There were three main data products derived from the lidar point cloud. The first two were based on the elevation and include the Digital Surface Model (DSM), which incorporates valid lidar returns from vegetation, buildings, ground and bathymetry returns, and the Digital Elevation Model (DEM) which incorporates ground returns above and below the water line. The third data product was the intensity of the lidar returns, or the reflectance of the bathy laser. The lidar reflectance, or the amplitude of the returning signal from the bathy laser, is influenced by several factors including water depth, the local angle of incidence with the target, the natural reflectivity of the target material, the transmission power of the laser and the sensitivity of the receiver.

5.1.1.3 Depth Normalization of the Green Laser Amplitude

The energy that is transmitted into the water column by the green laser is exponentially lost with depth. The amplitude of the returning signal from the bathy laser provides a means of visualizing the seabed cover. However, the raw amplitude data are difficult to interpret because of variances as a result of signal loss due to the attenuation of the laser pulse through the water column at different scan angles and depths. Gridding the amplitude value from the bathy laser results in an image with a wide range of values that are not compensated for depth and have significant differences for the same target depending on depth and the local angle of incidence from flight line to flight line. As a result, these data are not suitable for quantitative analysis and are difficult to interpret for qualitative analysis. A process has been developed to normalize the amplitude data for signal loss and is reported in a recent publication (Webster et al., 2016). The process involved sampling the amplitude data from a location with homogeneous seabed cover (e.g., sand or eelgrass) over a range of depths. These data were used to establish a relationship between depth and the amplitude value. The inverse of this relationship was used with the depth map to adjust the amplitude data so that they could be interpreted without the bias of depth. This map is referred to as a depth normalized intensity (DNI) image, is more consistent in tone, and can be interpreted for the seabed cover material. Note that this analysis considers only bathymetric lidar values and ignores any topographic lidar returns.

5.1.1.4 Aerial Photo Processing

The RCD30 60 MPIX imagery were processed using the aircraft trajectory and direct georeferencing. The low altitude and high resolution of the imagery required that the lidar data be processed first to produce bare-earth digital elevation models (DEMs) that was used in the orthorectification process. The aircraft trajectory, which combines the GPS position and the IMU attitude information into a best estimate of the overall position and orientation of the aircraft during the survey is required for this process. This trajectory, which is linked to the laser shots and photo events by GPS based time tags, is used to define the Exterior Orientation (EO) for each of the RCD30 aerial photos acquired. The EO, which has traditionally been calculated by selecting ground control points (x, y, and z) locations relative to the air photo frame and calculating a bundle adjustment; however, in this case it was calculated using direct georeferencing and exploiting the high precision of the navigation system. The EO file defines the camera position (x, y, z) for every exposure as well as the various rotation angles about the x, y and z axis known as omega, phi and kappa. The EO file along with a DEM was used with the aerial photo to produce a digital orthophoto. After the lidar data were processed and classified into ground points, the lidar-derived DEM (above and below the water line) was used in the orthorectification process in Erdas Imagine software and satisfactory results were produced.

The 5 MPIX Quality Assurance (QA) camera were also processed and georeferenced in a similar fashion as with the RCD30 photos. Although the resolution of the orthophotos of the QA camera is less than the RCD30, 20 cm as compared to 5 cm, the QA photos provide excellent information over water for the water column and seabed.

5.1.2 Ellipsoidal to Orthometric Height Conversion

The original elevation of any lidar product are referenced to the same elevation model as the GPS they were collected with. This model is a theoretical Earth surface known as the ellipsoid, and elevations referenced to this surface are in ellipsoidal height (GRS80). To convert them to orthometric height (OHt), which is height orthogonal to the geoid we utilize a geoid-ellipsoid separation model. In this case the elevations were corrected to the Canadian Geodetic Vertical Datum of 1928 (CGVD28) based on the geoid-ellipsoid separation model, HT2, from Natural Resources Canada.

6 Appendix B

6.1 CTD

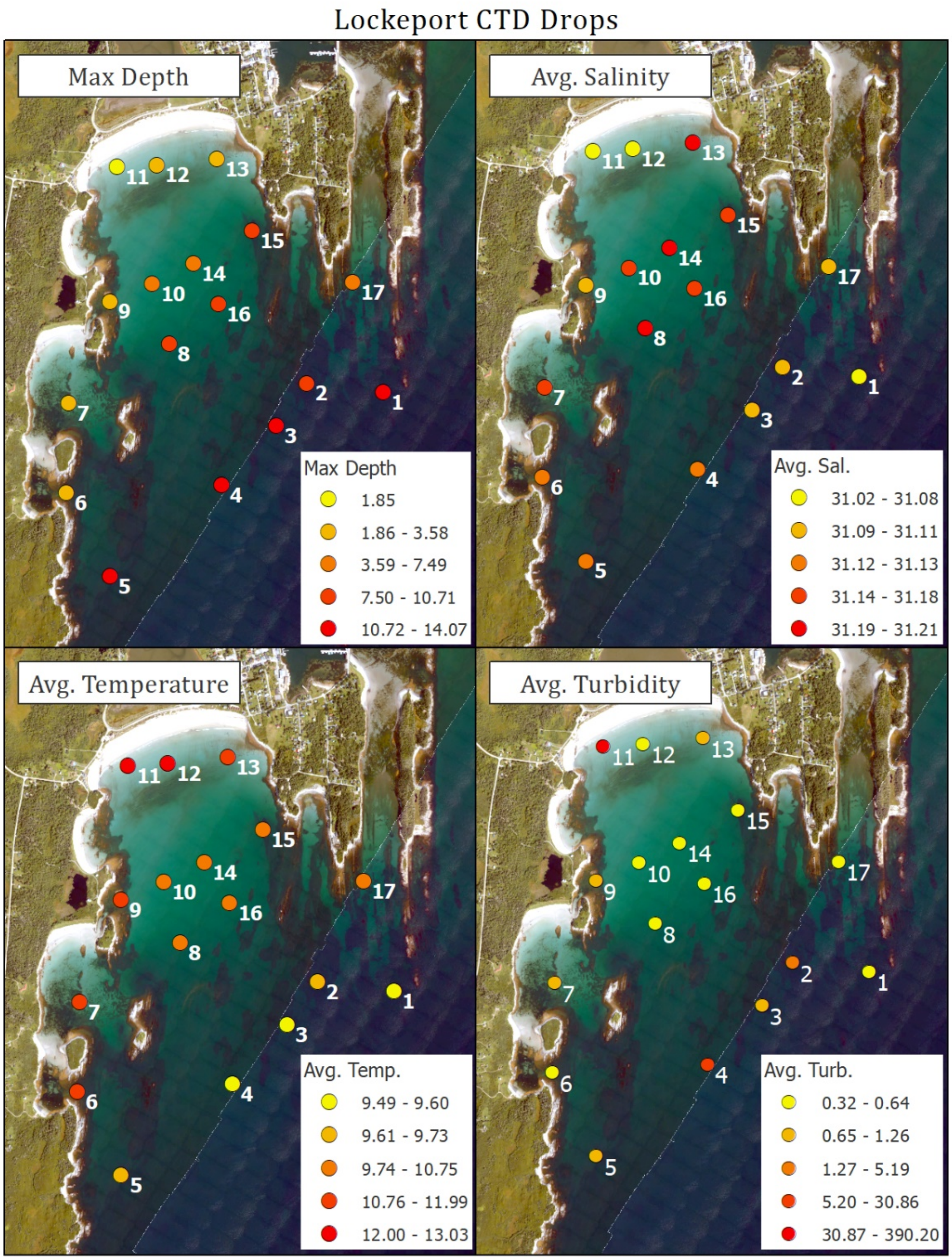

Figure 6.1: CTD data collected at Lockeport: maximum depth, and depth averaged salinity, temperature and turbidity. Salinity varied little throughout the inlet, while temperature decreased with increasing depth; turbidity did not exhibit a trend.

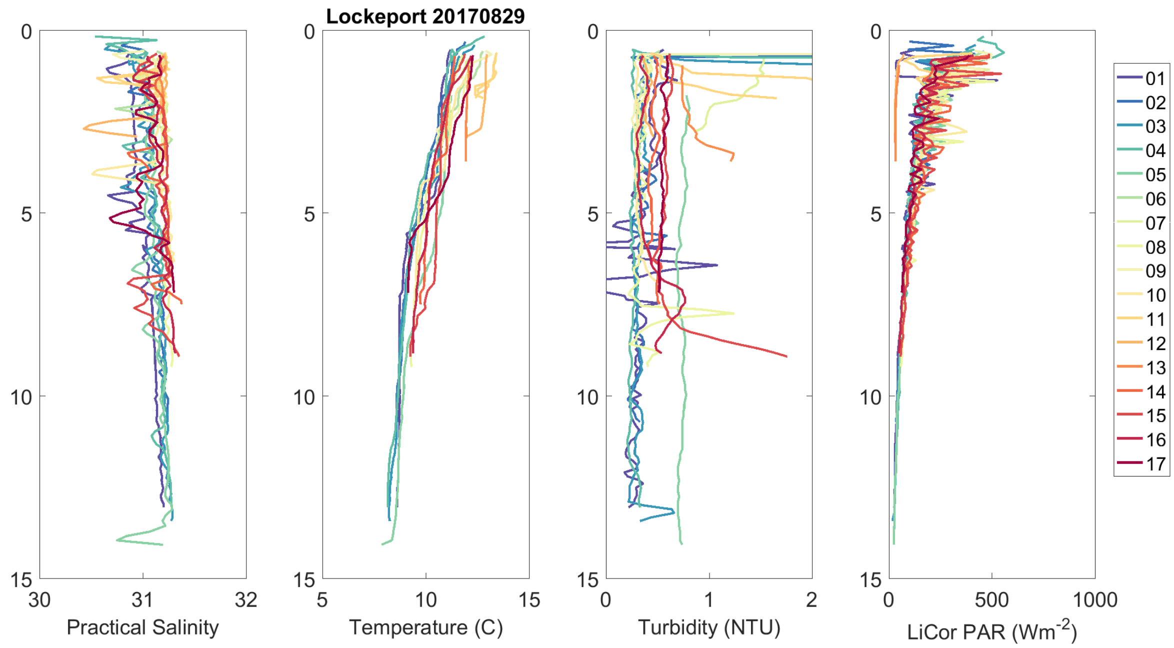

Figure 6.2: Depth averaged CTD data for Lockeport. Left to right: Salinity, temperature, turbidity, and light.

6.2 ADCP

6.2.1 Deep ADCP

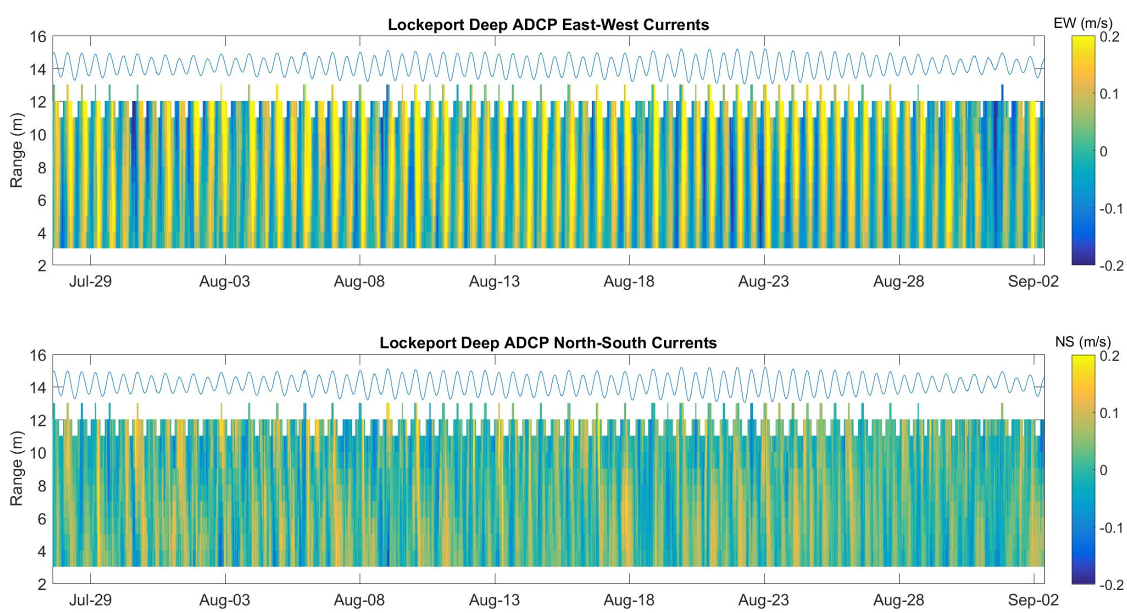

Figure 6.3: East-west (top panel) and north-south (lower panel) currents as measured by the deep ADCP between July 27 and Sept 2.

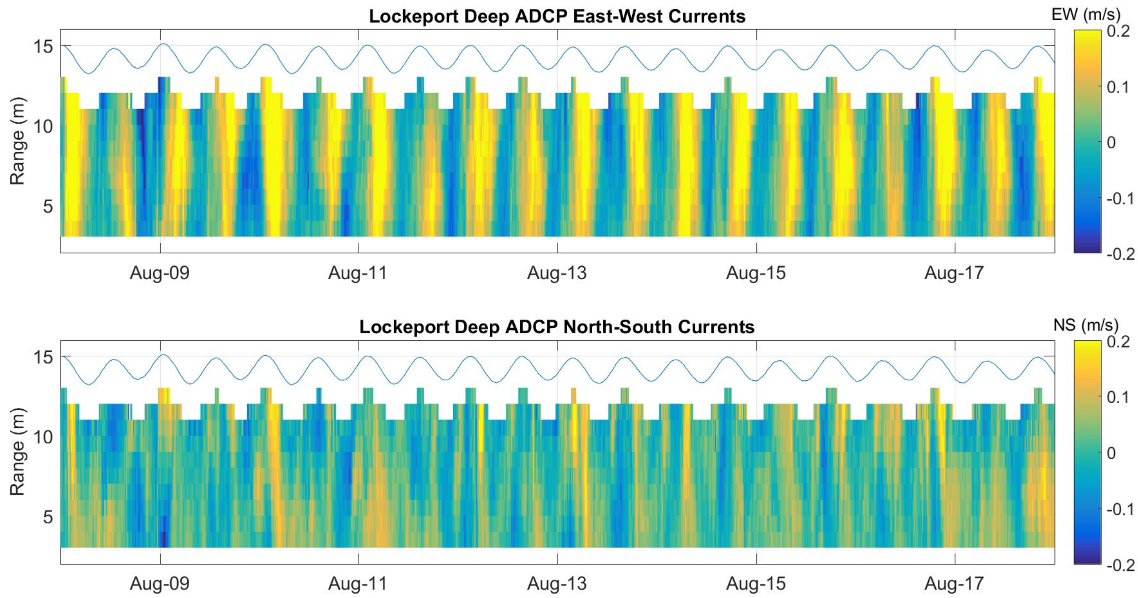

Figure 6.4: East-west (top panel) and north-south (lower panel) currents as measured by the deep ADCP between August 8 and Aug 18.

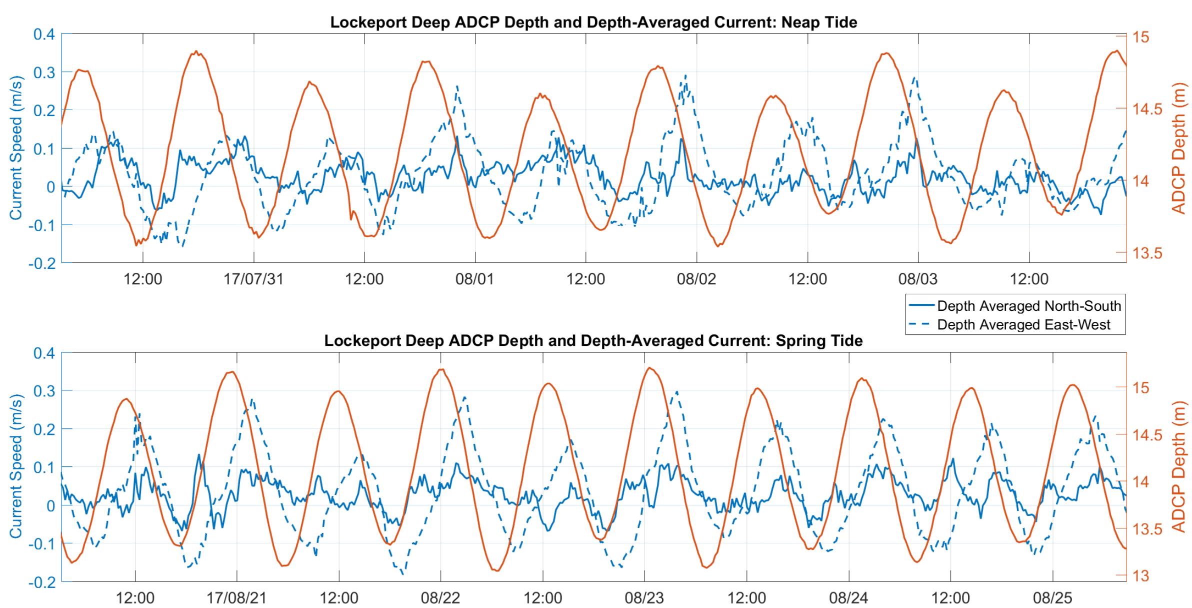

Figure 6.5: Depth averaged north-south and east-west current speed, and depth, as measured at the Deep ADCP for neap tide (upper panel) and spring tide (lower panel).

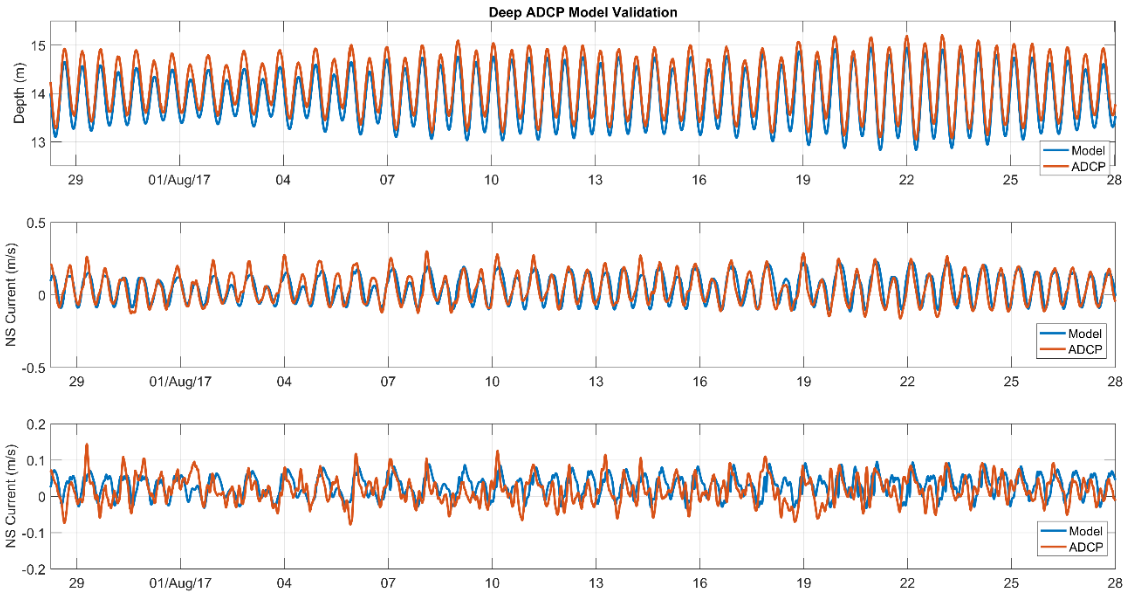

Figure 6.6: Modelled depth, NS currents, and EW currents compared to the Deep ADCP.

6.2.2 Shallow ADCP

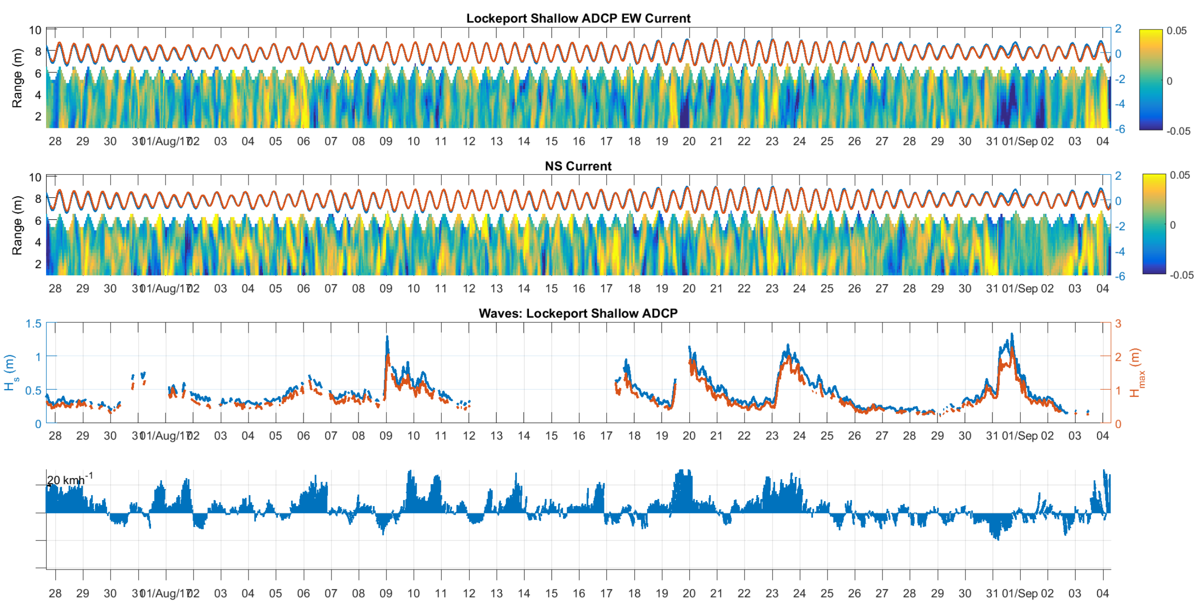

Figure 6.7: East-west (top panel) and north-south (second panel) currents as measured by the deep ADCP between July 27 and Sept 5; these panels also plot range from the ADCP to the water surface on the left axis, and water surface elevation on the right. The third panel shows significant wave height on the left (blue) axis and maximum wave height on the right (orange) axis, and the lower panel shows wind represented by vectors. Storm events are visible in all data panels as stronger currents, higher waves, and strong winds.

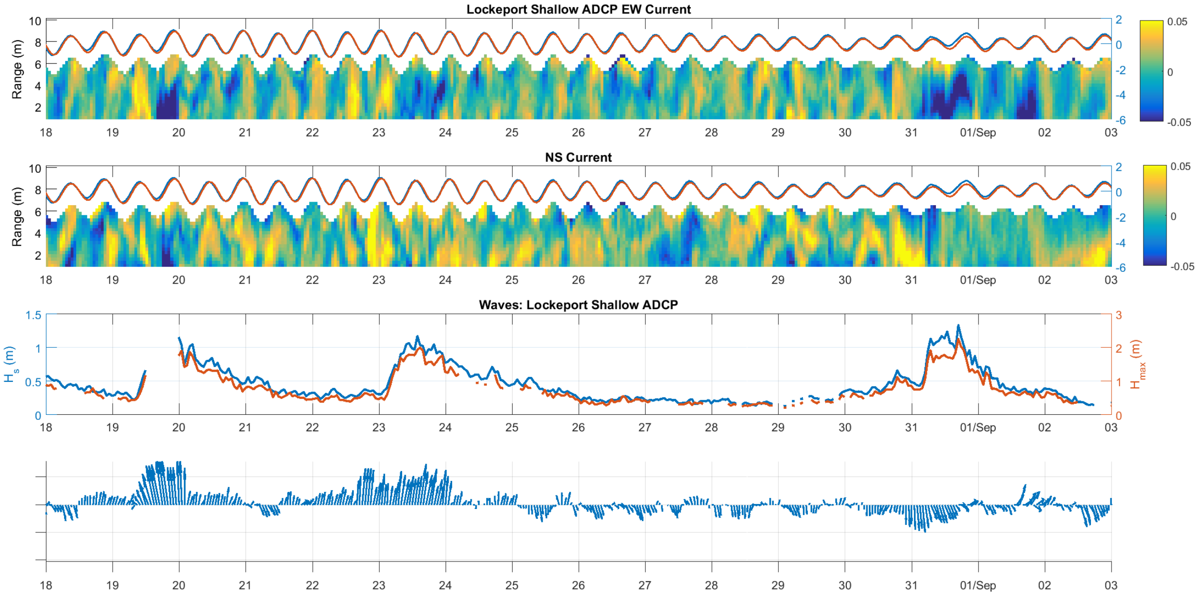

Figure 6.8: East-west (top panel) and north-south (second panel) currents as measured by the deep ADCP between Aug 18 and Sept 3; these panels also plot range from the ADCP to the water surface on the left axis, and water surface elevation on the right. The third panel shows significant wave height on the left (blue) axis and maximum wave height on the right (orange) axis, and the lower panel shows wind represented by vectors. Storm events are visible in all data panels as stronger currents, higher waves, and strong winds.

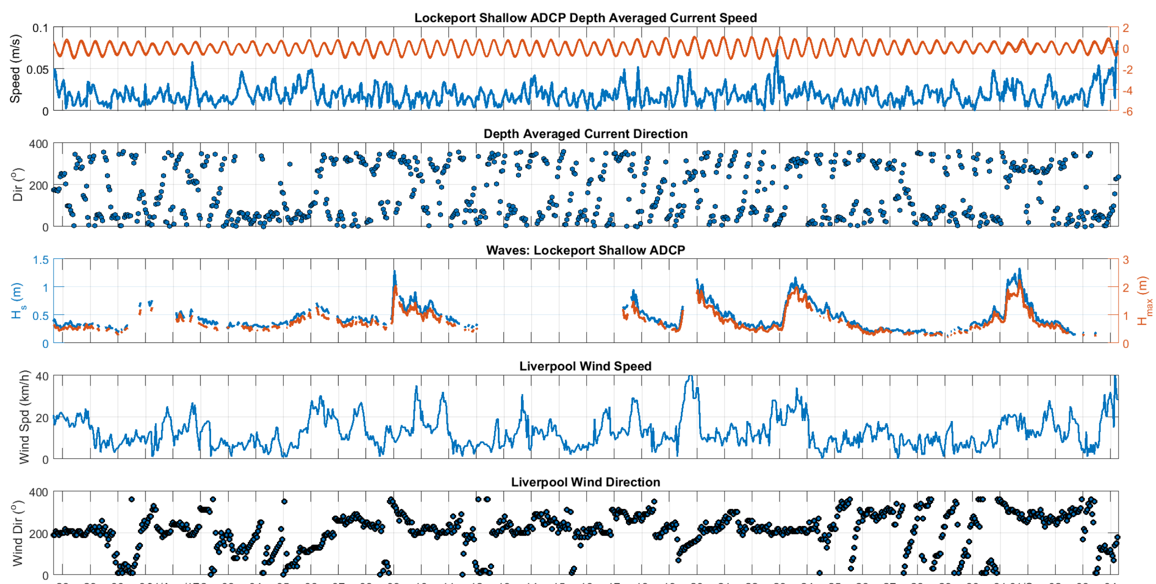

Figure 6.9: From top to bottom panel: depth averaged current speed and water surface elevation, depth averaged current direction, waves, wind speed, and wind direction.

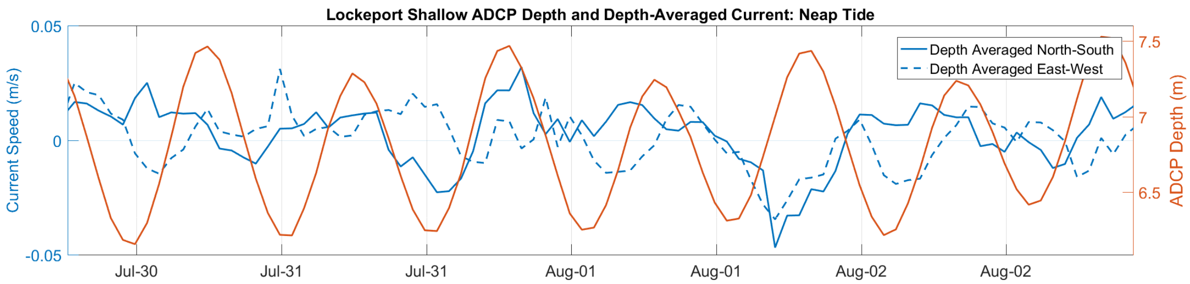

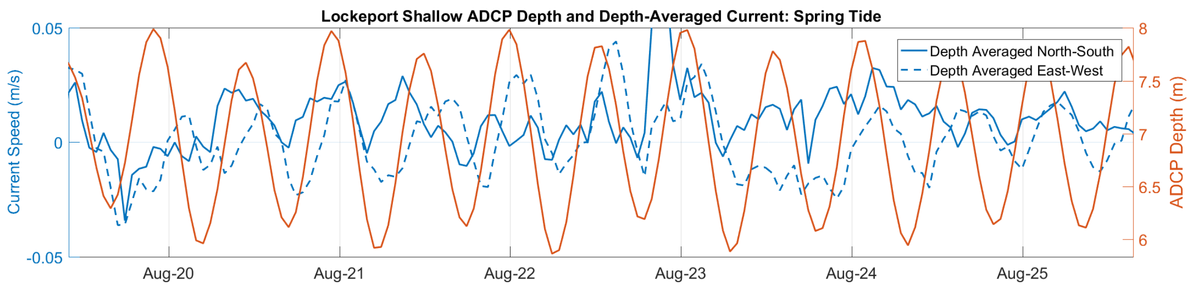

Figure 6.10: Lockeport Shallow ADCP depth and depth averaged current for neap tide period (top panel) and spring tide period (lower panel).

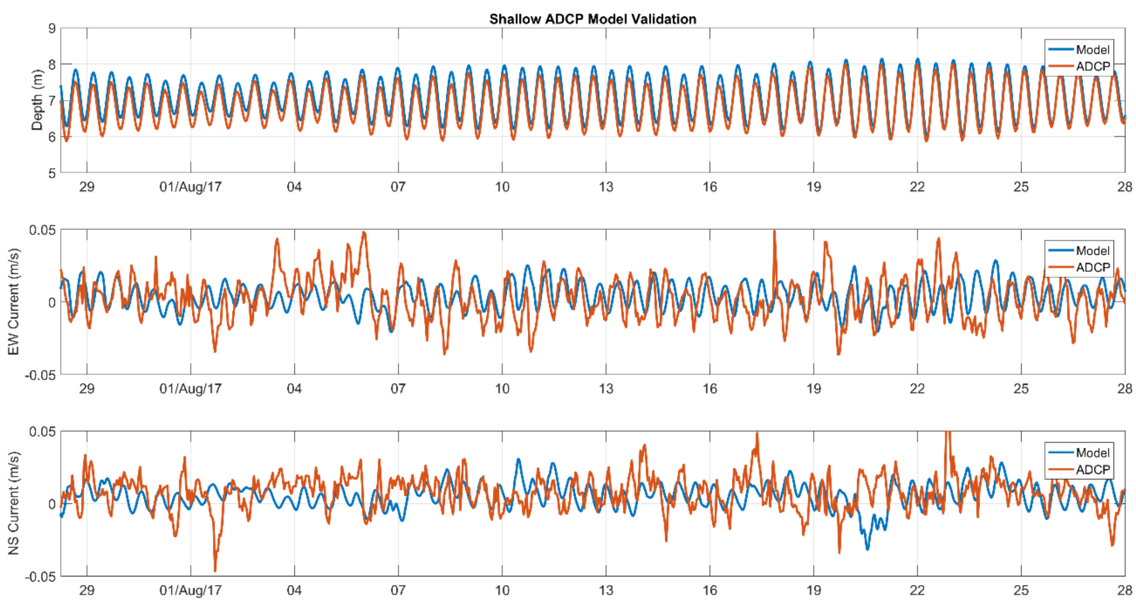

Figure 6.11: Modelled depth, NS currents, and EW currents compared to the Shallow ADCP.

6.2.3 Channel ADCP

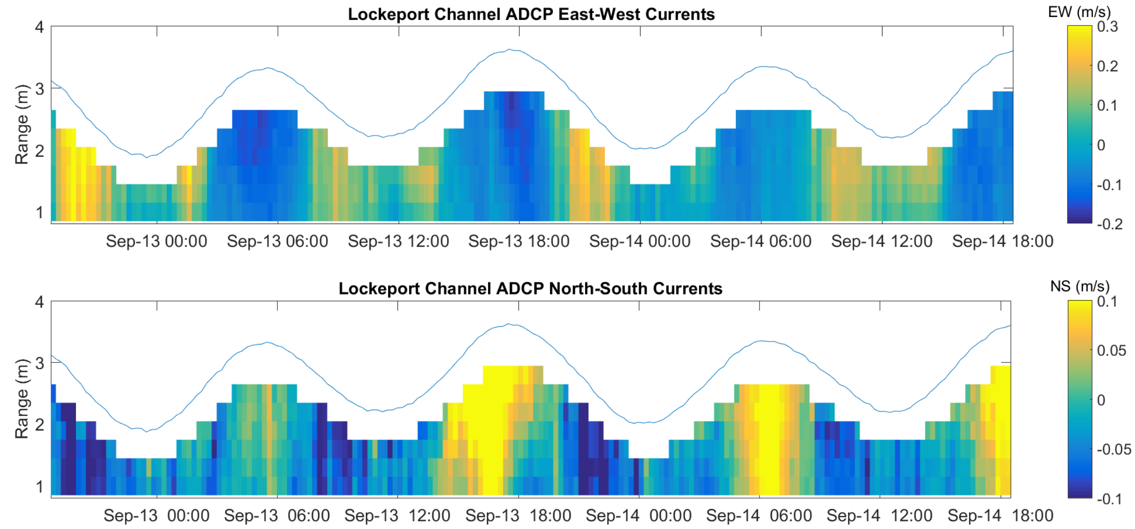

Figure 6.12: East-west (top panel) and north-south (lower panel) currents as measured by the channel ADCP between Spet 12 and Sept 14.

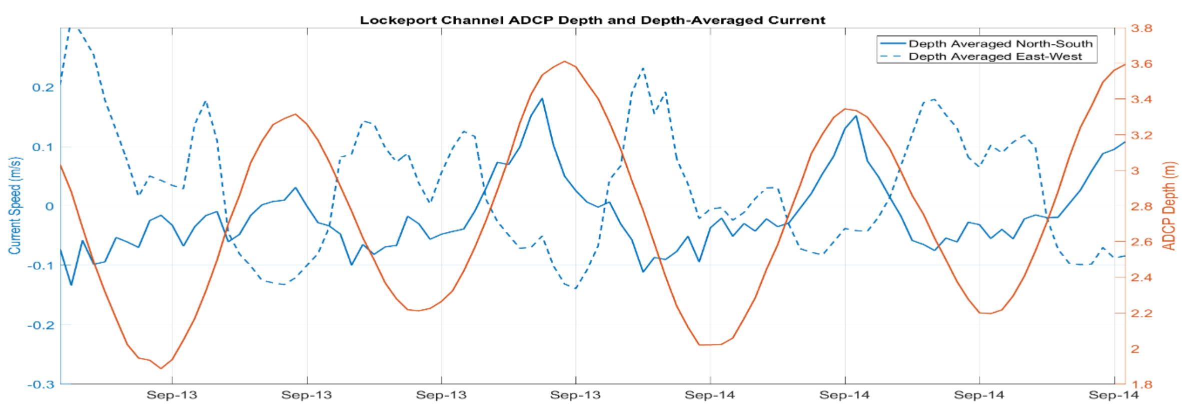

Figure 6.13: Depth averaged north-south and east-west currents, and depth, for the channel ADCP.

6.3 Drogue Experiments

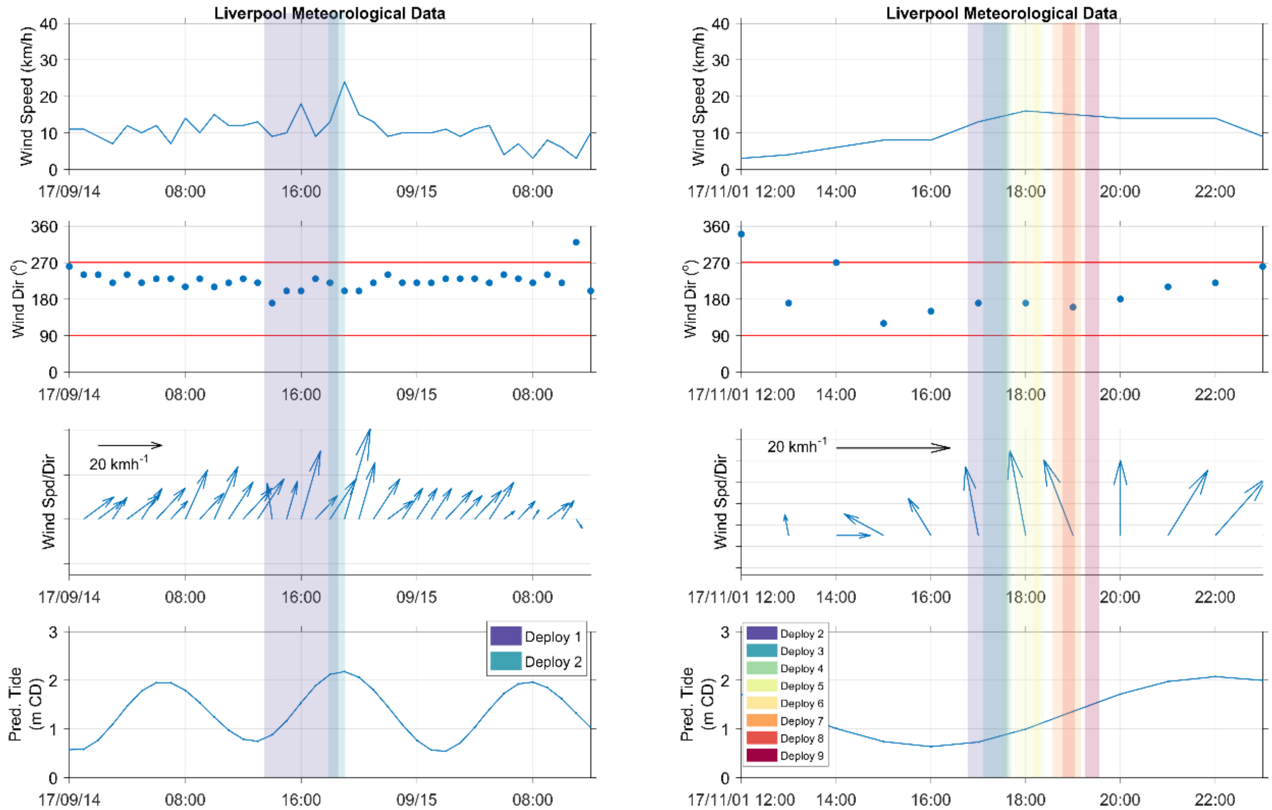

Figure 6.14: Weather as measured by Liverpool ECCC weather station during the drogue experiments in September (left) and November (right).

Time	y_proj	x_proj	Length (m)
2017/09/14 12:32:49	4839809.12	333968.38	1440
2017/09/14 17:45:44	4840214.93	333499.40	534
2017/09/14 12:31:38	4839575.31	334002.79	4123
2017/09/14 17:45:44	4840224.41	333498.03	731
2017/09/14 12:34:18	4840031.37	333874.21	3485
2017/09/14 12:32:33	4839756.11	333972.00	1760
2017/09/14 17:46:17	4840178.82	333557.99	259
2017/09/14 12:35:05	4840076.61	333873.81	797
2017/09/14 17:45:43	4840227.61	333496.81	180
2017/09/14-12:33:56	4839985.29	333898.52	1167
2017/09/14-17:45:51	4840216.83	333511.77	230
2017/09/14 12:34:25	4840044.69	333879.59	1785
2017/09/14 17:46:02	4840208.06	333530.72	1704

Table 6.1: September drogue experiment summary of name, position, start time, and length of drogue track.

Time	x_proj	y_proj	length
2017/11/01 16:43:01	333767.988	4839588.703	427
2017/11/01 16:44:55	333730.805	4839734.264	403
2017/11/01 16:45:01	333752.179	4839759.582	249
2017/11/01 16:45:23	333749.858	4839798.856	299
2017/11/01 16:45:25	333746.087	4839810.026	310
2017/11/01 16:45:48	333740.896	4839849.157	147
2017/11/01 16:45:49	333746.859	4839845.152	358
2017/11/01 16:55:20	333571.811	4840165.229	354
2017/11/01 17:04:50	333611.354	4840159.698	1092
2017/11/01 17:17:21	333597.617	4840149.794	113
2017/11/01 17:24:17	333647.573	4840127.898	324
2017/11/01 17:24:20	333639.340	4840129.472	89
2017/11/01 17:29:14	333617.646	4840197.417	337
2017/11/01 17:45:20	333765.324	4839882.857	223
2017/11/01 17:46:15	333749.972	4839903.425	232
2017/11/01 17:46:20	333751.932	4839917.284	227
2017/11/01 17:46:55	333701.928	4840000.315	305
2017/11/01 17:47:13	333686.880	4840020.568	159
2017/11/01 17:47:26	333673.222	4840037.471	340
2017/11/01 17:47:27	333677.458	4840041.725	184
2017/11/01 17:48:38	333602.009	4840156.540	582
2017/11/01 18:09:46	333584.529	4840181.680	94
2017/11/01 18:31:43	333672.659	4840082.980	324
2017/11/01 18:31:45	333659.350	4840077.256	91
2017/11/01 18:31:49	333671.237	4840075.554	363
2017/11/01 18:31:56	333678.831	4840066.767	133
2017/11/01 18:31:56	333680.317	4840066.981	215
2017/11/01 18:31:57	333706.810	4840080.481	345
2017/11/01 18:32:09	333693.840	4840041.680	492
2017/11/01 18:32:17	333705.073	4840023.469	328
2017/11/01 18:46:43	333612.244	4840156.081	331
2017/11/01 19:14:08	333753.215	4839870.751	153
2017/11/01 19:14:10	333752.150	4839865.710	223
2017/11/01 19:14:17	333743.236	4839860.082	212
2017/11/01 19:14:20	333747.466	4839858.393	208
2017/11/01 19:14:23	333743.459	4839855.726	170
2017/11/01 19:14:32	333769.005	4839831.411	244
2017/11/01 19:15:05	333795.527	4839818.902	205

Table 6.2: November drogue experiment summary of name, position, start time, and length of drogue track.

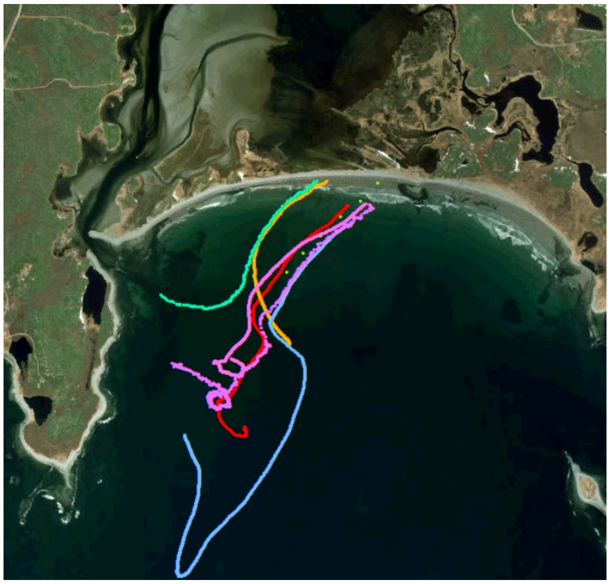


Figure 6.15: Drogue Experiment 1, Deployment 1, on September 14 2017 (left); Drogue Experiment 1, Deployment 2, on September 14 2017 (right).

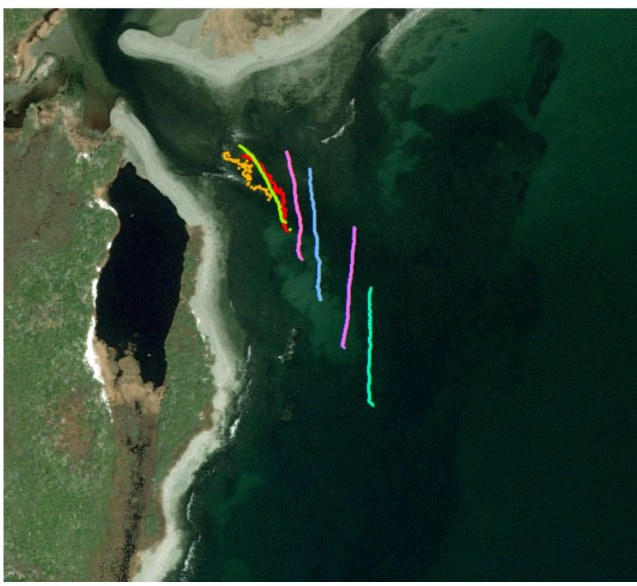


Figure 6.16: Drogue Experiment 2, Deployment 9, on November 1 2017 (left); drogues used in the experiment (right).

6.4 Light and Temperature

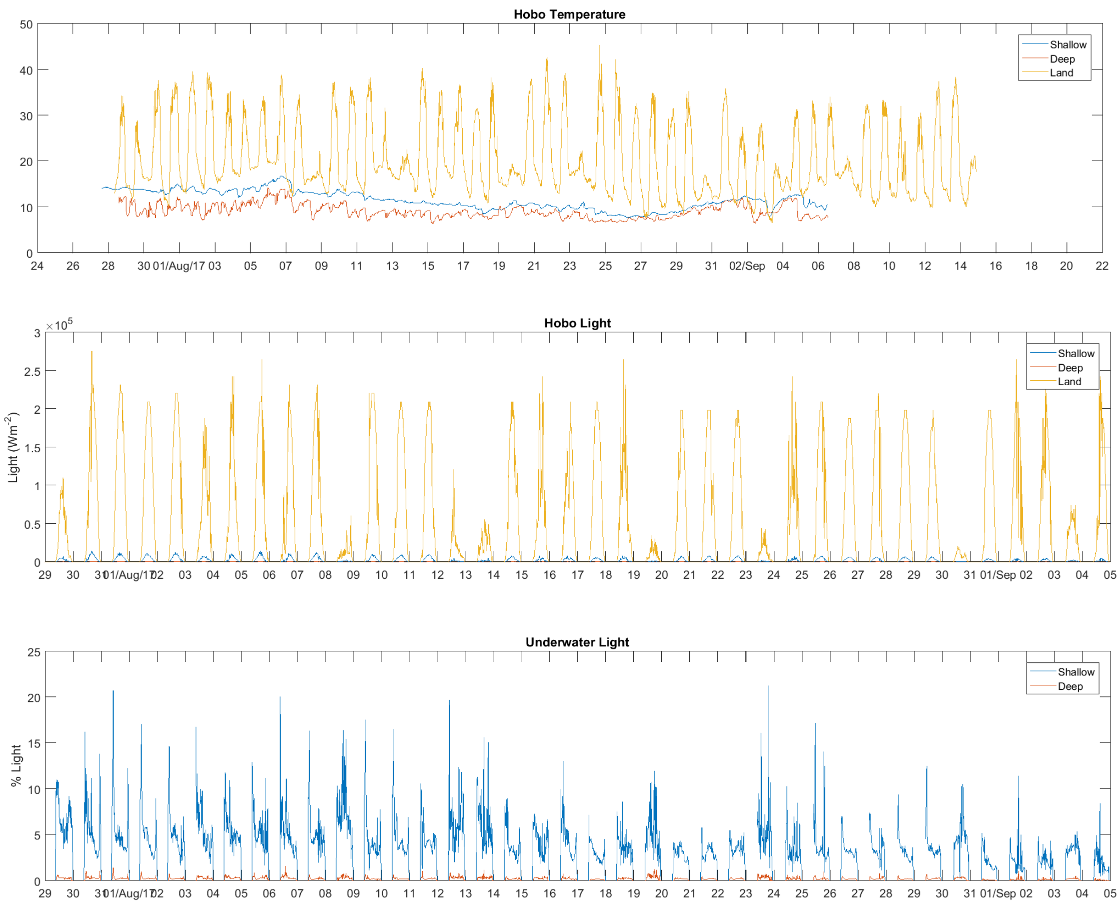

Figure 6.17: Temperature as measured by Hobo temperature (˚C) sensors attached to each ADCP and on land (top); light as measured by Hobo light (W/m^2) sensors attached to each ADCP and on land (middle); underwater light at the shallow and deep ADCPs calculated using a ratio of on-land to underwater light (bottom).

6.5 Ground Truth Imagery

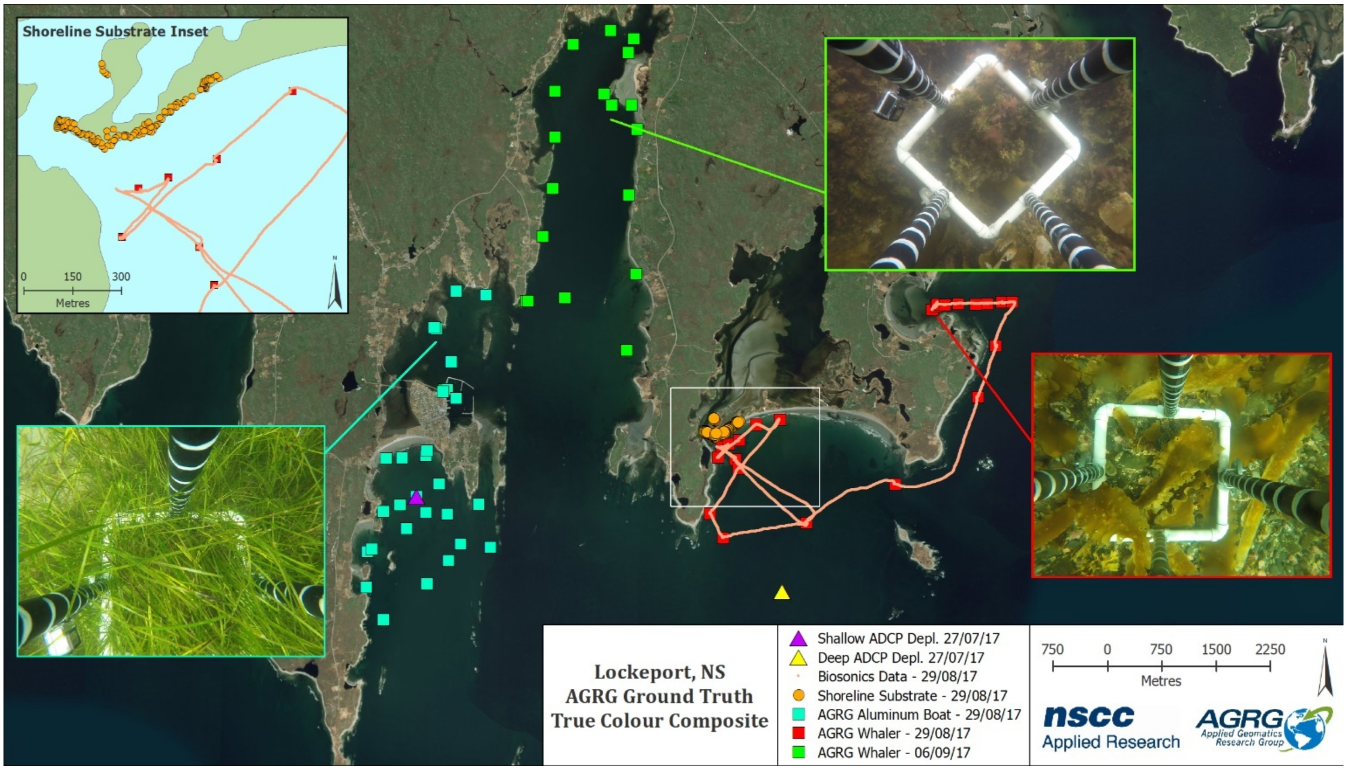

Figure 6.18: Summary of ground truth fieldwork completed at Lockeport in 2017.

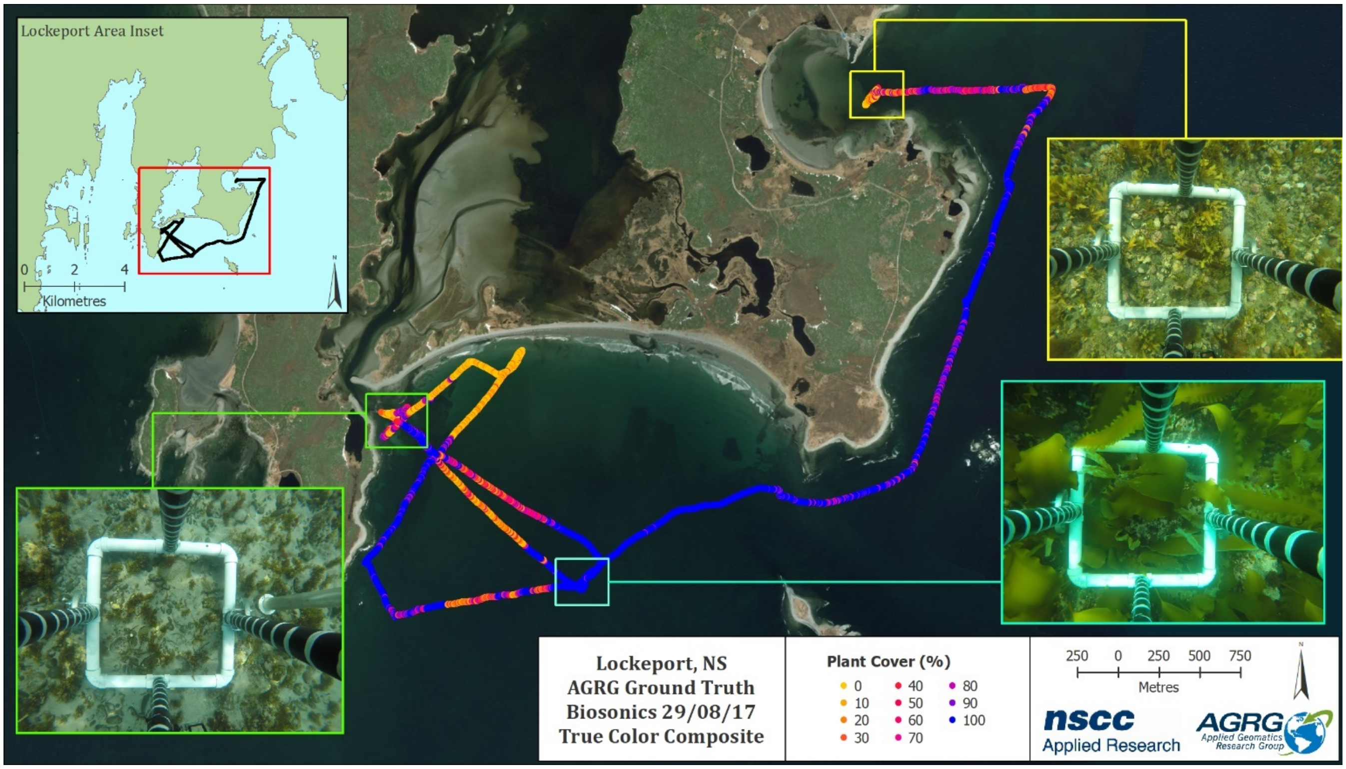

Figure 6.19: Plant cover as estimated by the Biosonics echo sounder during August 2017.

7 References

Collin, A., Archambault, P., & Long, B. (2011). Predicting species diversity of benthic communities within turbid nearshore using full-waveform bathymetric LiDAR and machine learners. *PLoS ONE*, *6*(6). https://doi.org/10.1371/journal.pone.0021265

DHI Water & Environment (2013). Mike 21 & Mike 3 Flow Model FM: Hydrodynamic Model Short Description.

Dupont, F., Hannah, C.G., Greenberg, D., Cherniawsky, J.Y., and Naimie, C.E. (2002). Modelling System for Tides for the Northwest Atlantic Coastal Ocean (Bedford Institute of Oceanography: Fisheries and Oceans Canada).

Hogrefe, K. R., Ward, D. H., Donnelly, T. F., & Dau, N. (2014). *Establishing a baseline for regional scale monitoring of eelgrass (Zostera marina) habitat on the lower Alaska Peninsula*. *Remote Sensing* (Vol. 6). https://doi.org/10.3390/rs61212447

Horn, M., and French MacKay, D. (2014). Tracjectory Modelling in Support of the Shelburne Basin Exploration Drilling Program: Model Description, Approach, and Summary of Results (South Kingstown, RI: ASA Science).

Stumpf, R. P., Holderied, K., & Sinclair, M. (2003). Determination of water depth with high-resolution satellite imagery over variable bottom types. Limonology And Oceanography, 48, 547–556. https://doi.org/10.4319/lo.2003.48.1_part_2.0547

Varma, H., Hannah, C., MacNab, R., Costello, G., Spears, T., Woodford, W., and Delbridge, C. (2008). The Complexities in the Design and Definitions of the North West Atlantic Data Set; Searching for Rational Architecture to Implement Diverse Bathymetric Data. Proc. Can. Hydrogr. Conf. Natl. Surv. Conf.

Webster, T.L., McGuigan, K., Crowell, N., Collins, K., and MacDonald, C. (2016). Optimization of data collection and refinement of post-processing techniques for Maritime Canada's first shallow water topographic-bathymetric lidar survey. J. Coast. Res.